Université de Montréal

A Multiplexed Microfluidic and Microscopy Study of Vasodilation Signaling Pathways Using Microbubble and Ultrasound Therapy

Par

Joseph Goldgewicht

Département de pharmacologie et physiologie | Faculté de médecine

Mémoire présenté en vue de l'obtention du grade de

maîtrise ès sciences appliquées en génie biomédical (M. sc. A.)

Mars 2021

University of Montreal

Department of Pharmacology and physiology/ Faculty of Medicine

---

This master's thesis, titled

A Multiplexed Microfluidic and Microscopy Study of Vasodilation Signaling Pathways Using Microbubble and Ultrasound Therapy

Presented By

Joseph Goldgewicht

Evaluated by a jury composed by the following members

Dr Sophie Lerouge
President

Dr Francois Yu
Research Director

Dr Thomas Gervais
Research Co-director

Dr Brandon Helfield
Jury member

Résumé

Dans les tumeurs solides, l'hypoxie est un mécanisme de résistance à la radiothérapie bien connu. Il a déjà été démontré que, lorsque les microbulles (MB) sont exposées à une impulsion ultrasonore (US), celles-ci peuvent induire une vasodilatation dans les tissus musculaires. De plus, une impulsion thérapeutique peut être délivrée localement dans la tumeur en dirigeant le faisceau US. Cette approche est donc proposée comme thérapie provasculaire ciblée, guidée par l'imagerie ultrasonore dans les tumeurs afin de réduire l'hypoxie avant la radiothérapie.

Le contrôle de la vasodilatation est induit par la production d'oxyde nitrique (NO) par la voie de signalisation cellulaire du eNOS dans les cellules endothéliales. Il a été démontré que l'augmentation de l'ATP extracellulaire active la voie de signalisation du eNOS. Il a aussi été démontré que l'oscillation des MB sous l'effet des US libèrent de l'ATP lorsque le tissu musculaire est traité. Cependant, les effets des différentes conditions ultrasonores et de MB sur la libération d'ATP n'ont pas encore été étudiés. Nous émettons donc l'hypothèse qu'il existe des conditions permettant de maximiser l'activation des voies de signalisation purinergiques (ATP) et d'optimiser leur durée d'activation pour une réponse provasculaire optimale.

Les motivations de ce projet sont de tester divers paramètres et d'étudier les interactions MB/cellules dans des conditions d'écoulement, qui sont généralement difficile à mettre en place lorsqu'on utilise des boîtes de Pétri. Pour quantifier plus facilement les voies de signalisation, nous avons créé des puces microfluidiques avec quatre canaux parallèles dans lesquels des cellules ont pu être cultivées. Avec quatre canaux traités lors d'une même impulsion ultrasonore, nous avons aussi augmenté le nombre de données à traiter et nous pouvons observer les effets de plusieurs impulsions lorsque les MB étaient dans un écoulement. En outre, la puce que nous avons développé est capable de donner une concentration en MB différente dans chaque canal afin de pouvoir tester quatre concentrations de MB différente dans des conditions d'écoulement. Les objectifs de ce projet de maîtrise sont donc les suivants : (1) concevoir la puce microfluidique ; (2) être capable de cultiver des cellules dans les canaux microfluidiques ; (3) créer des protocoles pour mesurer la libération d'ATP et la viabilité cellulaire après une impulsion ultrasonore ; (4)

observer la capacité de la puce à donner différentes concentrations de MB dans chaque canaux en conditions d'écoulement.

Lors de la conception de la puce microfluidique, nous avons créé un environnement dans lequel les quatre canaux de la puce ont des concentrations différentes de microbulles fluides. Ainsi, nous avons atteint les objectifs du projet. Nous avons réussi à introduire dans le canal microfluidique des cellules endothéliales de cordon ombilical humain (HUVEC) et une lignée cellulaire de cancer du sein (4T1). Les monocouches cellulaires créées par chacune des deux lignées cellulaires ont été traitées avec succès par une impulsion thérapeutique ultrasonore lors de l'injection de MB. Nos résultats montrent qu'une augmentation du nombre de cycles et de la pression, libère plus d'ATP et induisent une mortalité cellulaire plus importante. En outre, nous avons établi un lien entre la libération d'ATP et la mortalité cellulaire en comparant différentes impulsions thérapeutiques ultrasonore. Cette analyse a permis de dégager deux tendances. Avec des impulsions à faible énergie, la libération d'ATP est augmenté et on constate une très faible augmentation de la mort cellulaire ; inversement, avec des impulsions à plus forte énergie, la libération d'ATP et la mortalité cellulaire ont augmentés et on atteint un plateau. Ainsi, nos résultats confirment que différents mécanismes de libération d'ATP peuvent être déclenchés par les thérapies MB et US.

Mots-clés-Théranostic, Microbulles, Ultrasons, Microfluidique, libération d'ATP

Abstract

In solid tumors, hypoxia is a well-known resistance mechanism to radiation therapy. It was previously shown that microbubbles (MBs), when exposed to an ultrasound pulse (US) can cause vasodilation in muscle tissue. Conceptually, the therapeutic pulse can be localized on the tumor by steering the US beam. This approach is therefore proposed as a targeted image-guided provascular therapy in tumors to reduce hypoxia before radiotherapy. However, the effects of US and MB conditions on the relative increase in tumor perfusion remain largely unknown.

Vascular control is managed by the production of nitric oxide (NO) through the eNOS pathway inside the endothelial cells. Increases in extracellular ATP have been shown to be a signaling event for the activation of this pathway. Fittingly, MB and US have been shown to release ATP when muscle tissue was treated. However, the effects of therapeutic US and MB parameters on the treatment have not yet been described. We, therefore, hypothesize that there are conditions that will maximize the purinergic signaling pathways (ATP) and optimize their time course for an optimal provascular response.

The motivation for this project came from the desire to test various parameters and study MB/cell interactions in flowing conditions, which are typically limited when using petri dish setups. To quantify more easily the signaling pathways, we created microfluidic chips with four parallel cell coated channels. This chip allowed us to increase the throughput when using a single US exposure in static conditions and with the ability to support multiple US exposures with MB replenishment in flowing conditions. Also, the custom-made chip multiplexes the bubble concentration to obtain four channels with different flowing microbubble concentrations. The goals of this master's project were thus: (1) to design the microfluidic chip; (2) to demonstrate the capacity for cell culture; (3) create protocols for measuring ATP and cell viability after therapeutic pulses; (4) to demonstrate repeatable flowing conditions with the multiplexed MB concentration.

On the design of the microfluidic chip, we were successful at creating an environment where four of the four channels in the chip have different concentrations of flowing microbubbles. Thus, fulfilling the project's goals. We have succeeded in seeding both Human Umbilical Vein

Endothelial Cells (HUVECs) and a breast cancer cell line (4T1) into the microfluidic channel. The cell monolayers created by both cell lines were successfully treated with an US and MB therapeutic pulse. Our results support that an increase in both, cycles and pressure, release more ATP and cause more cell death. Further, we linked ATP release to cell death by comparing different therapeutic pulses. From this analysis, two trends appeared. With lower energy pulses, ATP release increased sharply with a very small increase in cell death; conversely, with higher energy pulses, ATP release continued to increase with cell death but reached a plateau. Thus, our results support that different mechanisms of ATP release can likely be triggered by MB and US therapy.

Keywords—Theranostics, Microbubbles, Ultrasound, Microfluidics, ATP release

Table of Contents

Résumé 1

Abstract 3

Table of Contents 5

List of Tables 10

List of Figures 11

List of Abbreviations 16

Acknowledgments 19

Chapter 1 Introduction 21

1.1 Objectives 23

Chapter 2 Theoretical Background and Literature Review 25

2.1 Ultrasound and Microbubbles 25

2.1.1 Ultrasound Physics 25

2.1.1.1 Single Element Ultrasound Wave Transmission 25

2.1.1.2 Scattering 28

2.1.1.3 Attenuation 28

2.1.1.4 US Image Formation 29

2.1.2 Microbubble Oscillations 31

2.1.2.1 Stable Cavitation 31

2.1.2.2 Inertial Cavitation 32

2.2 Vasodilation and ATP Release Following MB+US 33

2.3 In Vitro Studies of Microbubble Cell Interactions 35

2.3.1 Sonoporation 35

2.3.2 Calcium Waves 37
2.3.3 Enhanced Endocytosis 38
2.4 Microscopy and Imaging 40
2.4.1 Fluorescence 40
2.4.2 Bioluminescence 41
2.5 Microfluidic Structures 43
2.5.1 Fundamental Physics 43
2.5.2 Mixing in Microfluidics 46
2.5.2.1 Diffusion Estimation for MB Sized Particles 48
2.5.3 Input Flow Options 49
2.6 Microfluidic Chips to Study MB/Cell Interactions 49
Chapter 3 Methods 51
3.1 Microfluidic Device, Conception, Manufacturing, and Validation 51
3.1.1 Goals and Requirements of Microfluidic Chip Design 51
3.1.1.1 Polydimethylsiloxane (PDMS) 52
3.1.1.2 Fibronectin Surface Coating for Cell Culture 52
3.1.1.3 Cell Culture on the Roof of the Flow Channels 53
3.1.1.4 Multiplexing key Parameters of MB/Cell Interactions 53
3.1.1.5 Further Design Considerations 54
3.1.2 Design Formulation and Methodology 55
3.1.2.1 Concentration Divider 55
3.1.2.2 Mixer Options 55
3.1.2.3 Testing Section 56
3.1.3 Electric Circuit Analog 56

3.1.4 Micromixer 61
3.1.5 Modeling 61
3.1.6 Final Design 62
3.1.7 Validation 63
3.1.7.1 Concentration Distribution 63
3.1.7.2 Imaging Microbubbles 63
3.1.7.3 US Pressure Attenuation 64
3.1.8 Manufacturing 65
3.2 Cell Viability and ATP Release After Ultrasound and MB Therapy 66
3.2.1 Cell Seeding 66
3.2.2 Cell Viability Assays 68
3.2.3 Static Bubbles Experimental Setup 68
3.2.4 Setup for Flowing MB Experiments 70
3.2.5 Imaging and Image Processing 70
3.2.6 Cell to Nucleus Ratio 73
3.3 ATP Release Assays 74
3.3.1 Experimental Setup 74
3.3.2 Image processing 76
3.4 Statistical analysis 77
Chapter 4 Results 79
4.1.1 Microfluidic Chip Pressure Attenuation 79
4.1.2 Microfluidic Chip Concentration Validation 80
4.1.2.1 Static Food Coloring 81
4.1.2.2 Flowing Food Coloring 82

4.1.2.3 Flowing Bubbles 85
4.1.3 Static Cell Viability with 4T1 89
4.1.4 Static ATP Release 91
4.1.5 ATP Released vs % Dead Cells in Static Conditions 95
4.1.6 HUVEC Viability in Flowing Conditions 97
Chapter 5 Discussion 100
5.1 Microfluidic Device 100
5.1.1 Manufacturing and Handling 100
5.1.1.1 -6dB US area 101
5.1.1.2 Problem with Trapped Air 101
5.1.1.3 Improvements 101
5.1.2 PDMS Attenuation 102
5.1.3 Microbubble Mixing 102
5.1.3.1 Surface Modifications for Bubble Flow 104
5.1.3.2 Artifacts and small amounts of MB in the control channel 106
5.2 Cell growth 107
5.2.1 4T1 Cell Line 107
5.2.2 Endothelial Cells 107
5.2.3 Future Considerations 107
5.3 Image Analysis 108
5.4 Static Tests 108
5.4.1 Viability Studies 109
5.4.1.1 Image Analysis 109
5.4.1.2 Limitations: Using Offline Methods for Cell Viability 110

5.4.2 ATP Release Studies 110
5.4.2.1 Time Constant 111
5.4.2.2 Possible Release Mechanisms 111
5.4.2.3 Limitations 112
Limitation 1: Focussing 112
Limitation 2: Alignment and US Beam Size Miscalculation 112
Limitation 3: Time constant estimation of low signal 113
Limitation 4: Noise in estimation time to peak 113
5.4.3 Relation of ATP Released, Time to Peak, Release Speed and Cell Death 114
5.4.3.1 ATP Released and Cell Death 114
5.4.3.2 Time to Peak 115
5.4.3.3 ATP Release Speed 115
5.4.3.4 Conclusion 116
5.5 Flowing Viability Tests 116
Chapter 6 Conclusion 118
6.1 Future work 118
Bibliography 121
Annexes 131
Annexe A- IEEE IUS conference proceedings 131
Annexe B- Rodin Chermat report. 140

List of Tables

Table 1 The length width and height of each of the size branches of the concertation divider. Colored in dark green are the two arbitrary lengths and widths that make the system fit into the printable bed rectangle. At an input current of 200 µL/min. 62
Table 2 Pressures and number of cycles used as bursts in the MB and US therapeutic pulse. 68
Table 3 Bubble count at the roof for 5 chips with the smooth surface..... 88
Table 4 Bubble size at the roof for 5 chips with the smooth surface..... 88
Table 5 Bubble speed at the roof for 5 chips with a smooth surface..... 89
Table 6 Error from hydraulic resistance equation approximation. 104

List of Figures

Figure 1 Example of how different sections of a tumor can have different oxygenation levels [5]..... 22
Figure 2 Illustration of the movement of the ultrasound wave, i.e. a longitudinal pressure wave, across a media. (Adapted from http://www.bats.ac.nz/detail-basic_theory_of_ultrasound-29)..... 26
Figure 3 An illustration of how interference creates zones of higher and lower pressure along the path of the US wave. (c.f. Bushberg et al., The Essential Physics of Medical Imaging, p.491). 27
Figure 4 An illustration of how a wave refracts after crossing a boundary between two materials with a different speed of sound. [10] 27
Figure 5 Scattering of a pressure wave depending on the boundary type or on the size of the reflector [7] 28
Figure 6 Contrast-enhanced ultrasound image of liver tissue [17] and an image of super-resolution imaging of a rat kidney [16] 30
Figure 7 Sonovue microbubbles were intravenously injected into healthy volunteers and an image of the heart. a) shows the image pre-burst, b) during and c-h) show the microbubbles being replenished in the ventricle wall. [18] 30
Figure 8 A) A schematic of the pressure variation of the US wave. B and C) The behaviors of a MB under stable and inertial cavitation.[21] 31
Figure 9 A MB oscillating and causing microjets of fluid seen in the second and third panels. [39] 32
Figure 10 Illustration of the prevalent hypothesis leading to the creation of NO after MB and US therapy. The release of ATP by either an endothelial cell or a red blood cell then leads to an activation of the eNOS enzyme creating NO from L-arg. The NO then diffuses into the smooth muscle cell leading to relaxation and vasodilation. [6] 34
Figure 11 A schematic on how extracellular ATP can induce ATP release through the pannexin channel as activated by the P2Y receptor. [59] 35
Figure 12 An example of a membrane poration after a cell's interactions with a resonating Microbubble. Note how the pore forms and slowly reseals after 40 seconds. [66] 36
Figure 13 a) An example of a single MB sonoporation of a cell followed by a calcium fluctuation and the delayed calcium fluctuation in the adjacent cells. b) Calcium signal in each of the segmented cells over time. c) The signal as a function of distance and time. It clearly shows that locations further from the MB, experience a delayed calcium fluctuation [30]. 38

Figure 14 Illustration of the conversion of ATP into light [84]. 42
Figure 15 An illustration of how a modified tesla valve can function as a passive mixer in microfluidics [99]. 48
Figure 16 A top view of the mold for the microfluidic chip. The concentration divider is highlighted in pink. The micromixer is highlighted in blue. The testing section is highlighted in green. 52
Figure 17 Top- An electric circuit analog to the microfluidic elements. Two input currents that branch into three sections each, which then join to form four equal branches. Bottom- The physical equivalent of the electric resistances. 57
Figure 18 The final design of the microfluidic chip. 62
Figure 19 Setup to measure the attenuation of the PDMS slab. 65
Figure 20 Process for seeding and cultivating cells on the roof of the microfluidic chip. 68
Figure 21 The Ultrasound setup for exposing the cells inside the microfluidic chip to US and MB therapy. 69
Figure 22 Left- Inputting MBs into the chip with cells cultured on the roof so that the two can interact. Right- After US exposure the cells are allowed to rest for 10 min before Calcein AM is added to stain cells that are still alive. After 30 minutes of incubation with Calcein AM, the cells are exposed to a PI solution to stain dead cells. 70
Figure 23 Example of how images are taken in order at the microscope. The ordered images were converted into image stacks and then grouped together to be automatically analyzed by an algorithm. 72
Figure 24 Graphical representations of how the algorithm segments and obtains a quantitative measure of cell death. Top- How the algorithm functions with HUVEC cells. Bottom- How the algorithm calculates cell death using areas. 73
Figure 25 An example image of 4T1 cells, where green marks a cell's cytoplasm and blue marks their respective nucleus. To the right is the thresholded image. The areas of each were taken to obtain the cytoplasm to nucleolus ratio. 74
Figure 26 The experimental setup of ATP live imaging. The chip has Luciferin luciferase and MB solution. 75
Figure 27 A) The overlay of the peak signal colored in green and the brightfield image of the US probe. B) Shows an example of ROI processing with the signal colored in red, the linear fit for ATP released colored in orange, and the exponential fit colored in yellow. C) An image collected by the camera before the US pulse was sent with the 4 ROIs analyzed. D) An image of the same 4 ROIs but after

the US pulse was sent. E) The graphs of the 4 ROI's analyzed in the tiff stack with their respective outputs of ATP released, ATP release speed, and ATP time constant 77
Figure 28 An example of a control pulse signal vs an attenuated pulse signal. 79
Figure 29 The ratio of attenuation of the three slabs at different US pressures repeated at different locations. 80
Figure 30 Pixel value plotted against the average concentration of static food coloring inside the chip. Error bars are the standard deviation of the average pixel values of the images. (R^2=.99, F=statistic p-value<<.001) 81
Figure 31 Purple rectangle-from top to bottom static food dye in the channels from 0% to 100% going down. Top of the blue rectangle- Example of the ROI selected to calculate the average pixel signal. Going down the images of the control, 30% 70% and 100% channels are seen under flowing conditions of 200 µL/min 83
Figure 32 Sample images at important locations in the flow path of the chip. In the black and blue rectangles, the entrances to the 70% and the 30% channel are shown. In the red and yellow rectangles, the tesla mixer is shown mixing the two liquids. In the green rectangle, the flow of the 4 different channels at 200 µL/min can be seen. 84
Figure 33 Top- Effect of the input flow on food coloring pixel value. Bottom- Efficacy of mixing, expressed in % mixed for each channel for the three different flows. 85
Figure 34 Example of frames taken from videos of microbubbles flowing in the four channels of the microfluidic chip. In the first column (a-d) the raw frame is shown. The dots seen are the MBs flowing at the roof of each of the channels. The second column (e-h) shows the output of the MATLAB circle finder function as blue circles. These were used to assess the count and the size of the MBs. The third column shows the resulting tracks from the TrackMate program. These were used to quantify the speed of the bubbles. 87
Figure 35 a-e) Examples of pictures of 4T1 cells with the Calcein and the PI images superimposed. f-j) The Calcein channel superimposed with the automatic threshold. k-o) the PI signal superimposed with the automatic thresholded image. 90
Figure 36 Boxplot of % dead cells depending on #cycles and US pressure after a single US pulse. Each dot represents the average value for one channel in each chip. N=20 (5 repeats, 4 channels per chip). One-way ANOVA followed by Tukey multiple comparisons. *p < 0.05; **p < 0.01. 91
Figure 37 Examples of the ATP signal superimposed with the brightfield image. The ATP signal was scaled for better visualization. 92

Figure 38 The ATP released by the 4T1 cells dependent on cycles and US pressure. Each dot represents the average for one channel in each chip. N=20 (5 repeats, 4 channels per chip). One-way ANOVA followed by Tukey multiple comparisons. *p < 0.05; **p < 0.01. 93
Figure 39 The ATP released speed by the 4T1 cells dependent on cycles and US pressure. Each dot represents the average for one channel in each chip. N=20 (5 repeats, 4 channels per chip). One-way ANOVA followed by Tukey multiple comparisons. *p < 0.05; **p < 0.01..... 93
Figure 40 Time between the US activation and the peak signal plotted against cycles and US pressure. Each dot represents the time constant for one channel in each chip. N=20 (5 repeats, 4 channels per chip). One-way ANOVA followed by Tukey multiple comparisons. *p < 0.05; **p < 0.01. 94
Figure 41 The ATP consumption rate time constant by the luciferin and luciferase assay plotted against cycles and US pressure. Each dot represents the time constant for one channel in each chip. N=20 (5 repeats, 4 channels per chip). One-way ANOVA followed by Tukey multiple comparisons. *p < 0.05; **p < 0.01. 95
Figure 42 Each condition is shown as a dot plotted where the average % dead cells against the average ATP released. Two sections can be seen: a section in blue representing conditions where ATP is released with low cell death; and a section in red representing conditions where ATP is still released but with an increase in cell death..... 96
Figure 43 Each condition tested as a dot plotted where the average percentage cell death against the average ATP release speed. 97
Figure 44 a-c) Examples of pictures of HUVEC cells with the Calcein and the PI images superimposed. d-f) The Calcein channel is superimposed with the automatic watershed transform segmenting out the cells. g-i) the PI signal is superimposed with the automatic watershed transform identifying the dead cells. 98
Figure 45 In the blue rectangle the effect on cell death of the 3 pulses on HUVEC cells with flowing bubbles while the orange rectangle displays the effect of a single pulse. a) Shows the fluorescent image of the 100% and the 30% channel. b) Shows the images for the control and the 70% channel. c and d) Show the same channels but for the single pulse experiment..... 99
Figure 46 Three examples of scratches and mold usage translating into changes in channel geometry. a) The small channel carrying MB into the 30% channel being significantly affected in cross-sectional area. b-c) Intrusions into the channel of the 70% MB carrying channel..... 103

Figure 47 Problems with bubble entrapment due to surface roughness and stair traps in the original design. Bottom- An illustration of how the new chip is made to minimize the bubbles from being trapped. 105
Figure 48 a-d) The staircase traps causing bubble accumulations. e-f) Surface roughness features causing bubble accumulations in the roof of the chip. 106
Figure 49 Two sample images with a blurry background or noise. 108
Figure 50 Differences between signal covering the entire channel vs single spot. 111
Figure 51 Two pictures showing the difference between a well-focused image (right) vs an unfocused signal (left) 112
Figure 52 An example of a noisy signal inside an ROI. The two vertical black lines indicate the activation of the US pulse and the peak of the signal. Both of these time coordinates and ATP values were used in the analysis. The red line is the line of best fit of the signal between the two black lines. The slope of this line dictates the ATP release speed. The yellow fitted curve is an exponential fit of the signal between the second black line and the last time point. The time constant of that fit is the time constant used in the analysis. 114

List of Abbreviations

ATP : Adenosine triphosphate

dB : Decibels

DNA : Deoxyribonucleic acid

eNOS : Endothelial NO synthase

HUVECS : Human Umbilical Vein Endothelial Cells

kDa : Kilodalton

kPa : Kilopascal

kHz : Kilohertz

MDa : Megadalton

MHz : Megahertz

MPa : Megapascal

MB : Microbubbles

NO : Nitric Oxide

PDMS : Polydimethylsiloxane

PI : Propidium iodide

ROI : Region of Interest

SEM : Scanning Electron Microscope

US : Ultrasound

To tio Isra, for sparking my curiosity.

Acknowledgments

I would like to thank **Dr. Francois Yu** for teaching, guiding, and helping me grow as a person and a scientist. Without his work and constructive feedback, this project would not have been possible.

I would like to thank:

Ju Jing Tan and the rest of the 8th-floor team for the help and knowledge provided for imaging ATP.

Rodin and Amelie for the help with cell culture, chip manufacturing, and overall support for my project when creating, designing, and manufacturing the microfluidic chip.

Boris, Dr. Loise Allard, Dr. Guy Cloutier, and the rest of the LBUM team for the constant support and feedback during the weekly presentations.

The members of MTL YU Lab for your contributions feedback and overall support during these last few years.

Nick, Cory, and all the **rest of my friends** for the encouragement and help all along.

Dani, for reading, listening and supporting me throughout the project.

Finally, **my parents, my sister, and the rest of my family** for their unconditional love and support.

Chapter 1 Introduction

Cancer is a major cause of death across the globe. In Canada, it is responsible for 30% of total deaths and it is estimated that more than 200,000 people were diagnosed in 2020 alone, causing 83,000 deaths [1]. It has been one of the major challenges in healthcare for the past century. Huge leaps in treatment and detection are improving patient care. For example, when compared to the 1990s, between 2005 and 2009 the risk of death at 5 years fell by 52% for breast cancer, 43% for colon cancers, and even 68% for prostate cancer [2]. However, much work remains to be done.

One of the main tools to treat tumors is radiotherapy. This treatment uses high-energy X-rays or protons to destroy the DNA inside cancer cells. Generally, radiation therapy can occur with either an external beam or an internal source of radiation [3]. As their name suggests, external radiotherapy delivers radiation through a machine outside the body, while internal radiotherapy uses radioactive implants that are surgically placed into the tumor or surrounding tissue [3]. During the 1950s, when Louis Gray was working on the effects of radiation, he noted that oxygen has an effect on radiation across different biological systems [4]. Indeed, the main pathway for effective treatment is the creation of reactive oxygen species through radiation that then damages the tumor's DNA, resulting in cell death [5].

Due to abnormal vasculature in tumors, their oxygenation levels can vary depending on the shape and size of the tumor as seen in Figure 1. This means that many tumors have hypoxic areas that are resistant to radiotherapy [5]. Certainly, it has been previously shown that hypoxic tumors have a higher resistance to radiotherapy and that lower oxygen tension is associated with this higher resistance [4]. The main problem is that normal tissue can also be affected by radiotherapy, so there is an upper limit to the radiation dosage [5]. Therefore, a therapy that would increase the oxygenation inside the tumors would boost the efficiency of radiotherapy.

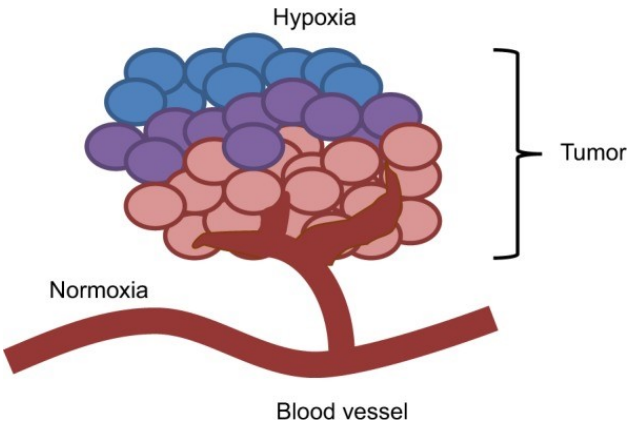

Figure 1 Example of how different sections of a tumor can have different oxygenation levels [5]

Microbubbles **(MBs)** are tiny gas-filled bubbles that are around 2 - 10 µm in diameter that can be injected into the bloodstream. Given that MBs are filled with a compressible gas, their volume can vary in an ultrasound **(US)** pressure field and have long been used as contrast agents in ultrasound imaging. These volumetric non-linear oscillations can be detected and thus provide a MB specific signature easily separable from surrounding tissues. Interestingly, when exposed to higher amplitude US pressure waves, MBs can cause biophysical effects that can be harnessed for therapy: for example, recently, MB+US has been shown to increase blood flow in muscle [6]. These effects are created by resonating MBs, which in turn, create streams of fluid that cause an increase in shear stress when close to endothelial cells. Fittingly, MBs can also be used to measure changes in perfusion in vivo. Thus, by combining these two applications, MBs and US become a theranostic approach (diagnostic and therapeutic) to therapeutically increase blood flow in tumors and assess the effectiveness of the therapy by US imaging. Therefore, one area of research in our laboratory is to use a MB+US therapy to locally increase the blood flow in a hypoxic tumor to sensitize it to radiotherapy.

In the “Microbubble Theranostics Laboratory”, we are studying this therapeutic strategy using in vivo and in vitro experiments. Currently, in vivo tests in mice are being performed to quantify the effect of different US parameters on the increase in perfusion in hypoxic tumor models. To complement this work and provide mechanistic insights, this master's project delves deeper into

the creation and development of in-vitro methods to further characterize the vasodilation pathways of the US and MB therapy.

1.1 **Objectives**

In this master's thesis, the specific goal is to quantify the effect of an US and MB therapeutic pulse on ATP release using in vitro cell culture submitted to flow, to more closely mimic in vivo conditions compared to MB/cell interactions studied in static Petri dishes.

This goal can be split into two main components: (1) creating structures and conditions that resemble in vivo flowing MB conditions; and (2) quantifying the effects of the therapeutic pulse on ATP release and cell viability.

Different approaches have been used in literature to create an environment where MBs and cells can interact either using an Opticell, well plates, or microfluidics structures, researchers have found methods to have MB interact with a variety of cell lines. Specifically, for this project, we chose to use microfluidics, as it offered a way to have the cells interact with flowing MBs, allowing for bubble replenishment between therapeutic pulses, which is how tissues are treated in vivo. As will be explained later on, microfluidics allowed us to design a very specific chip to have four channels with flowing MBs with four different MB concentrations. The novelty of this design is to take advantage of microfluidics concepts to create an environment where one US pulse can affect four channels, each with its own unique condition. The second component of the project's goal is to measure the effect of the therapy to compare how different US and MB parameters affect ATP release, which is implicated in vasodilation signaling, and cell death.

In this project, we developed tools to assess the cell viability of two different cell lines using fluorescent imaging and to quantify the amount of ATP being released following MB+US therapy, which remains poorly understood.

We report the effect of different US therapeutic pulses in the presence of static MB, on ATP signaling and cell viability, to gain an understating of how the US and MBs affect vasodilation pathways. The work done in this project will help pave the way to better understand how different parameters affect the physiological reactions that cause vasodilation.

This thesis will first provide an introduction and motivation for this project in Chapter 1. A more detailed theoretical background and current state of knowledge will be reviewed in Chapter 2. Then, Chapter 3 describes the methods of ATP and cell viability quantification using bioluminescence and fluorescence. Further, the chapter also describes the design of the multiplexed flow chip. The results of the experiments will be displayed in Chapter 4 and later discussed in Chapter 5.

Chapter 2 Theoretical Background and Literature Review

2.1 Ultrasound and Microbubbles

2.1.1 Ultrasound Physics

Just like audible sound, ultrasound is a pressure wave that can propagate through different media, but it is defined by its frequency above the normal human hearing, typically > 20 kHz. An US wave is further characterized by its amplitude, measured in Pascals, and the speed of sound, which is medium-specific (typically 1540 m/s in water). While propagating, the US wave can be reflected, scattered, or attenuated. Frequencies used in medical US imaging typically vary from 1 MHz to 20 MHz [7]. Clinically, different frequencies are used to image different biological tissues. Higher frequencies (10-40 MHz) are used to image shallow tissues with high spatial resolution but suffer from poor penetration. Conversely, lower frequencies (1-5 MHz) are used to image tissues that are deeper in the body but suffer from a poorer spatial resolution.

2.1.1.1 *Single Element Ultrasound Wave Transmission*

In medical applications, ultrasound is emitted by a transducer made of piezoelectric material. Piezoelectric crystals change their geometry when a voltage is applied. Thus, by sending an alternating voltage into a single element transducer, back and forth mechanical oscillations are created and transmitted to the adjacent media in the form of a longitudinal pressure wave. (Figure 2).

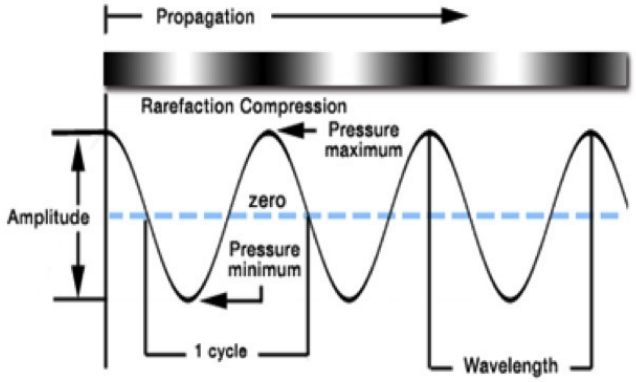

Figure 2 *Illustration of the movement of the ultrasound wave, i.e. a longitudinal pressure wave, across a media. (Adapted from http://www.bats.ac.nz/detail-basic_theory_of_ultrasound-29)*

In this project, the therapeutic US waves were generated at 1 MHz using a single element circular transducer with a diameter of 0.5 inches (A303S, Olympus, Waltham, MA). Near the face of the transducer, constructive and destructive interferences cause a spatially inhomogeneous pressure field. This area is called the “near field” (Figure 3). The near field ends at the natural focal distance (N) of the transducer, beyond which these interferences become negligible: in the “far field” the pressure reaches its maximum amplitude and decreases with the distance from the transducer (z). In the far field, the pressure is spatially homogeneous within a circular region of diameter $\lambda z/D$ (-6dB of maximal pressure). The figure below illustrates the amplitude of the wave in front of a flat transducer, where the focal zone is the line dividing the near and far fields. Here the maximum intensity of the sound wave occurs. The distance of the near field is a function of the transducer’s diameter, the speed of sound in the testing material, and the frequency of the transducer [8].

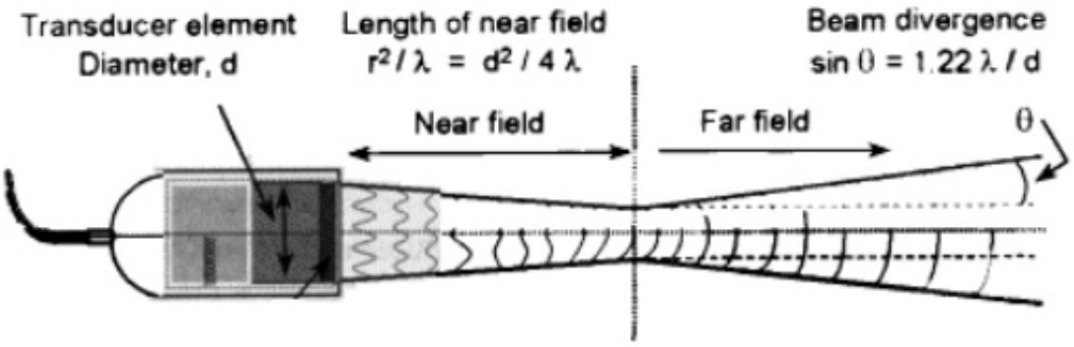

Figure 3 An illustration of how interference creates zones of higher and lower pressure along the path of the US wave. (c.f. Bushberg et al., The Essential Physics of Medical Imaging, p.491).

Where d is the diameter of the element, λ is the wavelength of the transducer and N is the length of the near field. Where

$$N = d^2/4\lambda$$

The flat transducer used in this project has a diameter of 0.5 in (1.27 cm) and a frequency of 1 MHz, this translates to a focal distance of 2.7cm and a -6dB diameter of 0.32 cm.

When the US pulse (a few cycles of oscillations) encounters a boundary of mismatching materials with different acoustic impedance (Z=ρc, where ρ=density and c= speed of sound), the ultrasound wave can be reflected or refracted according to Snell's law (Figure 4). This law dictates the angle of refraction depending on the different speeds of sound of the materials forming the boundary [9].

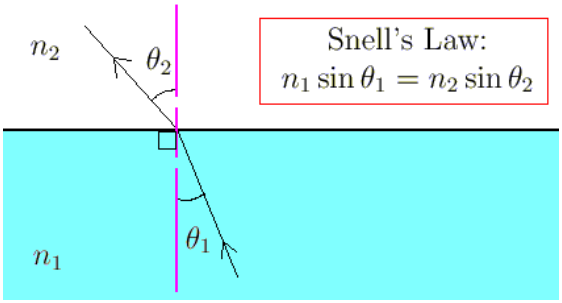

Figure 4 An illustration of how a wave refracts after crossing a boundary between two materials with a different speed of sound. [10]

For US to be efficiently transmitted between two mediums, it is important to match the impedances. Since air and water have a strong mismatch in acoustic impedance, an acoustic gel is used to create a coupling between the probe and the organ of interest [9].

2.1.1.2 Scattering

When an ultrasound wave encounters inhomogeneities that are much smaller than the wavelength, the ultrasound wave is scattered across multiple directions. These smaller particles can be distributed across the medium or across a surface (Figure 5). In an US image, scattering is responsible for the speckle patterns that give tissues a texture. Scattering properties can be used to characterize microstructures, a field known as ultrasound tissue characterization [11]. These properties, for example, have been used to characterize red blood cell aggregation [12] or even characterize thyroid cancer tissue [13].

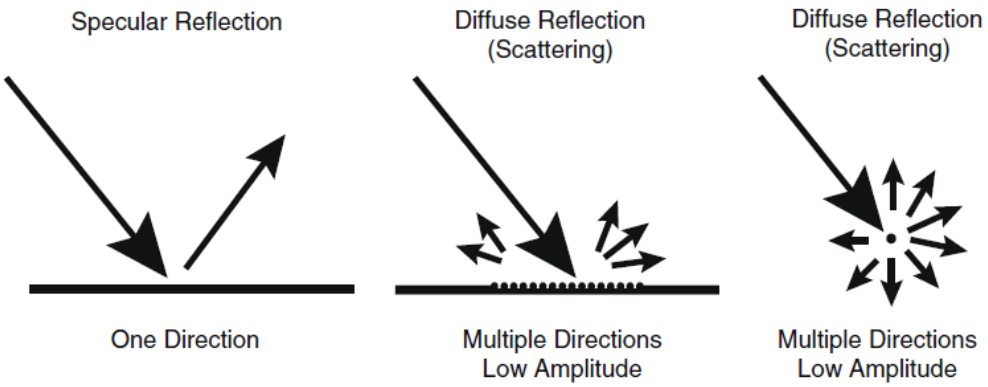

Figure 5 Scattering of a pressure wave depending on the boundary type or on the size of the reflector [7]

2.1.1.3 Attenuation

As a US wave propagates not only does the energy gets dissipated by scattering, but energy is also converted into thermal energy (due to the movement and subsequent relaxation of tissue) [7]. This energy loss is dependent on both the innate properties of the material and the properties of the pressure wave propagating through it, more specifically, the pressure and the central frequency. The energy loss can be characterized by the following equation.

$$A = A_o e^{-\alpha x} \tag{2.1}$$

Where A is the pressure of the sound wave, A_0 is the original pressure, α, measured in dB/(MHz cm) is the amplitude attenuation coefficient and x is the distance traveled by the sound wave [14]. Notice that α is dependent on the central frequency of the wave being applied. Looking at eq. 2.1, US gets more attenuated at higher frequencies and with increasing path length. In the next paragraph, we will describe how US waves can be used to form US images.

2.1.1.4 US Image Formation

In pulse-echo mode, an US pulse is sent into the tissue and the reflected and scattered waves that are backpropagated are amplified and recorded to form a radiofrequency (RF) line that is characteristic of the tissue's acoustic impedance spatial distribution. The log-compressed amplitude of the RF signal envelop form an A-line. Adjacent A-lines form a B-Mode image. By sending a sequence of pulses and recording their echoes, images can be formed. Repeating these pulses over time, images can turn into a video, which is typically around 50-100 frames per second (fps) [15]. As mentioned before, the strength of the echo is proportional to the impedance mismatch of the boundary, this makes stiffer materials like bone very bright in B-Mode images. However, the difference in impedance between blood and tissue is very low, making it harder to image vasculatures.

By injecting an US contrast agent (microbubbles) intravenously (Definity, Optison, and Sonovue are clinically approved), it is possible to image the vasculature as MBs are strictly intravascular agents and remain within vessels. Using clever processing techniques to locate and track microbubbles (non-linear imaging or SVD filtering), images can be formed with exquisite resolutions down to tens of microns in scale [16] as seen in Figure 6.

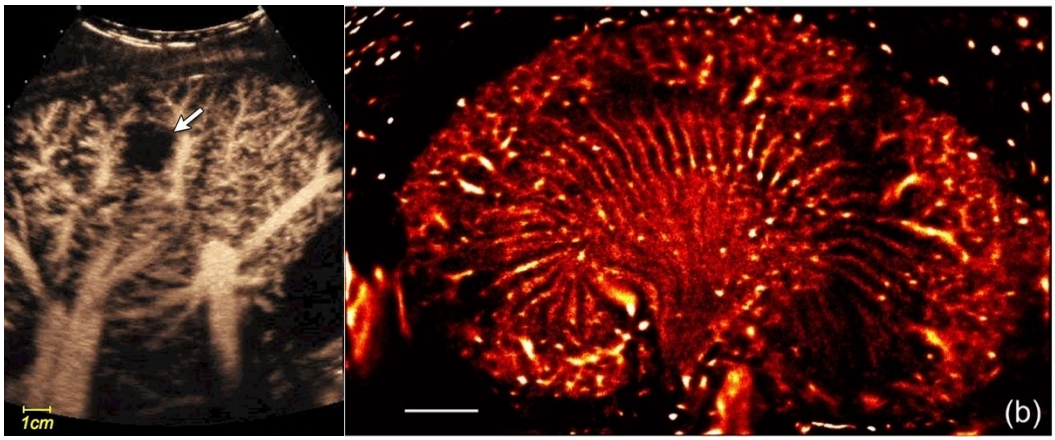

Figure 6 Contrast-enhanced ultrasound image of liver tissue [17] *and an image of super-resolution imaging of a rat kidney* [16]

Further, using burst replenishment imaging, it is possible to quantify blood perfusion. Burst replenishment entails bursting the microbubbles and recording the time it takes for MB to reperfuse the imaging plane (Figure 7). Increases or decreases in perfusion can be detected using burst replenishment, making this method for quantifying vasodilation, fitting for the purpose of this project.

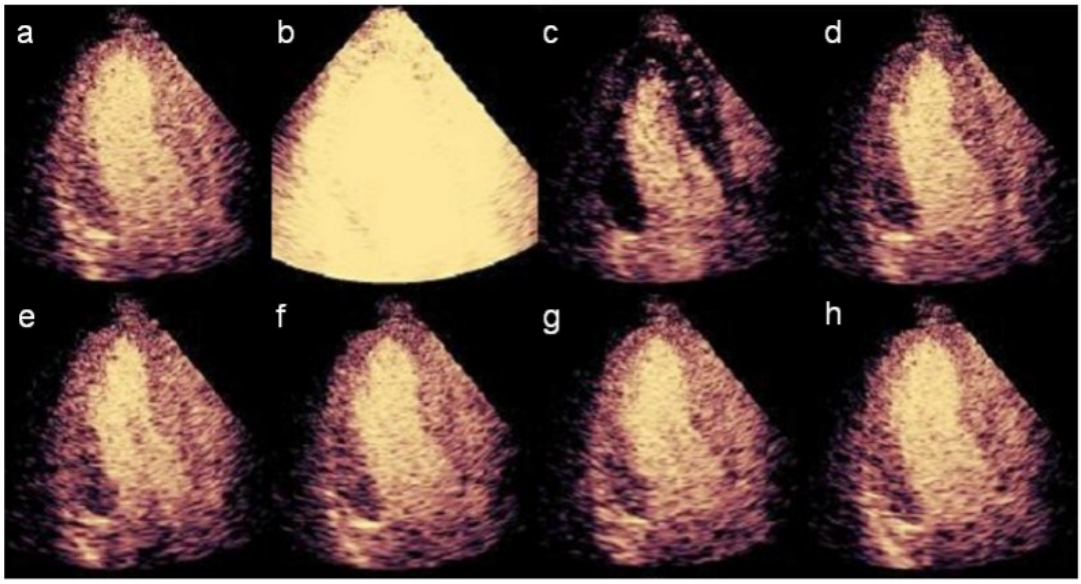

Figure 7 Sonovue microbubbles were intravenously injected into healthy volunteers and an image of the heart. a) shows the image pre-burst, b) during and c-h) show the microbubbles being replenished in the ventricle wall. [18]

2.1.2 **Microbubble Oscillations**

Microbubbles are used as US contrast agents because gas provides a strong mismatch in acoustic impedance. MBs are gas-filled bubbles ranging 0.5-10 micron in size [19], due to the gas inside them, they expand and contract in response to changing pressure in an US field. MB oscillations are described by the Rayleigh-Plesset equations [20], [21]. The microbubble oscillations are frequency-dependent and can resonate in the frequency range used for US imaging. When driving bubbles with low pressures in the order of tens of kilopascals the microbubbles oscillate linearly. However, as pressures increases, the microbubble oscillations start to experience non-linear behaviors ranging from stable (harmonic emissions) to inertial cavitation and microbubble destruction (broadband emissions) [19]. Figure 8 pairs an example US wave with the two different MB behaviours. Notice the osciallitons of the bubbles depending on the pressure of the US wave.

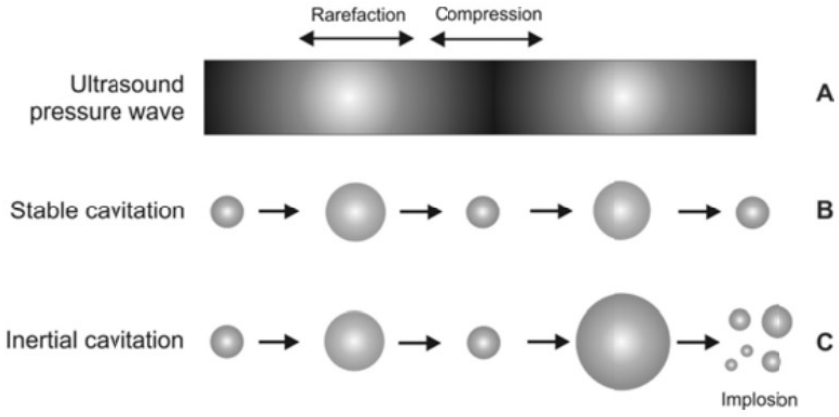

Figure 8 A) A schematic of the pressure variation of the US wave. B and C) The behaviors of a MB under stable and inertial cavitation.[21]

2.1.2.1 Stable Cavitation

In response to an excitation wave at resonance frequency F of higher amplitude (hundreds of kPa), microbubbles can undergo stable cavitation, where the bubble oscillates in size at harmonics (NxF), subharmonics (F/2) and ultraharmonics [(N+0.5)xF] of the fundamental frequency F. During stable cavitation, as the name implies, MBs are resonating at a low amplitude without destruction. The liquid around such oscillating bubbles can start to form micro streams of fluid

moving at a rapid velocity[22]. Fast-moving liquid, if near a cell, can cause high shear stress, normally not seen in regular blood flow and activate mechano-sensitive receptors [21], [23], open gap junctions [24], [25] or enhanced endocytosis [26].

2.1.2.2 Inertial Cavitation

If the pressure is further increased above the inertial cavitation threshold, microbubble oscillations become violent, and the inertial forces of the medium collapse onto the microbubble, concentrating energy focally, resulting in very high shearing forces, fluid jets, and local elevation of temperature and even the emission of light [27]. Some of these jets can be seen in Figure 9. This causes the destabilization of the microbubble shell, leading to the destruction of the microbubble [21], [28]. Microbubbles undergoing inertial cavitation can cause multiple bioeffects including mechanical puncturing of the cell membrane [21], generation of reactive oxygen species [29], calcium waves [30], and release of ATP [31], [32].

MB stable and inertial cavitation can be leveraged for multiple different therapies, such as opening the blood-brain barrier [33], increasing gene delivery into cells [34], [35] or, even increasing drug uptake [36]–[38]. Most pertinent to this project is the fact that US+MB therapy has been shown to locally increase blood flow in muscle tissue in vivo [6], [31], [32]. While the physiological effects of the therapy have been documented, we are interested in understanding the activation of the vasodilation pathway and ATP signaling following MB+US therapy, which remains largely unknown.

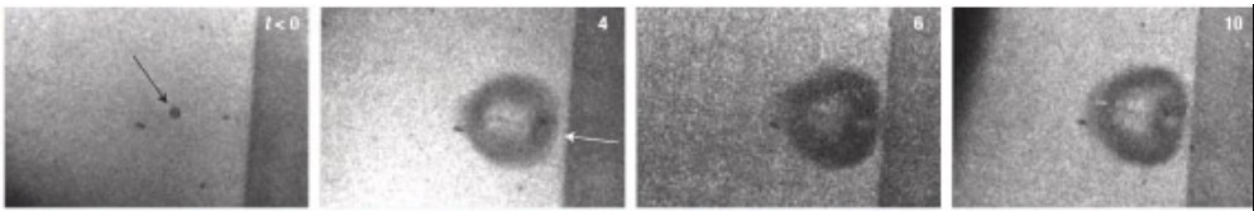

Figure 9 A MB oscillating and causing microjets of fluid seen in the second and third panels. [39]

2.2 **Vasodilation and ATP Release Following MB+US**

Vasodilation is a mechanism that regulates blood flow in organs [40]. Vasodilation and vasoconstriction regulate the temperature inside the body when vessels are near the skin [41], [42] and control oxygenation in muscle tissue [43]. Changes in blood flow are required as metabolic demands change [44]. This is regulated at the level of arteries and arterioles and is coordinated by electrical and chemical signals [44]. One important chemical signaling pathway is the production of nitric oxide (NO) in endothelial cells [45]–[48]. The production of NO in endothelial cells is controlled by the endothelial NO synthase enzyme (eNOS), which converts L-arginine to L-citrulline and NO [47]. eNOS phosphorylation is triggered by flow-mediated shear stress on the endothelial cell wall [49]–[52]. Similarly, increases in shear stress have been shown to release ATP both from endothelial cells [53] and red blood cells [54]. Furthermore, increases in ATP can also activate the eNOS pathway [55], [56] and thus be implicated in vasodilation. It is clear that ATP and the production of NO are linked. Andrews et al. showed that when endothelial cells are exposed to shear stress under flowing conditions an increase in NO can be seen, but when ATP is degraded by apyrase, the production of NO decreases [49]. The cascading effect of ATP release triggering the production of NO can be seen in Figure 10.

As mentioned previously MB oscillations can generate shear stress at the endothelial cell wall. MB+US therapy has already been shown to activate the eNOS pathway in muscle tissue [57]. Furthermore, recent in vitro studies have shown that ATP can be released by both endothelial cells and red blood cells following MB+US insonation [6]. Interestingly, after insonation, ATP signal is still seen after a 20 min delay, suggesting that in addition to the initial burst of released ATP, other mechanisms can sustain the release for longer periods [31]. Indeed, studies in vivo have shown that there is still ATP signal up to 24 hours after treatment in both muscle [31] and the myocardium [32]. In vitro, the ATP is released quickly while in vivo the ATP signal can be seen up to a day after treatment [31], [32], but not in pannexin knock-out mice models [32]. This data suggests that after an initial ATP release by sonoporation, the sustained release of ATP and subsequently, the synthesis of NO, is mediated by purinergic channels such as pannexins.

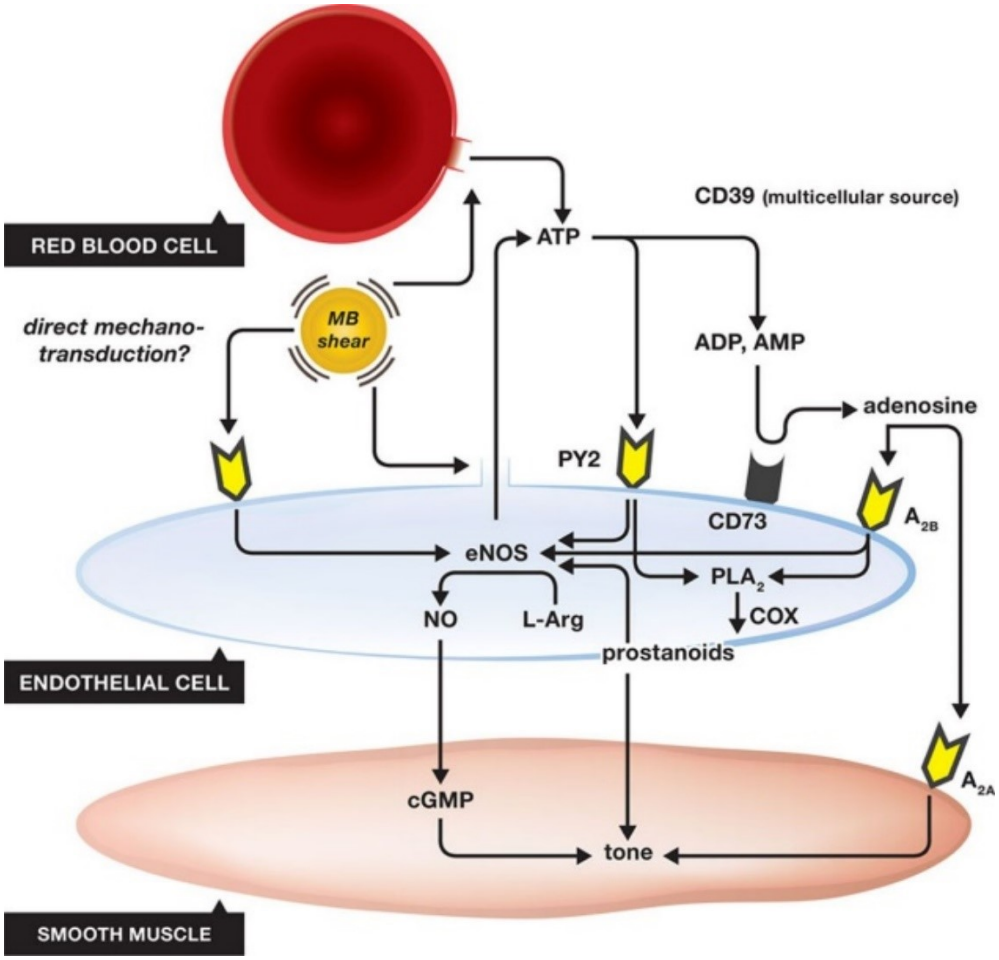

Figure 10 Illustration of the prevalent hypothesis leading to the creation of NO after MB and US therapy. The release of ATP by either an endothelial cell or a red blood cell then leads to an activation of the eNOS enzyme creating NO from L-arg. The NO then diffuses into the smooth muscle cell leading to relaxation and vasodilation. [6]

To further cement ATP as a mechanism for vasodilation, Belcik et al. suggest that the sustained release of ATP is triggered by ATP itself. It has been shown in astrocytes [58], oocytes [59], and glial cells [60] that extracellular ATP can trigger the pannexin channels to release more ATP via the P2Y receptor, as seen in Figure 11. To avoid a positive feedback loop from draining the cells' ATP, it has been found that ATP dosage can also be an inhibitor of the pannexin channels [61]. This leads to the conclusion that there is a feedback loop that can continuously release ATP and can be controlled by the extracellular ATP dosage [62], [63].

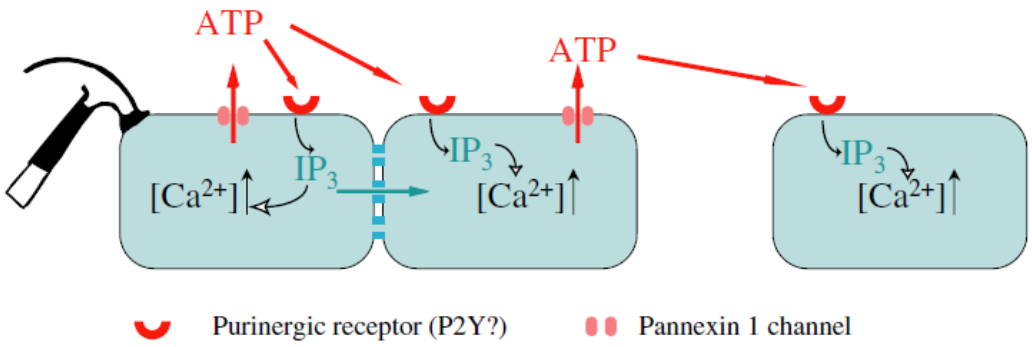

Figure 11 A schematic on how extracellular ATP can induce ATP release through the pannexin channel as activated by the P2Y receptor. [59]

Since the sustained ATP signal is first triggered by an initial ATP release, it is important to describe and understand how cells let out their ATP depending on US and MB parameters. The time course, amplitude, source, and US pulse dependence of the initial ATP release by US and MB therapy remains largely unknown. We set out to investigate the contribution of live and dead cells to the ATP signal following MB+US therapy using a highly sensitive bioluminescence camera and live/dead fluorescence staining.

2.3 In Vitro Studies of Microbubble Cell Interactions

As mentioned before, MBs oscillate under an US pressure wave. These oscillations can cause microstreaming and jet streams of high shear stress [21]. When a MB is oscillating close to cells, the two can interact and the cells can experience a range of biophysical effects [64], [65], including sonoporation, the generation of calcium waves, and enhanced endocytosis.

2.3.1 Sonoporation

In vitro studies have shown that microbubble therapy can open small transient pores on cell membranes, which is called sonoporation. In vitro studies have shown that a single bubble exposed to a 10 cycle 1 MHz pulse can open a pore on the cell membrane [66]. These pores reseal in under 1 minute with a time constant below 20 seconds. However, they also show that some pores are too large (over 100 μm^2) and cannot reseal. Other studies have also shown similar

effects to the cell membrane via microbubble oscillations. Disruptions on the cell's membrane can be seen through scanning electron microscopy [36], [67]–[69] and, whole-cell patch clamping [70]. An example of these resealable pores can be seen in Figure 12.

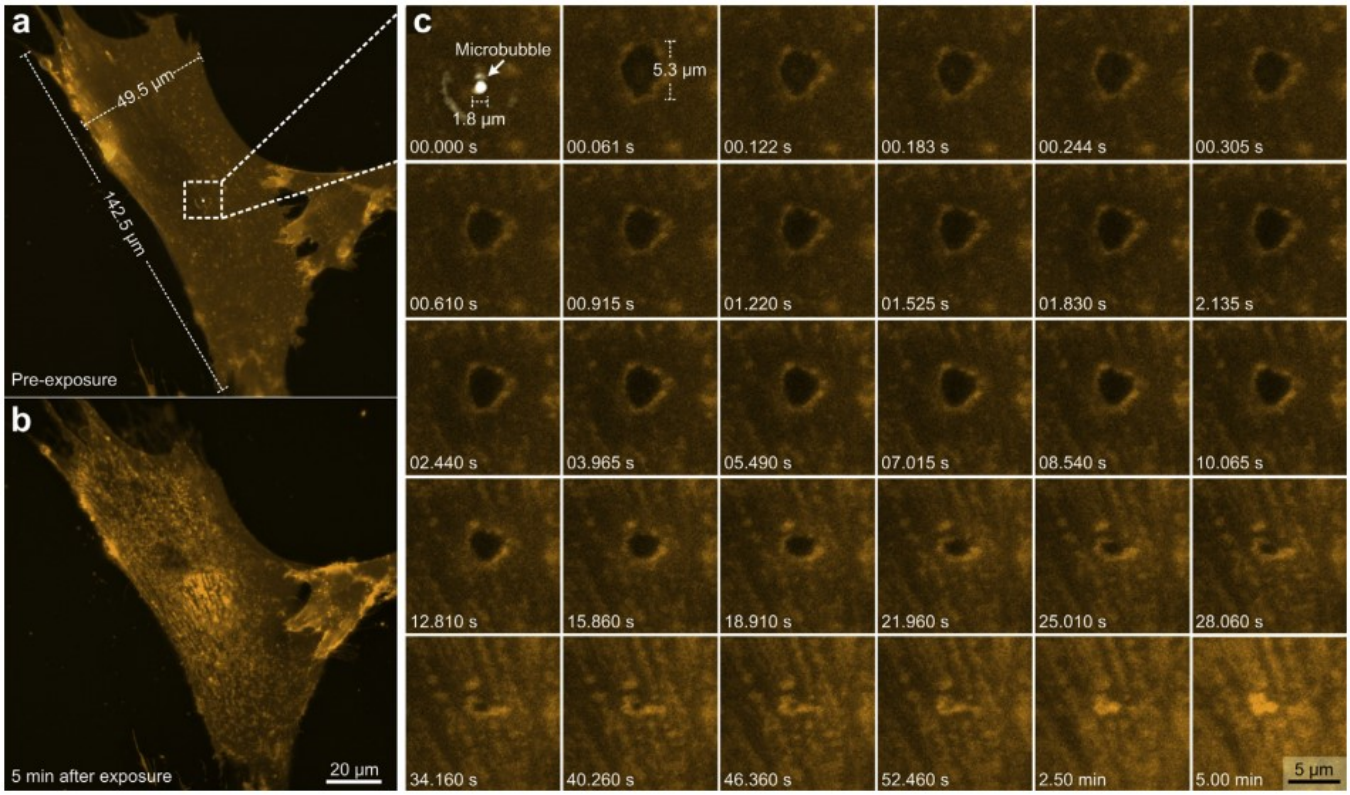

Figure 12 An example of a membrane poration after a cell's interactions with a resonating Microbubble. Note how the pore forms and slowly reseals after 40 seconds. [66]

The basis of most of the therapies, like drug uptake or gene delivery, is the transport of molecules through these pores. They offer a way for impermeable chemicals to enter the cell's cytoplasm while maintaining the cells alive. To image, such intake, a very common fluorescent dye, propidium iodide (PI) is used. This dye fluoresces after binding to nucleic acids (DNA and RNA) and has the advantage that is normally impermeable to cell membranes. PI has been consistently shown to enter cells once they are exposed to resonating MBs [71]–[76]. Note that PI can also be used as a cell death marker as it will label membrane compromised cells. The difference in PI functioning as a drug uptake or cell death marker is dependent on the timing of PI exposure relative to the resealing of the pores.

It is important to note that not every oscillating microbubble can cause a pore to form. There are specific microbubble and ultrasound conditions that allow the pores to form. De Cock et al have shown that at higher pressures of 500kPa there is a prevalence of pores, while at lower pressures, 100 kPa there is a prevalence of cell membrane disturbances [74]. A disturbance was characterized as a change in the cell membrane geometry after treatment. The implication of this will be discussed in Section 2.3.3. Helfield et al have shown that sonoporation is independent of initial bubble size. They show that the main contributor to pore formation is a shear stress threshold, which is related to MB expansion [71]. Van Rooj et al have shown that microbubbles that are being displaced are the main contributors to sonoporation, while static ones rather contribute to cell death [75], which clearly emphasizes the importance of flow.

2.3.2 **Calcium Waves**

The calcium ion, Ca^{2+} is an important intracellular signaling molecule that is implicated in many cellular regulation processes [77]. Pertinently, one of these is the activation of NO synthase in endothelial cells [22], [78]. Controlling the calcium ion levels in cells can help develop a targeted therapy by allowing control over vascular flow [79]. Given the focus of this project, one way of achieving this would be to use MBs. Certainly, oscillating MB has been shown to increase the levels of calcium inside cells they are in contact with. Further cementing MBs as an ideal tool to control vascular flow [80]. It is important to note that the oscillatory behaviors of the MBs are not enough to create calcium fluctuations inside the cell. Beekers et al. showed that the formation of pores is heavily linked to these changes. In their study, they found that after US and MB therapy all of the cells that were sonoporated showed calcium fluctuations; while all of the cells that did not show signs of sonoporation but were still exposed to a resonating MB, had a stable level of calcium [30]. Even more interesting, fluctuations in calcium levels are not limited to cells in contact with the MB. Again, Beekers et al. have shown that adjacent cells (meaning they were not in contact with a MB) also experience calcium fluctuations [30]. Furthermore, they could quantify the speed of the calcium propagation at an average of 15μm/s away from the MB site [30]. This propagation is called a calcium wave. The spatiotemporal distribution of calcium fluctuations after a sonoporation event can be seen in Figure 13.

These findings highlight the complex behavior and reaction to the sonoporation event and how studying a layer of cells can lead to a better understanding of physiological reactions to the US and MB therapy.

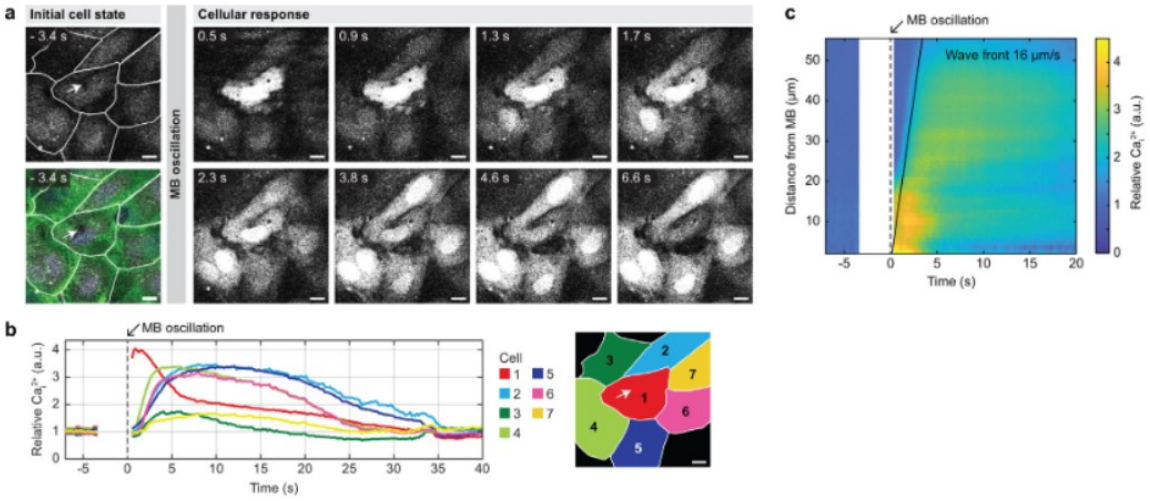

Figure 13 a) An example of a single MB sonoporation of a cell followed by a calcium fluctuation and the delayed calcium fluctuation in the adjacent cells. b) Calcium signal in each of the segmented cells over time. c) The signal as a function of distance and time. It clearly shows that locations further from the MB, experience a delayed calcium fluctuation [30].

2.3.3 **Enhanced Endocytosis**

As discussed before, drugs and molecules that are cell impermeable can be transported into the cell via the small pores caused by the US and the MB therapy. However, the therapy can also induce endocytosis of large molecules without puncturing the cell membrane. For example, Nejad et al. sonicated a single cell in close contact with a linearly oscillating microbubble to examine the behavior of the cell's geometry and its downstream enhanced permeability. They discovered that even without puncturing a hole in the cell's membrane, PI, normally impermeable to live cells, still entered the cell [81]. Proof that there exist more pathways of enhanced permeability other than sonoporation. To understand the pathways different sized molecules (4.4-500 kDa) take when entering cells after US and MB targeted delivery, Meijering et al. studied their fluorescence and colocalization with important endocytic proteins [26]. Their results showed the smaller molecules (4.4 -70 kDa) spread homogeneously inside the cell while larger ones (155-500 kDa)

localize in smaller vesicles, pointing towards different mechanisms of uptake. When depleting ATP to inhibit endocytosis pathways, no uptake of the 500 kDa dextran and a significant decrease of the 4.4kDa molecules were seen. Even more, fluorescent microscopy showed colocalization of the large dextrans with caveolin-1 and clathrin [26]. This means that larger molecules localize themselves with important proteins in the endocytosis pathways. Similar results are shown with DNA plasmids and clathrin in vitro [82]. Concluding that while poration of the cell membrane leads to an influx of smaller molecules, endocytosis is the main pathway for larger molecules.

These mentioned studies examine the behaviors using a single US and MB condition. De Cock et al. set out to investigate the role the US pressure has on endocytosis and sonoporation[74]. Using confocal microscopy, membrane dyes, and PI as a poration marker, they could assess the changes in cell membrane morphology and cell sonoporation. As mentioned before, their findings showed that greater acoustic pressures cause more pore formation and fewer membrane deformations. While the opposite is true for lower pressures, where a higher percentage of cells went through membrane deformations. They linked these differences in the cell's reactions to enhanced endocytosis by assessing the uptake of small (4 kDa) and large (2MDa) fluorescent dextrans. Similar to previous results, uptake of these dextrans could be split as localized uptake, as a marker of endocytosis pathways, or diffuse and homogenous uptake, signaling entry into the cell via a pore. They show that just as with membrane deformation and pore formations, as acoustic pressures increase, the population of cells shifts towards the high-intensity diffuse uptake, meaning pore formation. They conclude that membrane deformations mechanically activate the cytoskeleton of the cell to enable enhanced endocytosis.

Note that varying acoustic pressures lead to different cellular reactions. This shows that to understand and tune US and MB pulses for therapy, a wide variety of conditions need to be tested. Contextualizing the need for a multiplex platform to test many US and MB conditions at once.

While sonoporation, calcium waves, and enhanced endocytosis have been described, very few groups have studied the release of ATP following US and MB therapy, and more importantly, no one has quantified the molar amount of ATP after therapy. The following section will shed light

on the methods used in this project to quantify ATP and to link its release to cell viability after therapeutic pulses.

2.4 **Microscopy and Imaging**

In this project, we used two microscopy tools to image cells and their behaviors: fluorescence and bioluminescence.

2.4.1 **Fluorescence**

Fluorescence is a phenomenon where molecules absorb and emit electromagnetic radiation. Molecules that exhibit this behavior are called fluorophores. These molecules normally emit light at a lower energy level than what they are excited with. Microscopes are built with filter cubes containing a dichroic mirror and two filters delimiting excitation/emission wavelength combinations that are adapted to each fluorophore. The excitation filter allows the excitation bandwidth of light to pass through. This light is reflected by the mirror, reaches the specimen, and excites the fluorophores, which in turn emit light at a lower bandwidth. This emitted light is caught by the microscope lens, passes through the mirror and the emission filter, and is fed into a camera or to the eyepiece. Using this configuration, the microscope can excite the specimen with a narrow band and collect only the signal coming from the fluorophores.

This project uses three fluorophores to image cellular structures and to test for cell viability. Calcein Acetoxymethyl (Calcein AM) is a nonfluorescent molecule that is permeable in live cells. Once the Calcein AM goes into the cell, the Acetoxymethyl is cleaved off by intracellular esterases. Once cleaved, Calcein becomes a fluorescent molecule with peak excitement at 495nm and peak emissions at 515nm (green). Since esterases are only functional in live cells, Calcein AM is a marker of live cells.

Propidium iodide (PI) is a common fluorescent marker that tests for cell death. It cannot cross the membrane and is thus not permeable to live cells. PI becomes highly fluorescent once bound with nucleic acid and typically binds to nuclear DNA of membrane compromised cells. PI has a peak excitation of 493nm and a peak emission of 636nm (red). The large time difference between the reversible effect of sonoporation (around 1 min) and the time between treatment of the cells and

PI exposure (30 min), we are confident that PI stained cells are membrane compromised and are likely to be dead cells.

Hoechst is a cell membrane-permeable dye that also binds to DNA. It is used to stain the nucleus of the cell. It is excited by light of 460nm and emits light of 490nm (blue). We use Hoechst to count the numbers of cells.

2.4.2 **Bioluminescence**

Rather than introducing energy into a system via light, there is a chemical process that naturally produces light. With a sensitive enough camera detection system, this light can be collected and analyzed. For this project, the chemical reaction is one of Luciferin, Luciferase, and ATP. Luciferase is an enzyme that can convert the Luciferin protein into light and other products when ATP is present. Using conditions in which ATP is the rate-limiting factor, it is possible to quantify the instantaneous ATP concentration using this system. Compared to fluorescent images used in this project to assess cell viability, the light emitted by the ATP reaction is imaged as the reaction happens with the signal decreasing over time as reagents are consumed (Figure 14). Capturing the light created by this reaction is a challenging process. This is due to a dim signal being produced by the reaction when compared to fluorescence [83]. Furthermore, the fluorescence signal can be increased by simply increasing the excitation light but the bioluminescent signal is limited by the number of substrates to catalyze the enzyme [83].

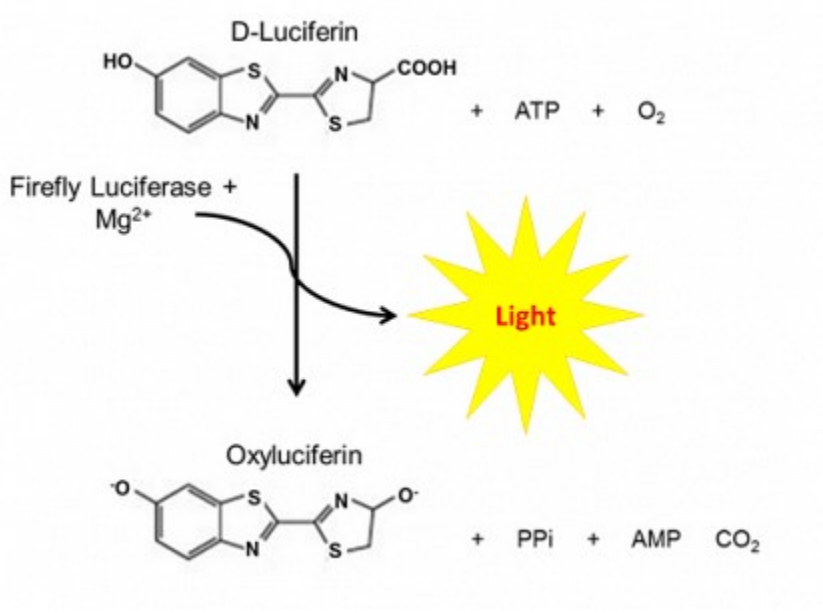

Figure 14 Illustration of the conversion of ATP into light [84].

A luminometer can be used to capture the light and output a single value reflecting the average released ATP in a well. While useful, using a luminometer only provides a number count of photons counted as an output rather than an image. Another way to capture enough photons of light is to use a scanning system to systematically scan a certain area for a certain period (~1 sec). This technique has been used to image ATP release in vivo [6], [31] but it lacks time resolution, making it hard to study bursts of light.

The novel way used in this project was proposed by Tan et al. [85]. Here, we used a sensitive camera, more specifically, an electron-multiplying charge-coupled device (EMCCD), with a widefield configuration using a low magnification (0.33 X) that collects light over seconds. This camera, set up with a low magnification and a high numerical aperture, increases image brightness. Furthermore, the device collects all of the light rays that are traveling parallel to the camera, often called infinity space, thus increasing the signal-to-noise ratio and allowing detection of ATP in the fmol range. Benefits to using such a setup include a high time resolution (1s) and spatial resolutions of ~78µm/pixel [85]. This allows us to study ATP release kinetics. One of the limitations of using this method is that the spatial resolution is not sufficient for imaging individual cells.

Literature shows that we can use microfluidic structures as tools to not only cultivate cells and have them interact with bubbles but more importantly, to quantify the cellular response to US and MB therapy.

2.5 **Microfluidic Structures**

The field of microfluidics has been growing in the past decade peaking at around 1500 papers per year [86]. Unsurprisingly, of the papers covering microfluidics, around 85% of them were published in engineering journals. However, between 2002 and 2012 the percentage of publications in biology and medicine journals rose from 6% to 9% [86]. This shows that microfluidic structures have started to emerge as a great option for cellular and biological models. These types of devices, often called lab on a chip or organ on a chip, offer versatile and adaptable options for in vitro cell culture and biological studies. Advantageously, given their small size, the amount of material, cells, and expensive reagents become quite accessible [86]. However, one important advantage of these microfluidic devices is that they can be used to introduce flow inside their chambers. Compared to cell plates and other biologicals tests typically performed in static conditions or requiring the collection of a sample, microfluidic systems allow perfusion of liquids and therefore can be easily used to mimic in vivo conditions. Moreover, microfluidic devices can be easily manufactured and adapted for many uses, such as testing drugs for micro-dissected tumor tissues [87] or used as a multiplexing platform for testing chemotherapy in spheroids [88]. By making the devices transparent, microscopy and bioluminescent studies can be performed in them. Polydimethylsiloxane (PDMS), is an ideal material to use for the chip. It is a common material used in microfluidics for its flexibility, transparency, and gas permeability. This makes it ideal for manufacturing chips that allow cell culture.

2.5.1 **Fundamental Physics**

In general, microfluidics encompasses the study of fluids in the microliter to nanoliter range within the field of fluid dynamics. The fundamental equations for dealing with microfluidic flows are the conservation of mass, energy, and momentum. The conservation of mass yields the first

governing equation of microfluidics, the continuity equation. The conservation of momentum yields the Navier-stokes equation[89]. For an incompressible fluid the Navier-Stokes equation is as follows [89]:

$$\rho[\partial_t \boldsymbol{v} + (\boldsymbol{v} \cdot \nabla)\boldsymbol{v}] = -\nabla p + \eta \nabla^2 \boldsymbol{v} + \rho \boldsymbol{g} \tag{2.2}$$

Where ρ is the density of the fluid, $\boldsymbol{v}$ is the velocity as a function of space and time, p is the pressure field across space, η is the viscosity of the fluid and $\boldsymbol{g}$ is the acceleration due to gravity.

In layman's terms, it resembles Newton's second law of motion. On the left side, the intrinsic inertial forces can be seen, such as the density of the fluid and its acceleration. On the right, the sum of the external forces such as gravity, pressure, and friction are seen. Since there are infinite ways to solve this partial differential equation, solving it for a particular system requires boundary and initial conditions.

One way to generalize this long partial equation is to make it dimensionless. This will allow us to gain some intuition on how different setups compare to each other and what to expect from certain conditions. The first important dimensionless number is the Reynolds number (Re). It is calculated by adding two characteristic variables, the length, and the velocity. To make time dimensionless we divide the time variable over the characteristic length and multiply it by the characteristic velocity. Making pressure dimensionless is done by multiplying the viscosity of the liquid with the characteristic velocity and dividing it by the characteristic length. Which yields the following equations [89]:

$$Re\left[\tilde{\partial}_t \tilde{\boldsymbol{v}} + \widetilde{(\boldsymbol{v} \cdot \nabla)\boldsymbol{v}}\right] = -\tilde{\nabla}\tilde{p} + \tilde{\nabla}^2 \tilde{\boldsymbol{v}} \tag{2.3}$$

$$Re = \frac{\rho V_0 L_0}{\eta} \tag{2.4}$$

Where V_0 and L_0 are the characteristic velocity and length.

Re is used to distinguish laminar and turbulent flow. Flows with Re>2000 [90] are considered turbulent; flows with Re <2000 are laminar. Notice that this number is proportional to the

characteristic length of the system. In the microfluidic context, this length is in the micron range, making the Reynolds number much lower than one. Physically, this translates to highly laminar flows inside microfluidic structures. Even further, in flows with Re<<1 are inertia-free, or viscous driven. These conditions are classified as the Stokes flow regime. This consideration is discussed in section 2.5.2.

By applying boundary conditions to the Navier stokes equations it is possible to spatially characterize the velocity along a channel. For example, let a simple channel that runs parallel to the x-axis and has an arbitrary cross-section across the yz plane. Assuming that there is no change in gravitational forces and that the system is under steady-state conditions, the flow is then driven by a differential pressure along the x-axis. By further assuming a no-slip condition, we arrive at a known flow state named Poiseuille flow, described by the following equation [89]:

$$\eta\left[\partial_y^2 + \partial_z^2\right] v_x(y,z) = \partial_x p(x) \tag{2.5}$$

Notice that to obtain this equation there was no imposition of channel geometry, it was achieved using spatial and temporal boundary conditions. To further solve this, geometric conditions can be applied to obtain the following velocity profiles along the y and z-axis. For a circular cross-sectional area, with a radius a, and a length of L.

$$v_x(y,z) = \frac{\Delta p}{4\eta L}(a^2 - y^2 - z^2) \tag{2.6}$$

A rectangular cross-sectional area is also obtained, with y ranging between ±w/2 and z in the range of 0 to h.

$$v_x(y,z) = \frac{4h^2\Delta p}{\pi^3 \eta L} \sum_{n.odd}^{\infty} \frac{1}{n^3}\left[1 - \frac{\cosh\left(n\pi\frac{y}{h}\right)}{\cosh\left(n\pi\frac{w}{2h}\right)}\right]\sin\left(n\pi\frac{z}{h}\right) \tag{2.8}$$

$$for\ rectangular\ channles\ wih\ h < w$$

Integrating the velocity profiles gives us the flow rate across the cross-section of the channel. The rectangular cross-section flow rate is approximated by the following equation [89]:

$$Q \approx \frac{\left(1 - .63\frac{h}{w}\right) h^3 w}{12\eta L} \Delta p \tag{2.9}$$

This is an approximation, as the integral of Equation (2.8) yields an infinite series. Equation 2.9 is a convenient closed form solution to the integration of the velocity profile. This approximation gets better as the ratio of the height to the width approaches zero. In the worst-case scenario where the ratio is equal to one, (i.e. a square cross-section) the error of the flow rate is 13% [89]. Notice that the change in pressure and the flow rate are linked proportionally by a constant dependant on the geometry of the channel and the viscosity of the liquid. This constant is called the hydraulic resistance and is analogous to Ohm's law. Moreover, combinations of channels can be analyzed with an electric analog. This opens a new toolbox that can be used in microfluidics to create systems with similar characteristics to an electric circuit and can be solved just the same way using Kirchhoff's laws. The most pertinent equation to this project is the hydraulic resistance of a rectangular cross-sectional channel [91].

$$R_{hyd} = \frac{12\eta L}{\left(1 - .63\frac{h}{w}\right) h^3 w}, \quad h < w \tag{2.10}$$

2.5.2 **Mixing in Microfluidics**

As mentioned above, flows in microfluidic devices are highly laminar. Under these conditions, mixing happens through diffusion rather than through eddies and other turbulent structures. This means that mixing occurs at a very low pace [92]. To get an idea of how long two fluids will mix in a microfluidic channel, another dimensionless number can be useful, the Peclet number (Pe) [92]. In channels with lateral mixings the Peclet number is defined as follows:

$$Pe = \frac{V_0 w^2}{DL} \tag{2.11}$$

Where V_0 is the average velocity of the fluid, w is the width that the fluid is diffusing, L is the length of the channel, and D is the diffusion coefficient.

The Peclet number quantifies the importance of convection relative to diffusion [92]. It is defined as the diffusion time over the convection time [92]. If the Peclet number is far greater than one,

the time it takes for the fluid to mix by diffusion is far larger than the convection time. Pe >>1 often happens in microfluidic devices due to the small widths and the slow velocities. In order to mix two liquids in microfluidics, the solution is often to include micromixers to induce turbulence.

There is a range of active and passive designs that can help mix highly laminar flows. Active designs include a separate mixing source like acoustic pressure [93], thermal actuation [94], or even a magnetic force [95]. Passive mixers, like their names imply, are static structures that increase chaotic flows, contact time, or contact area between the mixing liquids [96]. Within this category, we can further split the mixing options into planar flow and 3D induced flow. 3D structures include out-of-plane folding structures [97] or stacking and recombining [98]. In-plane flow can include structures like the tesla mixer [99], intersecting channels, [100], or even channels with ridges [101]. The tesla mixing unit (Figure 15) is a great in-plane mixing option for 3D printed microfluidics, making it a great choice for this project [102], [103].

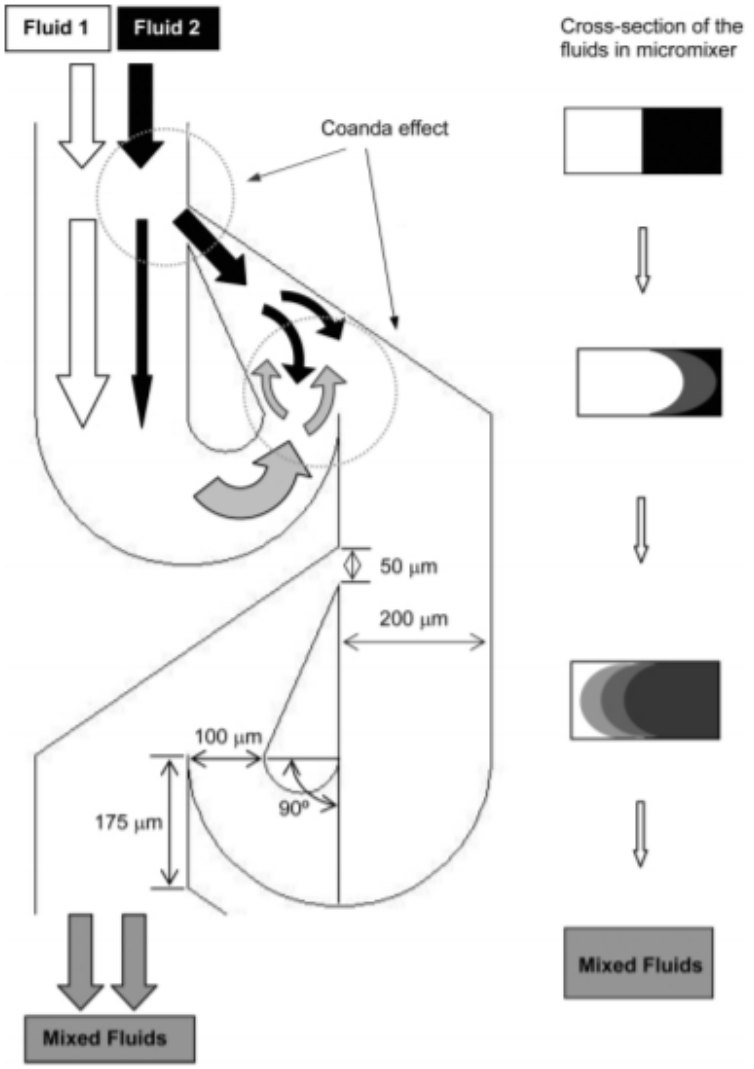

Figure 15 An illustration of how a modified tesla valve can function as a passive mixer in microfluidics [99].

2.5.2.1 Diffusion Estimation for MB Sized Particles

To the best of the author's knowledge, no study has been made to empirically measure the diffusion coefficient of MBs. In order to calculate the Peclet number for MBs, the Stokes-Einstein equation was used. This equation applies to spherical particles in a low Reynolds flowing condition. It is given by equation 2.12.

$$D = \frac{kT}{6\pi\eta r} \tag{2.12}$$

Where k is the Boltzmann constant, T is the temperature in kelvin, η is the viscosity of the fluid and r is the radius of the particle. For bubbles 2µm in radius at a temperature of 300K and a viscosity of .001 Pa s, the estimated diffusion coefficient is 2.09E-13. Such a low diffusion coefficient makes the Peclet number a lot larger than one. Further highlighting the need to include a mixer in the microfluidic chip design.

2.5.3 **Input Flow Options**

Microfluidic channels can accept flows from multiple sources. Capillary pumps have been designed to pump fluid up channels using the capillary pressure of liquids [104]. Even gravitational flow can help drive the liquid through these channels [105]. Peristatic pumps and bubble traps have been used to culture cells under flowing conditions [80]. The simplest flow solution to implement is a syringe pump [106].

2.6 **Microfluidic Chips to Study MB/Cell Interactions**

Using microfluidics, researchers can design and control small environments with optically transparent closed systems. For single-cell experiments, microfluidics allows for highly controlled bubble placement and single-cell interactions between the bubbles and the cells [107]. For example, trapping a single cell in a microfluidic structure to interact with microjets coming from a bubble activated by ultrasound [108]. Moving towards more complex systems, a monolayer of cells or adherent cells can offer structures that resemble in vivo conditions. These are very often used in sonoporation studies [107]. Cell monolayers can give insight into cell viability, gene transfection, and drug uptake [107]. For example, Yong et al. have shown an increase of 42% genre transfection rate in B- cell lines over conventional transfection using cell monolayers [109]. Furthermore, cell monolayers have been used to study cell detachment caused by cavitating microbubbles [110].

However, even endothelial cell monolayers meant to mimic in vivo conditions are still too simplistic to actually mimic the three-dimensional structure and multi-cell systems that occur in vivo [107]. Even the presence of a rigid wall can affect the behavior of microbubbles, which is a

limitation to the ability of these monolayer models to adequately mimic in vivo conditions [111], [112].

Researchers have been getting closer to mimicking in vivo conditions with 3D vessels and multicellular systems[107]. For example, Zheng et al. have created a collagen-coated 3D microvessel with endothelial cells that show angiogenesis [113]. Closer to the scope of this project Juang et al. have shown that it is possible to create 3D structures of endothelial cells to study sonoporation [106]. To the author's knowledge, microfluidic chips have never been used to study ATP signaling following MB/cell interactions.

Chapter 3 Methods

3.1 Microfluidic Device, Conception, Manufacturing, and Validation

3.1.1 Goals and Requirements of Microfluidic Chip Design

In this project, we were interested in developing an in vitro platform to study microbubble cell interactions. We wanted to develop a microfluidic chip compatible with cell culture, acoustically transparent, optically transparent and that could accommodate flow to mimic MB replenishment and thus allow multiple pulse therapy, similar to the conditions used in vivo in which multiples pulses are given sequentially.

We established that the microfluidic chip had to have the following six requirements:

1. The device should allow US pressure waves to pass through without attenuation
2. The device should allow for microscopy and bioluminescent studies
3. The microfluidic chip should allow a monolayer of any cell line to grow confluently
4. The monolayer of cells should have a way to interact with the microbubbles
5. The microfluidic chip should allow for cells to experience a flowing medium with microbubbles
6. The device should multiplex at least one parameter

The final design of the microfluidic chips can be seen in Figure 16. To help illustrate each design choice and how the microfluidic structures fulfill the design requirements, the chip was divided

into three sections: the divider (pink), the mixer (blue), and the testing area (green). These are highlighted in Figure 16.

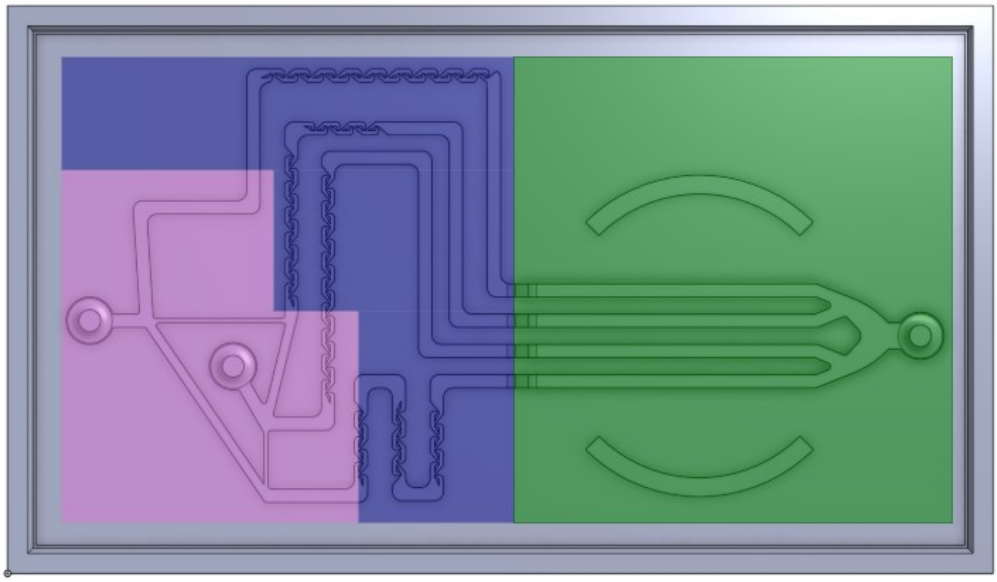

Figure 16 A top view of the mold for the microfluidic chip. The concentration divider is highlighted in pink. The micromixer is highlighted in blue. The testing section is highlighted in green.

The next paragraphs describe the design choices that were made to fulfill all the requirements.

3.1.1.1 Polydimethylsiloxane (PDMS)

Microfluidic chips can be manufactured with many materials such as glass or PDMS (Polydimethylsiloxane). Glass has a high impedance mismatch with water, which would not allow the US to pass through, and was eliminated as a material candidate. PDMS has a low US attenuation coefficient and is optically transparent, can be molded, and is a biocompatible low-cost material [114]. Hence, by manufacturing the chip solely from relatively thin PDMS, requirements 1 and 2 will be met. For verification, the attenuation of pressure waves across the PDMS will be measured.

3.1.1.2 Fibronectin Surface Coating for Cell Culture

For cells to grow in the microchannels, they need a surface to attach to and sufficient media to feed them while they attach and spread. However, PDMS is not the most suitable for cell growth

and attachment due to its hydrophobicity [115]. To help cells attach to the surface of the channel, different proteins can be used, including collagen and fibronectin. By precoating the channels with fibronectin (100 µg/mL) [76], [116], we have been able to culture cells into a confluent layer in our PDMS chips. To increase the volume of media in the cell culture section of the chip, the height of the channels was increased to 700 µm, compared to 150 µm in the other sections. The microfluidic chip accepts a total of 55µL of media to feed the cells during their incubation. This fulfills requirement 3.

3.1.1.3 Cell Culture on the Roof of the Flow Channels

Naturally, cells settle down because of gravity. Inversely, microbubbles tend to float to the top. This poses a problem where intervention is needed for floating MBs to interact with cells. This dilemma was fixed by culturing the cells on the "roof" of the channel. This is achieved by flipping the chip in a "roof side down" position during the cell growth phase. To maintain culture media in the flow channel and avoid media evaporation, the chip was flipped into a puddle of feeding media in the bottom of a petri dish. The chip was then flipped again, "roof side up", before experimentation. Using this technique, when microbubbles were injected into a "roof side up" chip, they floated to come into contact with the cells. More details are available in section 3.2.1 Cell Seeding. The chip has two entry ports that accept a metal adapter, 1 mm in diameter that allows a standard syringe and "catheter" to be used in conjunction with a syringe pump to inject fluid at a range of rates into the channel, ranging from 3-26 mL/ min in arteries [117] down to 33 µL/min flow rates in the smallest arterioles [118]. This way the microfluidic chip allows a cell monolayer to be in contact with both static bubbles and flowing bubbles, thus fulfilling requirements 4 and 5.

3.1.1.4 Multiplexing key Parameters of MB/Cell Interactions

We explored different parameters that are known to be important in MB/cell interactions, including US pressure, microbubble size, microbubble concentration, and flow speed.

We considered creating an US pressure gradient using a sloping PDMS material with different thicknesses to attenuate the initial US pressure and have a continuous pressure gradient across the flowing channels. However, calculations showed that the difference in PDMS thickness (>1

cm difference in height) to achieve a scientifically meaningful pressure gradient was too high, and the pressure was dropped as a variable. For example, to obtain a 60% drop in pressure, we would need a 3cm change in PDMS thickness.

We also considered sorting MBs by size, which could be achieved by using a parallel microfluidic structure like the one designed by Kok et al. [119]. A parallel structure would entail designing and manufacturing a complex 3D structure and that falls off from the scope of the project.

Multiplexing the flow speed could be done by adjusting each of the channels' cross-sections, or by varying the flow rate at the pump side. Due to the ease of changing the flow with other components, we decided that making flow the variable to multiplex would not be as innovative and could be tested in other ways.

Therefore, the candidate selected to be multiplexed was the concentration of microbubbles. Using tools from microfluidics like the electric circuit analog for hydraulic resistances, we can achieve parallel channels with four different (100%, 70%, 30%, and 0%) concentrations ranging from an initial MB concentration (100%) to a control channel without microbubbles (0%). The setup included two entry ports (MB and media) and one output port. Eventually, this chip could be used to titrate drug concentration. Another restriction is the use of the US probe. The probe has a diameter of 1.27 cm and all channels must be within the US probe -6dB focal diameter (0.32 cm) at a distance of 2.7 cm so the experiment can be done under the same US pressure. This was miscalculated as 0.6cm and will be rectified in future chip design (see Discussion 5.1.1.1 -6dB US area)

3.1.1.5 Further Design Considerations

Further into consideration were the manufacturing limits of the chip. This device is made using PDMS poured into a 3D-printed mold. The 3D printer available has a maximum area of 35mm by 55mm, constraining the chip to fit within the area. A further consideration was to include a 200µm spacing between parallel channels to help with demolding. A 7-degree chamfer to the side was also included for the same reason. Features smaller than 50 µm were avoided, and the height of all components was multiples of 50µm as the printer yields the best results with that slice height. More details will be provided in the manufacturing section below.

3.1.2 **Design Formulation and Methodology**

The design of the chip was divided into three sections: the concentration divider, the mixer, and the testing area. Each was developed sequentially and has different design constraints. The concentration divider has the sole purpose of dividing the microbubbles into 4 different channels. The mixer is in charge of getting the output from the concentration divider and making the three channels with MBs to be spatially homogeneous. The testing area had to be designed to make all four channels fit into the -6dB circle of 0.32cm in diameter (was miscalculated as 0.6cm. This will be rectified in future designs). Also, this area required a healthy monolayer of cells. Each channel in the testing area had the same flow rate and only differed in the concentration of MBs.

3.1.2.1 Concentration Divider

The first section of the chip included two input ports. One carrying the microbubbles and the other the dilutant. The design would split each of these inputs into three and then connect the six total branches in such a way to create four different microbubble to dilutant ratios. To ensure that the concentration divider worked as designed, an electric circuit analog was created (see section 3.1.3).

3.1.2.2 Mixer Options

A couple of mixer options were available from literature reviews. To avoid bubble trapping in 3D flow, all nonplanar options were discarded. This left multiple ideas, like expanding and contracting channels or the tesla mixer. The same literature shows that the tesla mixer was the most effective at homogenously mixing two fluids [120] [99], hence the inclusion of this design in the final version of the microfluidic chip. One caveat to using the tesla mixer is that the resistance of each individual unit is not fully comprehended and complex computational fluid dynamics simulations would be needed to obtain a value for the hydraulic resistance of a mixer [121]. As explained in the Electric Circuit Analog (3.1.3) section of this chapter, one of the constraints chosen was that all of the resistances past the concentration divider had to be equal; meaning that the channels with either the initial concentration of MBs or the control channel with no MBs still had to include the same mixer design to account for the unknown resistances of the tesla mixer. The number of

individual tesla mixers was decided empirically, starting with 6-tesla units and moving on to 9 since not all channels were homogeneously mixed.

3.1.2.3 Testing Section

There are two important constraints to this section. One, all of the four channels should fit within the 0.6 cm diameter (will be corrected to 0.32cm in future designs). Second, the cells have to create a confluent monolayer inside the channel. While the first one is a simple design restriction and needed some design thoughts, the overall separation between the four channels was a simple enough goal to achieve. Furthermore, to ensure a repeatable US probe location a circular geometric shape was included in the mold. This feature does not house any cells or liquids and its purpose is to guide the user when placing the US probe on the chip during experiments. As discussed later on, one design constraint imposed onto the concertation divider and the mixing sections was a channel height of 150µm. Using this height in the testing section left little media and thus little nutrients for the cells to consume, so a cell monolayer was not possible. To remedy this, only in the testing section the height of the channels would be 700µm, the implications of this are discussed later.

3.1.3 **Electric Circuit Analog**

Like many other microfluidic products, an analog electric circuit was used to model the fluidic resistances inherent to these devices. The circuit is shown in Figure 17. A total of ten resistances and two input currents needed to be solved by imposing some design constraints.

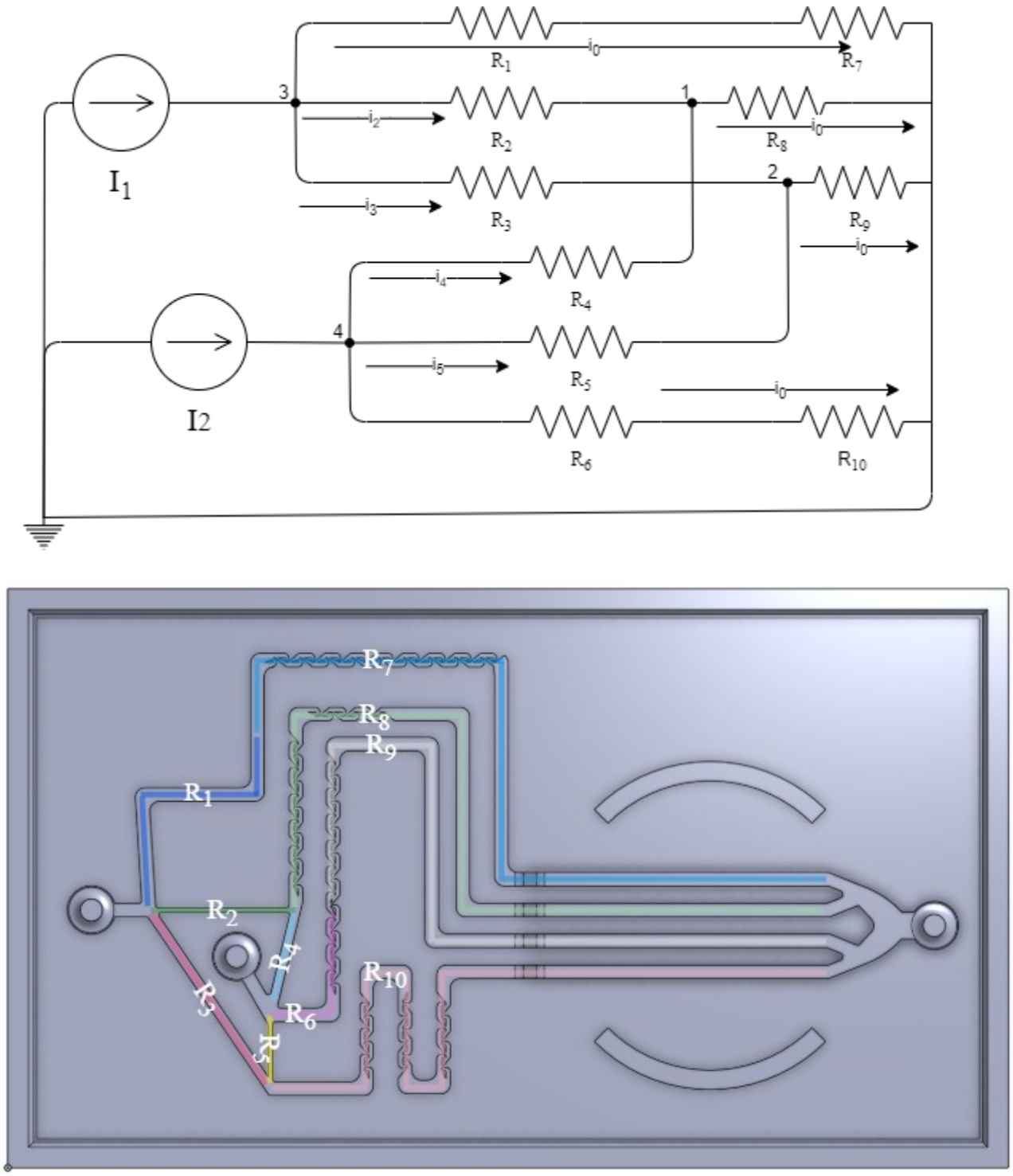

Figure 17 Top- An electric circuit analog to the microfluidic elements. Two input currents that branch into three sections each, which then join to form four equal branches. Bottom- The physical equivalent of the electric resistances.

To relate this to the physical system, Figure 17 shows the microfluidic chip with each resistance in a different color. Figure 17 also illustrates the different divisions of the chip. The concentration divider consists of the two input currents and the six branches (the ones carrying the MBs, $R_{1\text{-}3}$, and the ones carrying the dilutant, $R_{4\text{-}6}$). The mixer and the testing sections were then coupled and the four branches that correspond to the two sections are $R_{7\text{-}10}$.

To simplify the experiential process, the initial inputs into the system must have the same current. This physically translates to having the same size syringe with a pump capable of injecting liquid simultaneously. A dual pump with the same size syringe is perfectly suited for this experiment. Leading to:

$$I_1 = I_2 \tag{3.1}$$

I_1 being the input carrying the microbubbles at a concentration of c_1 and I_2 carrying the dilutant with a microbubble concertation of zero.

All four testing channels need to have the same geometry and flow rate to ensure homogeneity between channels. This leads to the following equations.

$$R_7 = R_8 = R_9 = R_{10} \tag{3.2}$$

Notice that since the mixer and the testing section are combined in one channel, the resistance of the mixer must be equal across all branches, even if they are not mixing anything.

To decrease bubble trapping and 3D flow, the height of all the concentration dividers (and the mixer) will remain the same. Lastly, and most importantly, the cross-sectional area of each of the merging branches was used to dilute the initial MB concentration. Since we fixed the height of the system, the width of the branches was dictated by the concentration desired. For example, for one channel's concentration to be half its initial MB concentration, there would be two merging branches with equal width and height. One branch contains the initial MB concentration and the second would be carrying the dilutant with no MBs in it. In total there are 3 concentrations of microbubbles, the input concentration, c_1, and the two diluted concentrations c_2 and c_3. This leads to the following equations:

$$i_2 = \frac{c_2}{c_1} i_0 \tag{3.3}$$

$$i_3 = \frac{c_3}{c_1} i_0 \tag{3.4}$$

Adding the currents at nodes 1 and 2 yields:

$$i_4 = (1 - \frac{c_2}{c_1}) i_0 \tag{3.5}$$

$$i_5 = (1 - \frac{c_3}{c_1}) i_0 \tag{3.6}$$

Summing the voltage drops due to currents and resistances lead to the next equations:

$$i_0 R_1 + i_0 R_7 - i_0 R_8 - i_2 R_2 = 0$$

$$i_0 R_1 + i_0 R_7 - i_0 R_9 - i_3 R_3 = 0$$

$$i_0 R_6 + i_0 R_{10} - i_0 R_9 - i_5 R_5 = 0$$

$$i_0 R_6 + i_0 R_{10} - i_0 R_8 - i_4 R_4 = 0 \tag{3.7}$$

Inputting equations 3.1, 3.3, 3.4, 3.5, 3.6 they simplify to the followings and solving R_2 and R_3 in terms of R_1 and R_4 and R_5 in terms of R_6 :

$$R_2 = \frac{c_1}{c_2} R_1 \tag{3.8}$$

$$R_3 = \frac{c_1}{c_3} R_1 \tag{3.9}$$

$$R_4 = \frac{1}{(1 - \frac{c_2}{c_1})} R_6 \tag{3.10}$$

$$R_5 = \frac{1}{(1 - \frac{c_3}{c_1})} R_6 \tag{3.11}$$

Note that solving nodes 3 and 4 yields:

$$I_1 = \ i_0 \, (1 + \frac{c_2}{c_1} + \frac{c_3}{c_1})$$

$$I_2 = i_0 \left(1 + \left(1 - \frac{c_2}{c_1}\right) + \left(1 - \frac{c_3}{c_1}\right)\right) = (3 - \frac{c_2}{c_1} - \frac{c_3}{c_1})$$

For the given resistors on equation 3.2:

$$\frac{c_2}{c_1} + \frac{c_3}{c_1} = 1$$

The final version of the design had the two dilutions of the MBs to be:

$$c_2 = 0.7c_1$$

$$c_3 = 0.3c_1$$

And further note that:

$$I_1 = 2\, i_0$$

With all the geometric constraints and the resistance equations given in the formulas, all that is left is to translate the electric circuit analog to the physical characteristics of the chip. The resistances of the microfluidic structures are dependent on multiple variables: the viscosity of the fluid (constant throughout the experiment), the height, the length, and the width of the channel. The formula that links these properties to the hydraulic resistance is the following [91]:

$$R_{hyd} = \frac{12\eta L}{\left(1 - .63\frac{h}{w}\right) h^3 w}, \quad h < w \tag{3.12}$$

Where *h* is the high of the channel, *w* is the width, *L* is the length and *η* is the viscosity of the liquid flowing through the channel.

Given that the height is constant, and the width is dictated by the desired concentrations, the only variable left to solve for is the length of the branch. This variable was set by the resistance equations that stem from the electric circuit diagram. A second thing to notice is that since the initial current inputs must be the same, the concentration divisions we can achieve have to be complementary. For the two diluted channels, only concentrations that add up to 100% can be achieved. Thirdly, notice that the branches for the inputs are dependent on R_1 for the MBs and

on R_6 for the dilutant. So, by fixing one branch for each input, the other two can be fixed as well. This was dependent on how the chip would fit on the printable rectangle.

All of these formulas were written into an Excel table. A "goal seek, what if analysis" was done to solve for the length of each branch given the width, height, and resistance of each channel.

3.1.4 **Micromixer**

Given the fact that the flow is very laminar at these scales, Re<<1 mixing takes a long time. Since Pe>>1 across all sections, the convection has a greater effect on the flow over diffusion. This makes the time of diffusion across the width of the channel a lot longer than the time it takes to flow over the length of the channel, explaining the need for a micromixer. A modified version of the tesla mixer was used to fit into the constraints of the chosen widths. The number of tesla units was chosen to fit the maximum amount possible on the lowest branch. As mentioned before, the same amount of tesla units was included on all of the branches to make the resistances equal. A total of nine tesla mixer units per channel were used in the micromixer.

3.1.5 **Modeling**

All the geometric constraints were drawn into the Solidworks model. Here are the major constraints that had to be considered when modeling:

1. Distance between the outer walls and any component had to be greater the 50μm
2. Distances between parallel walls had to be greater than 50 μm
3. All components had to fit within the 35mm by 55mm print bed area
4. All heights had to be a multiple of 50 μm

Three different branch lengths were modified manually to ensure that all requirements were met. These lengths were the length of R_1, the length of R_6, and the lengths of $R_{7\text{-}10}$.

Inside Solidworks, the widths and the height of the channels were inputted. The shape of the channels was dictated by the modeling equations. For the concentration divider, the two unknown variables were the lengths of R_1 and R_6. These were modified and chosen arbitrarily to

make the shape fit into the printed dimensions. Lengths of $R_{7\text{-}10}$ were set using the "Path Length" tool in Solidworks. The mold's outer walls included a 7-degree chamfer to help with demolding.

3.1.6 **Final Design**

The final design has a total of two input ports and one output port. Table 1 shows the lengths widths and heights of all the sections outlined in Figure 18.

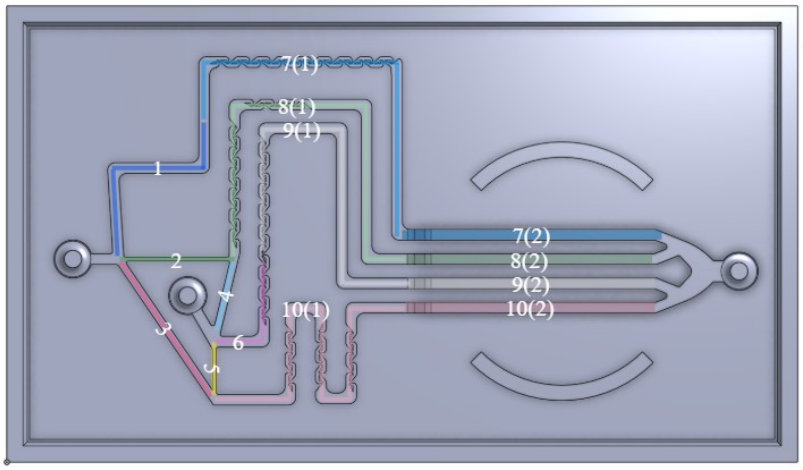

Figure 18 The final design of the microfluidic chip.

	Segment	Height mm	Width mm	Length mm	Reynolds	Peclet	Flow µL/min
	1	0.15	0.70	12.00	0.014	1.55E+06	50
	2	0.15	0.49	11.20	0.015	8.14E+05	35
	3	0.15	0.21	7.63	0.022	2.19E+05	15
	4	0.15	0.21	3.82	0.045	4.39E+05	15
	5	0.15	0.49	5.60	0.030	1.63E+06	35
	6	0.15	0.70	6.00	0.028	3.10E+06	50
7,8,9,10	Section 1	0.15	0.70	31.50	0.036	1.82E+05	50
	Section 2	0.70	0.70	16.50	0.008	8.50E+05	50

Table 1 The length width and height of each of the size branches of the concertation divider. Colored in dark green are the two arbitrary lengths and widths that make the system fit into the printable bed rectangle. At an input current of 200 µL/min.

3.1.7 **Validation**

3.1.7.1 Concentration Distribution

Two main results needed to be validated, the MB concentration of each channel and the distribution of the MBs inside each channel. Since bubbles are small, a 4x magnification will not have enough resolution to image them. However, there is still an advantage to viewing the entire channel of the chip. For this, food coloring and water were used as MBs and dilutant substitutes. To calibrate for the signal absorbed by the food coloring a serial dilution of 1x, 1/2x, 1/4x, and 1/8x and another one of 2/3x and 4/9x were prepared. Each of these was injected into the chip in reverse (from the output port) and four images were taken of each concentration to build a calibration curve. A syringe pump was then used to flow the food coloring and the clear water into the chip. Three different input flow rates, I_1, were tested [25, 50, 100] µL/min matching the total input flow rates of [50, 100, 200] µL/min. At the testing section, multiple images were taken at each channel. Each image was then analyzed in ImageJ. A line 500 pixels wide was manually drawn perpendicular to the flow of the channel. The average concentration at each point in the line was then plotted. The average concentration was taken, and the distribution of the signal was characterized using the following equation:

$$\% \, Mixed = 1 - \frac{Standard \; deviation \; of \; signal}{Mean \; signal} \tag{3.13}$$

3.1.7.2 Imaging Microbubbles

Bubbles were imaged in the microfluidic chip using an inverted brightfield microscope, the Widefield Olympus IX71 fluorescent microscope with no filter cube at 10x. A video of 30 frames at 100 ms framerate was taken for each of the 4 channels. The measurements were taken twice in different locations of the channel. Videos were saved as Tiff stacks and imported into ImageJ and MATLAB for analysis. The TrackMate v3.8.0 plugin was used to find and track the bubbles and quantify bubble speed [122]. A LoG detector was used to find the blobs with sub-pixel localization. An automatic quality thresholding and a “simple LAP tracker” were used to find the links of the bubble tracks. Track statistics, containing the average speed of each track, were saved and processed. To count and analyze their size, the tiff stacks were imported into MATLAB where a

circular Hough transform was used to find the bubbles. Channels were compared to ensure that all have the same flow rate, the same bubble size, and the only difference is the bubble concentration.

3.1.7.3 US Pressure Attenuation

Three different PDMS slabs with a thickness of 2.5mm (the distance between the roof of the channels and the top of the chip) were created from three different PDMS mixtures on three different days. Three different pressures of [200 300 and 500 kPa] were tested. The US probe and a hydrophone were both set up inside a water bath. They were aligned using a three-axis motorized positioning system. One measurement consists of ten pulses, ten cycles in length, and the maximum voltage amplitude for each pulse was averaged over the ten pulses. Three measurements were done with no PDMS to calibrate for the different pressures and then three measurements were done for different slabs. For each slab, three different random locations were tested. A two-way Anova was used to test if a significant difference existed between slabs and within slab variability. Figure 19 shows the setup for this experiment.

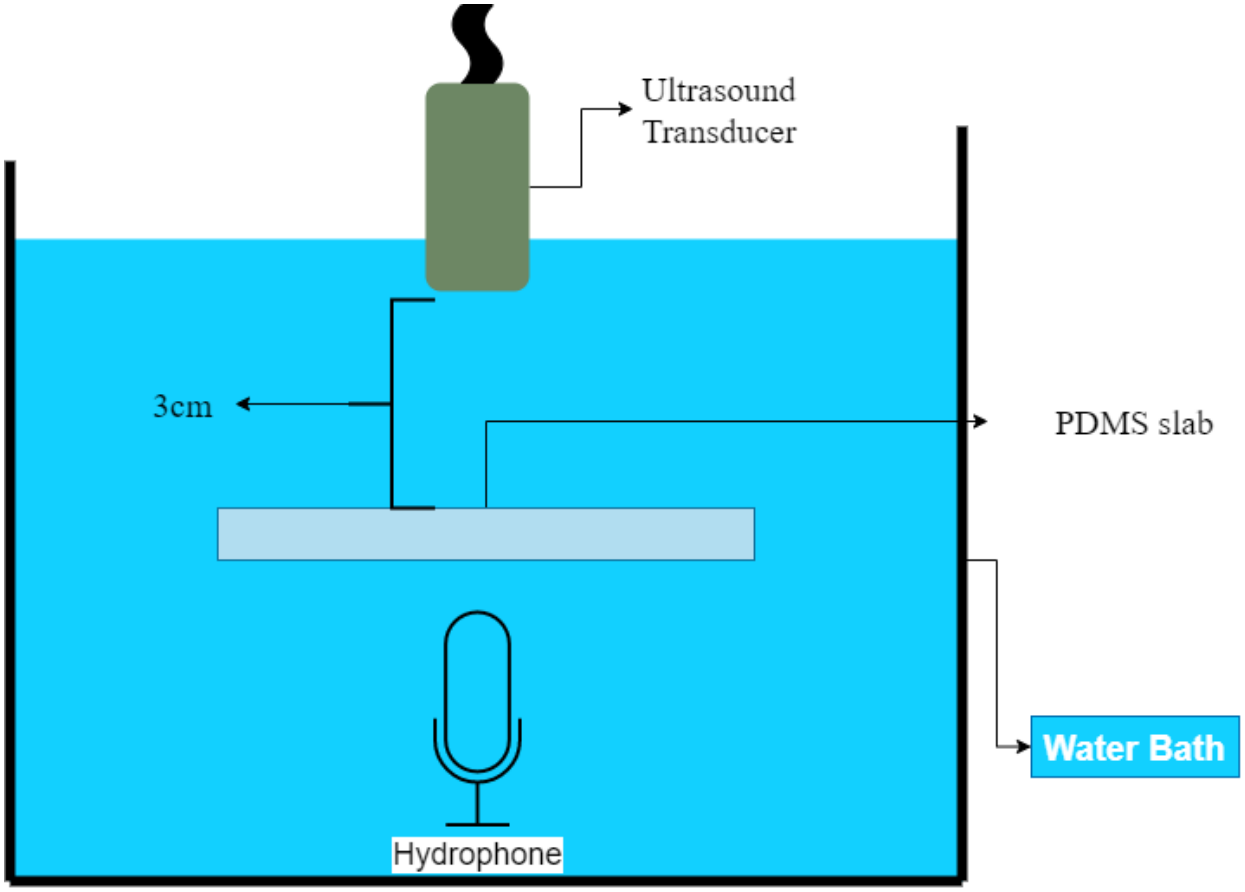

Figure 19 Setup to measure the attenuation of the PDMS slab.

3.1.8 **Manufacturing**

Manufacturing the mold entailed sending the STL file into the Asiga soft-lithography printer and using the GSC clear resin. Slicer and UV exposure setting are listed below:

- Baseplate thickness: 0.250mm
- Baseplate type: shadow
- Baseplate placement: underneath
- Light intensity: 28.318
- Slice thickness: 0.05mm
- Exposure time: 1.6s
- Burn-In exposure time: 6 s
- Burn-In layers: 5

Once the part finished printing the following post-processing steps were performed:

1) Remove the part from the metal plate using a razor
2) Clean the part with isopropanol for 3 min

3) Put the part in isopropanol and sonicate for 5 min
4) Remove the part and dry using Nitrogen gas
5) Place the part under UV light for 10 minutes to finish curing
6) Place the mold in 70% ethanol and sonicate for 5 min
7) Before pouring PDMS clean the part with nitrogen gas

Once the mold is ready, mix in a 10:1 ratio the PDMS and its solidifier. Mix well and put under vacuum for 10-15 min to get rid of all the bubbles. If there are still bubbles are at the surface, and open and close the vacuum. Once the bubbles are gone, pour the PDMS mix into the mold. Expose them to the vacuum again to get rid of the bubbles formed during pouring. Then, put into the oven at 70 degrees Celsius for 2 hours. Also, pour 40g of PDMS into a petri dish to use as a flat surface for the other half of the chip. Once cured, remove from the oven and demold using a sharp edge and some tweezers, being careful not to ruin the mold and not to cut into the channels. Cut the matching half from the PDMS poured into the petri dish. Clean each of the surfaces from any dust or extra PDMS bits using clear tape and Nitrogen gas if needed. Put both of the edges that are meant to be glued together under plasma at a distance of 3 cm for 30 seconds. Remove from plasma and push together with enough force until the parts are welded strong enough to form one piece. Before seeding any cells send to sterilize in an autoclave.

3.2 Cell Viability and ATP Release After Ultrasound and MB Therapy

The Microfluidic chip was designed with two inputs and one output port for flow. However, chemicals (like Calcein and PI), reagents (Luciferin and Luciferase), and cells were all inserted into the chip via the output port. This made it easy to inject reagents and seed cells in all channels at an equal concentration. All pipetting for static tests was done through the output port.

3.2.1 Cell Seeding

Before cell seeding, the channels need to be coated with fibronectin at a concentration of 100 µg/ml. This helps the cells attach to the surface of the channel. To do this, wash and rinse the inside of the chips with 70% ethanol three times. When washing with ethanol, insert the liquid into the chip and then use a glass pipette and the vacuum to clear all the ethanol out of the chip and repeat. Next, wash with PBS three times; when washing with PBS do not use the vacuum to suck out the liquid from the inside. Instead, just add more PBS into the channels and let the old

liquid run out the other side. This prevents air bubbles from getting trapped in the system. Then the channel is ready for coating. Dilute the fibronectin by the correct amount (final concentration of 100 µg/mL) in PBS and similarly add it to the chip without emptying the channels. Let this rest at room temperature for one hour. Before seeding the cells, wash the channels three times with warm media without removing liquid to avoid air bubble entrapment.

Trypsinize the cell lines that are in the 25 cm^2 flasks. From here, spin down and resuspend in media with the volume needed. The resuspension volume was obtained by matching the areas of the flasks to the area of the microfluidic chip so that the cell density inside the confluent flask would be the same as the cell density in the microfluidic chip. Resuspension volume is given by the following formula.

$$V_{resuspention} = \frac{Area_{flask}}{Area_{chip}} Volume_{chip}$$

For a T25 area and a surface area inside the chip of 153 mm^2 and a volume of a chip of 55µL, the resuspension volume is 899 µL. A useful dependant factor to the volume resuspension is cell concentration. This was calculated using the following equation:

$$Cell\ Concentration = \frac{\#\ of\ cells\ in\ a\ T25\ flask}{V_{resuspention}}$$

A confluent monolayer of 4T1 cells in a T25 flask contains 1.5e6 cells, giving the final concentrations of 1.74e6 cells/ml. A confluent monolayer of HUVEC cells contains 1.25e5 cells, giving a final resuspension cell concentration of 1.45e5 c/mL.

While the cells are being spun down, add 1.5 mL of sacrificial media into the petri dish.

Reconstitute the cells at the desired concentration and homogenously mix inside the test tube by pipetting up and down. Insert the cells into the channel and as fast as possible flip the chip into the puddle of sacrificial media. Ensure that all ports have access to the media. Let the cells fall down to the “roof” of the chip, close the petri dish, and put inside the incubator at 5% CO_2 and 37 degrees Celsius overnight. The next day checks for a confluent monolayer of cells before experimenting.

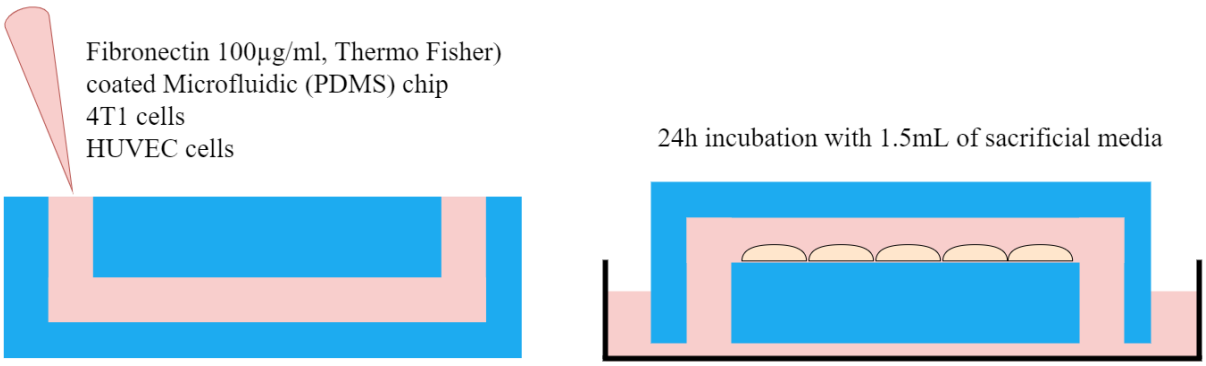

Figure 20 Process for seeding and cultivating cells on the roof of the microfluidic chip.

3.2.2 **Cell Viability Assays**

3.2.3 **Static Bubbles Experimental Setup**

To assess cell viability after US exposure, a Calcein AM and PI assay was used. For static tests, a MB media solution was prepared beforehand at a concentration of $1x10^7$ MB/mL. The US setup was also prepared before any test as shown in Figure 21. A pig gelatin phantom was used as both a matching layer and a guide for the US probe to always be 3cm apart from the testing zone. The US probe (flat 1MHz transducer A303S, 0.5 inch, Olympus) was connected to an RF amplifier (AR, model 75A250, Souderton, PA, USA) which in turn was connected to a waveform generator (33210A, Keysight Technologies, Santa Rosa, CA). Experiments were performed using the busts of the following pressures and cycles

Waveform generator (mVpp)	Corresponding Pressure (kPa)	Number of cycles
250	500	1000
150	300	1000
100	200	1000
150	300	100
150	300	10

Table 2 Pressures and number of cycles used as bursts in the MB and US therapeutic pulse.

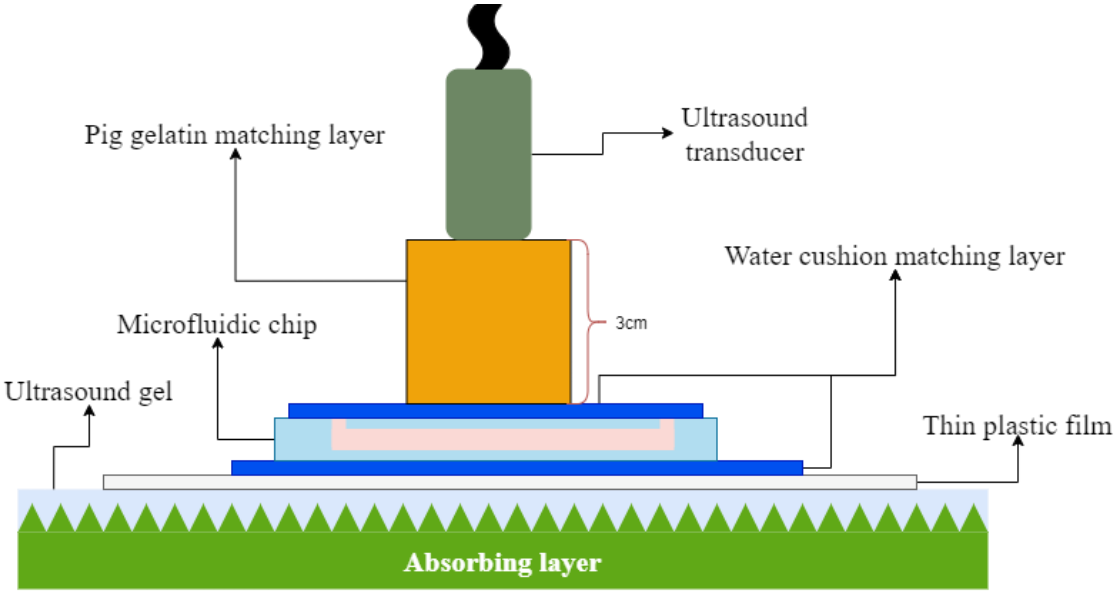

Figure 21 The Ultrasound setup for exposing the cells inside the microfluidic chip to US and MB therapy.

The microfluidic chips are turned "roof-side-up" so that the cells are now on the roof of the chip and the ports become accessible. The MB and media solution were injected into the chip using the output port and rested for five minutes in order to let the bubbles float to the top and come into contact with the cells. The cells were then exposed to the US pulse allowing the microbubbles and cells to interact (Figure 22).

After US therapy, the cells rested for 10 min. While the cells were resting the Calcein AM solution was diluted in PBS to the desired concentration of 4 μg/mL. After the 10 minutes passed the Calcein AM was inserted via the output port into the channels and incubated for 30 min. While the cells were resting in the Calcein AM solution, the PI solution was also created by diluting the stock PI in PBS to the concentration of 25 μg/mL. After 30 min the cells were taken out of the incubator. The PI was inserted into the channels and after 5 min the chip was ready for imaging (Figure 22).

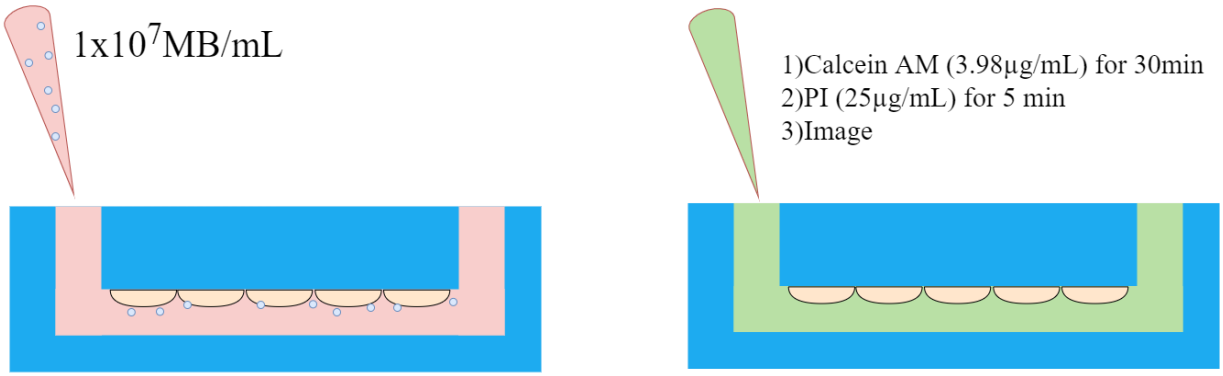

Figure 22 Left- Inputting MBs into the chip with cells cultured on the roof so that the two can interact. Right- After US exposure the cells are allowed to rest for 10 min before Calcein AM is added to stain cells that are still alive. After 30 minutes of incubation with Calcein AM, the cells are exposed to a PI solution to stain dead cells.

3.2.4 **Setup for Flowing MB Experiments**

For flow cell viability assays a similar setup was used. Instead of injecting the MB (final concentration of 1x 10^7 MB/mL) and media solution into the chip, it was prepared and put into a 1mL syringe. Another syringe was prepared with the same volume but without MBs, serving as the MB dilutant. After removing large air bubbles that come from filling the two syringes, they were placed on the pump. The flow rate was set to 100 µL/min (a total flow rate of 200 µL/min replacing the media inside the chip every 10 seconds). Similar to the static tests, the chip was taken out of the incubator, flipped and the US setup was prepared. The two syringes on the pump were placed into the entry ports, inserting the one without MBs first to ensure that no MB went into the media channel. Then the MB entry was inserted and allow flow for 2 min to stabilize. Once the two minutes passed the US pulse was sent. For multiple pulses, each pulse was sent 2 min apart. The two syringes were disconnected, the pump turned off and the chip went through similar steps to add the Calcein AM and PI assay.

3.2.5 **Imaging and Image Processing**

This section describes the standardized protocols for image acquisition and custom algorithms for image processing. For Calcein AM and PI images, the following steps were taken when imaging the chip in the Widefield Olympus IX71 fluorescent microscope. Calcein AM fluorescent signal was acquired using a FITC filter cube (Ex/Em: 470/525nm) with an exposure of 300ms. Rapidly

and without moving the chip's position or focus, the fluorescent channel was changed to the Cy5 channel (Ex/Em: 562/624 nm) to image the PI signal with the same 300ms exposure. Both images were taken with a monochrome 8-bit camera (Evolution VF cooled monochrome camera) and all colors added in the images are artificial. The chip was moved to a new location and the process was repeated until 5-10 images were taken per channel. Each chip contained four channels, and each was imaged separately. All images were saved separately into a folder. Methodically taking images takes advantage of the ordered image and pairs them by nature. This way an algorithm can join pairs and analyze images in batches (Figure 23). Taking multiple images at different locations in the same condition reduced selection bias and gives a better understanding of the stochastic nature of MB sonoporation. This gives us more confidence in the mean effect of the US therapy.

As mentioned before once the images were separated into their groups, an algorithm analyzed the Calcein AM and PI signals of all image pairs. Depending on the cell line a different algorithm was used. Since 4T1 cells are small and highly confluent with overlapping cells, clear borders between cells are hard to define. Therefore, for 4T1 experiments, a rougher and more robust method was used using simple area fractions as explained below. However, HUVEC cells tended to avoid touching each other, are bigger and more defined. We can use this to our advantage and use image processing tools like the watershed transform to segment the images into individual cells and actually count how many dead to live cells were in an image. More details on the algorithm will be explained below and a graphical workflow chat can be seen in Figure 24.

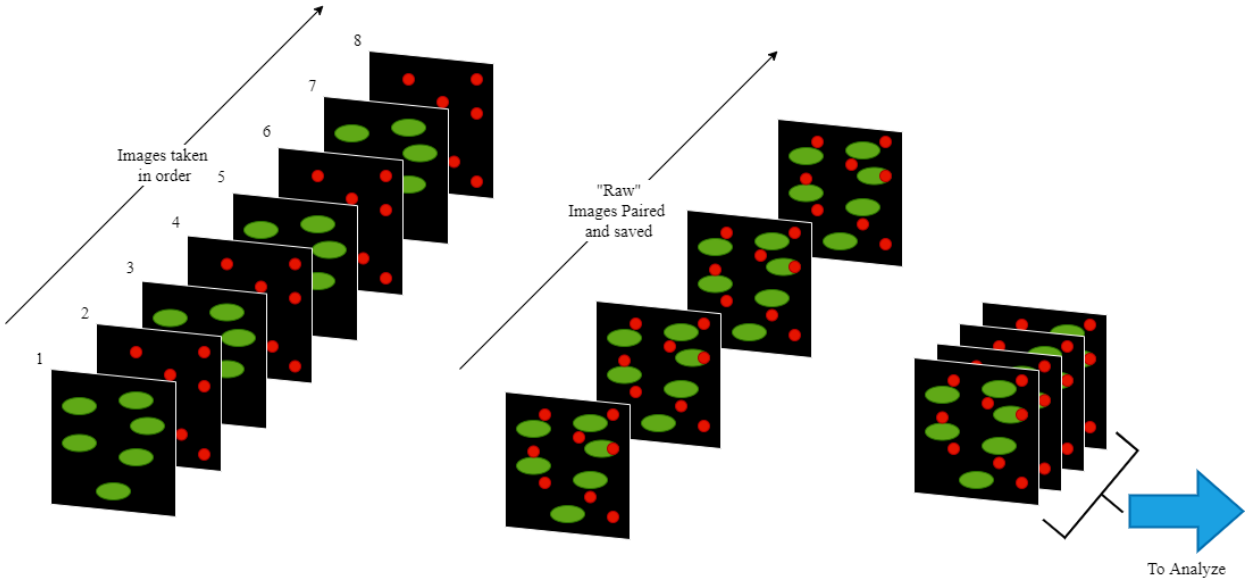

Figure 23 Example of how images are taken in order at the microscope. The ordered images were converted into image stacks and then grouped together to be automatically analyzed by an algorithm.

For both custom algorithms written in house, the first step was to generate an automatic threshold for each channel. This automatic threshold was obtained using Otsu's method. In brief, this method divides the image into two classes using all possible values as a threshold. For each threshold value, the method calculates a weighted variance of both classes. The value chosen as the optimal threshold is the value that minimizes that weighed variance. Once the threshold was selected, two different algorithms were used depending on the cell line, just like described above. A simple algorithm was used for 4T1 where the area over the threshold was kept for each image. The estimation for cell death came from the area of the PI signal over the sum of the Calcein and the PI areas with an intermediate multiplication of the cell to nucleus ratio. The HUVEC algorithm similarly took the thresholded image and applied a watershed transform to the areas inside the image over the threshold values. The transform uses the regional maximums as the centers for the watershed operation. The algorithm then uses the separated image and counts the number of regions calculated by the watershed segmentation. The number of regions in the PI images was considered as the number of dead cells and the regions in the Calcein image were assigned to be

the number of alive cells in the image. The percentage of dead cells in these images is simply the number of dead cells over the total number of cells in each image.

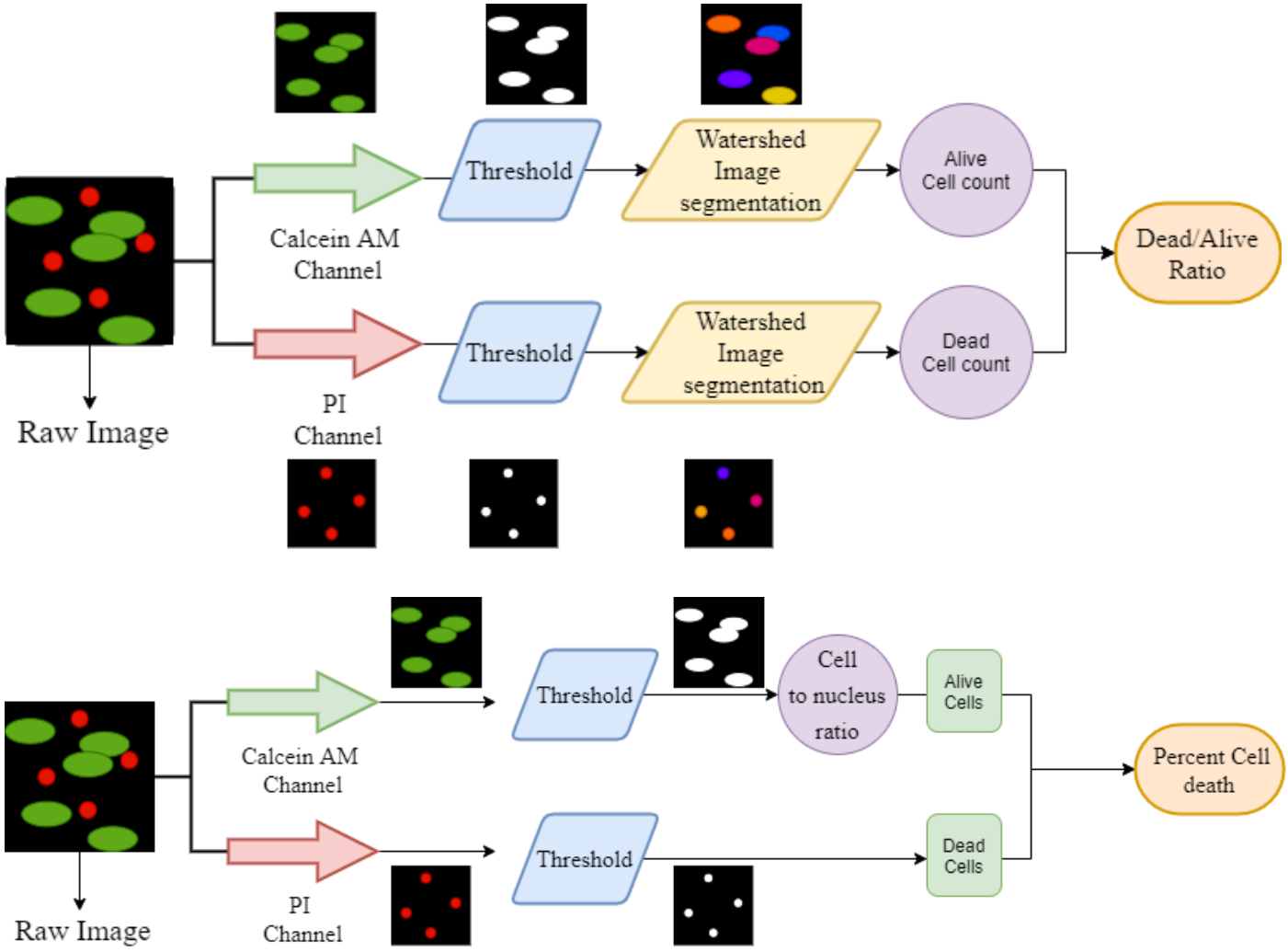

Figure 24 Graphical representations of how the algorithm segments and obtains a quantitative measure of cell death. Top- How the algorithm functions with HUVEC cells. Bottom- How the algorithm calculates cell death using areas.

3.2.6 **Cell to Nucleus Ratio**

PI only stains in the nucleus of the cell, while Calcein stains the entire cytoplasm. This makes the red signal of a dead cell occupy less space than a signal of a live cell. To compensate for this ratio of cytoplasm to the nucleus, cells were seeded in the microfluidic chip overnight. Calcein and Hoechst were used to stain the cytoplasm and the nucleus. The same algorithm was used to

segment the image and calculate the ratio of the areas. Ten images were taken, and the ratio of each image was averaged (Figure 25).

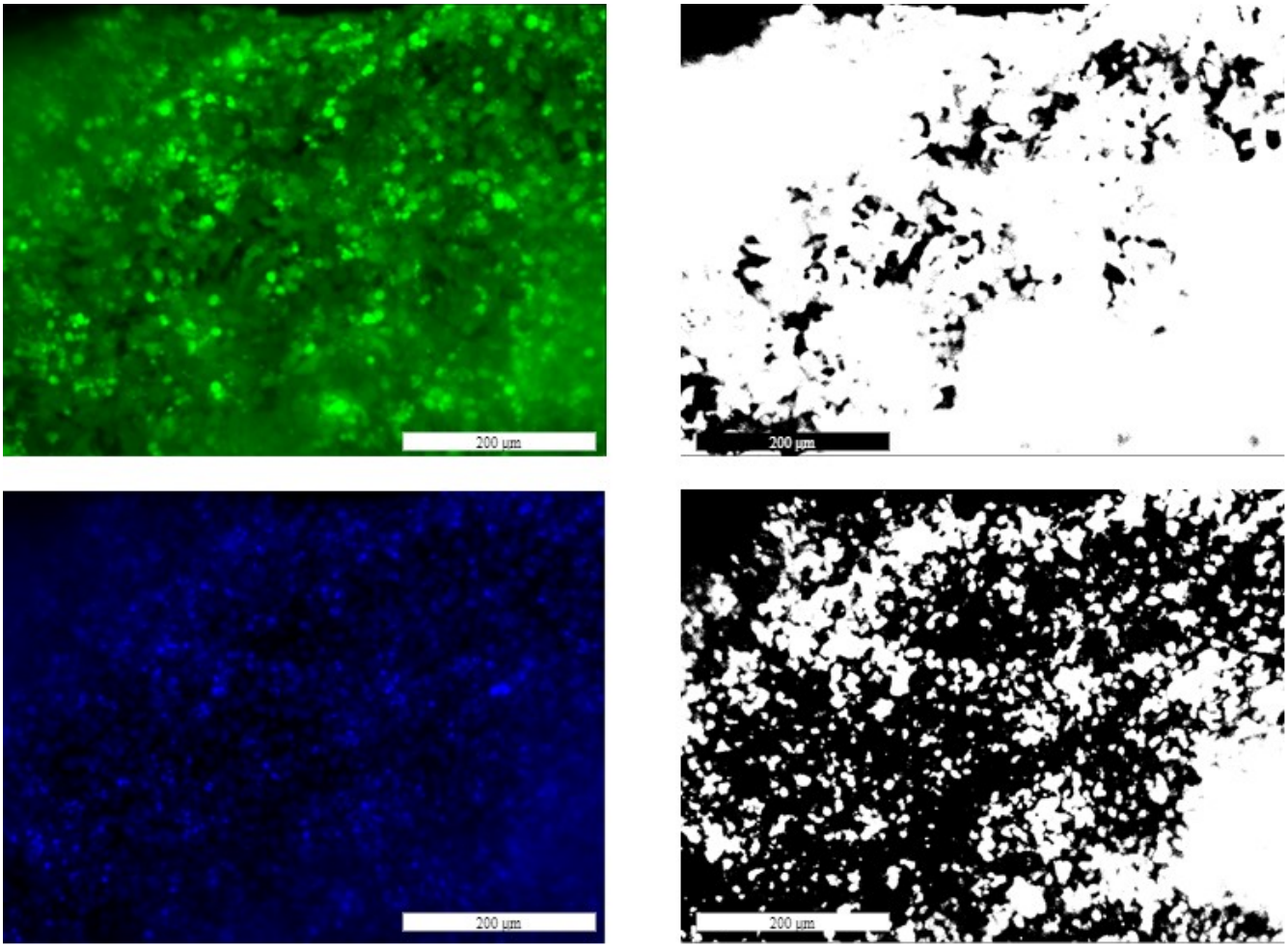

Figure 25 An example image of 4T1 cells, where green marks a cell's cytoplasm and blue marks their respective nucleus. To the right is the thresholded image. The areas of each were taken to obtain the cytoplasm to nucleolus ratio.

3.3 **ATP Release Assays**

3.3.1 **Experimental Setup**

ATP experiments followed the same initial cell seeding process as the cell viability assays. However, the main difference between the viability assays and the ATP imaging is that the latter was done using live imaging of the effect of sonoporation. This was achieved by using an EMCCD Evolve 512 camera with a 0.3x magnitude lens and placing the camera below the chip. The US

probe was positioned in place from above using the same phantom for the matching layer. Imaging live enables the triggering of the ultrasound at a certain moment in time to see the immediate effect of the US pulse. For every experiment, the following methods were followed. First, the luciferin luciferase solution containing the MB (final concentration of $1x10^7$ MB/mL) was inserted into the chip. More details on the preparation of the luciferin luciferase assay are described in Tan et al.[85] Then the chip and US were aligned using the camera's brightfield option. Once they were in place, a brightfield image was taken as a reference to know where the US probe was located. A sample alignment can be seen in Figure 26. Then the setup was covered by a custom cardboard shroud and the lights in the room were turned off. The total time of the video taken was five minutes. Each image has a one-second integration time and a one-second "dumping" time. That means each frame is spaced two seconds apart. The camera has a resolution of 16-bits. Once the setup was dark and the US clamped in place inside, the camera started recording, after 10 seconds the US was activated. After the pulse, the camera kept going for the remainder of the 5min. A .zvi stack was created and exported with the original 16-bit memory.

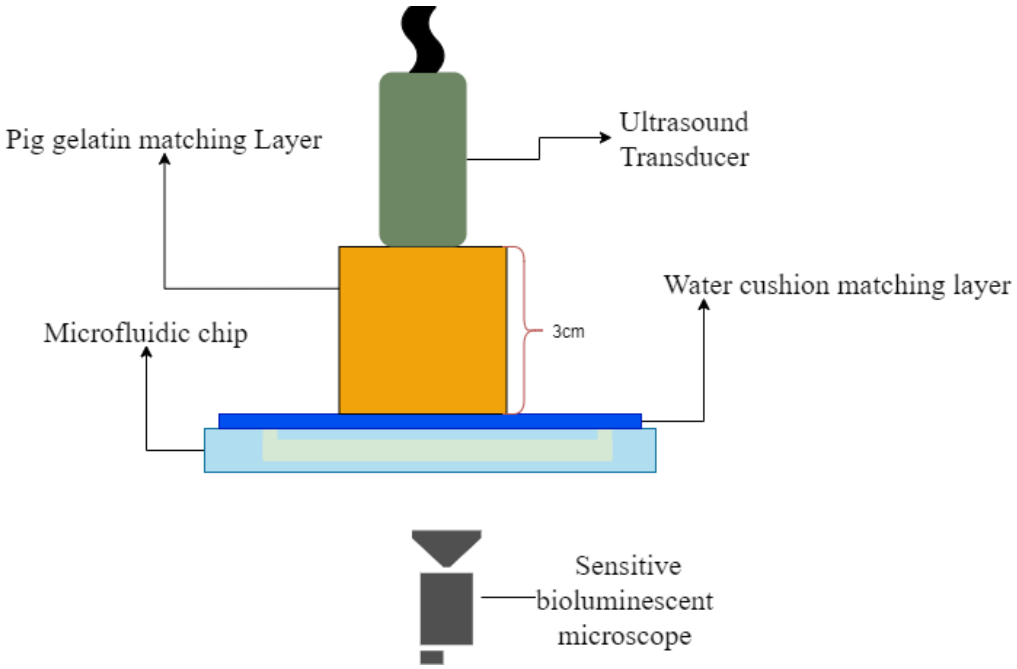

Figure 26 The experimental setup of ATP live imaging. The chip has Luciferin luciferase and MB solution.

3.3.2 **Image processing**

All .zvi files were converted to a .tiff stack with 150 frames. Each tiff stack was then imported into a custom MATLAB GUI. Using the brightfield image, four rectangular sections of 100 x 10 pixels in size were fitted to the image where the US probe and the four parallel channels were located. These four rectangles were saved as ROIs. The conversion between signal intensity and ATP amount is described in better detail in Tan et al. [85]. Briefly, background noise was first removed from the image stacks. For each ROI the signal is then integrated, and a calibration factor is applied to convert the signal to an amount of ATP.

Four measures of ATP kinetics were taken, the total amount of ATP release, the speed of release, the time between ultrasound activation and peak signal, and the time constant of ATP consumption after release. The signal was first smoothened using a sliding window of three frames. The frame in the stack where the US pulse was sent was located manually. Total ATP release was calculated as the peak intensity of the signal minus the average intensity before the ultrasound pulse. ATP release speed was calculated as the slope of the linear fit of the signal between the US exposure and the peak ATP signal. The time between US activation and peak ("time to peak") signal was taken as well. Finally, the ATP time constant was an exponential fit of the signal from the peak intensity to the end of the video. The time constant is a physical interpretation of the reactions of the luciferin luciferase assay with ATP. A sample video with each ROI can be seen in Figure 27. Each ROI was saved with all three outputs with the corresponding pressure and cycle count to be grouped later.

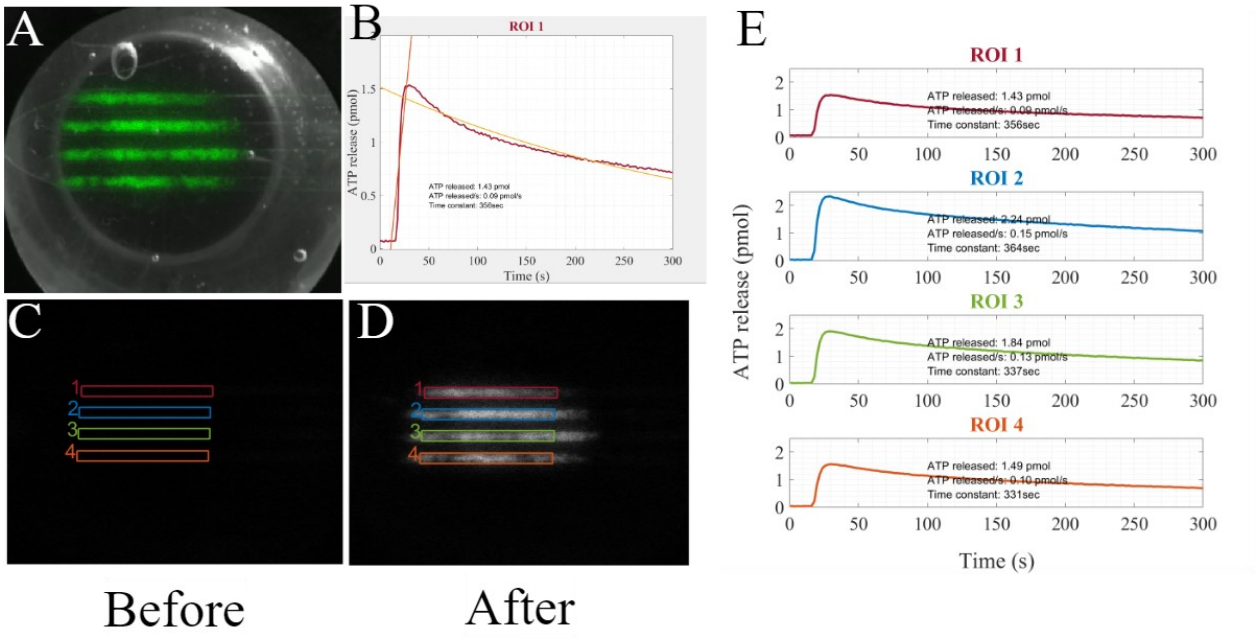

Figure 27 A) The overlay of the peak signal colored in green and the brightfield image of the US probe. B) Shows an example of ROI processing with the signal colored in red, the linear fit for ATP released colored in orange, and the exponential fit colored in yellow. C) An image collected by the camera before the US pulse was sent with the 4 ROIs analyzed. D) An image of the same 4 ROIs but after the US pulse was sent. E) The graphs of the 4 ROI's analyzed in the tiff stack with their respective outputs of ATP released, ATP release speed, and ATP time constant

3.4 **Statistical analysis**

A one-way Anova was used to characterize the significance of pressure and cycles on all ATP kinematics and cell death. Multiple comparisons were made with a Tukey test. All tests were performed with MATLAB r2019.

Chapter 4 Results

4.1.1 **Microfluidic Chip Pressure Attenuation**

To ensure that the manufactured PDMS did not significantly attenuate the pressure of the US wave, we measured three slabs made separately. Pressure attenuation was measured with respect to a control. It is defined as the ratio between the maximum amplitude of the measured signal vs the control signal (Figure 28). Their thickness of 2.5mm was chosen as it's the distance between the top of the PDMS and the roof of the channels where the cells attach. The average ratio of maximum pressures is .9424 between the control and the slab (Figure 29). There was no significant difference between the pressures and there was no significant difference in attenuation depending on location.

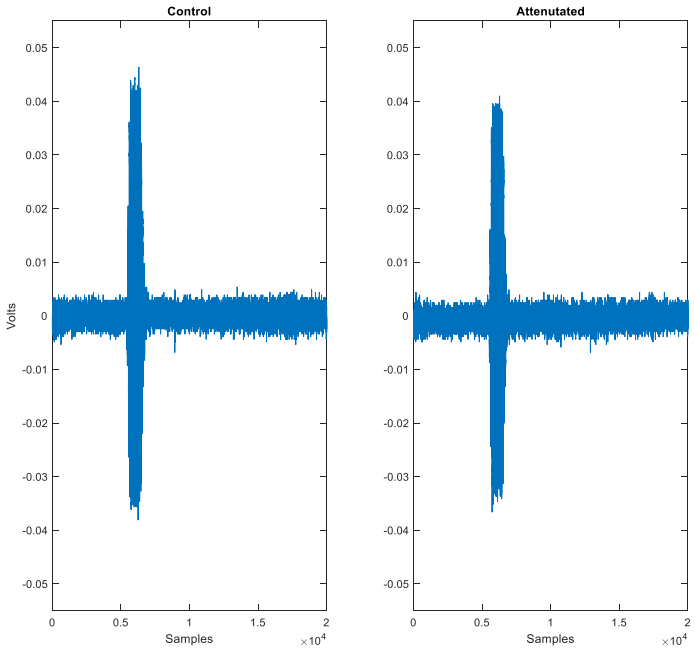

Figure 28 An example of a control pulse signal vs an attenuated pulse signal.

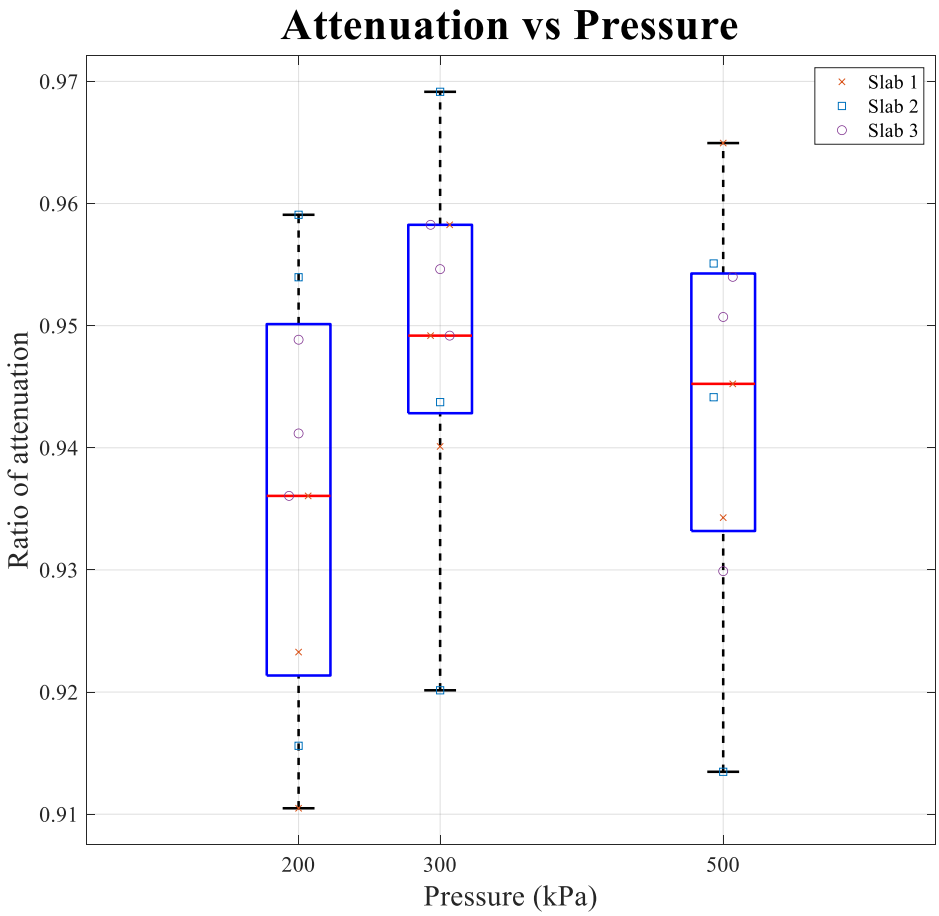

Figure 29 The ratio of attenuation of the three slabs at different US pressures repeated at different locations.

4.1.2 **Microfluidic Chip Concentration Validation**

To validate the chip's spatial distribution, food coloring was used as a visual marker. We used this test to obtain a quantitative understating of the efficacy of the chip's concentration splitting and subsequent mixing of inputs and dilutants.

4.1.2.1 Static Food Coloring

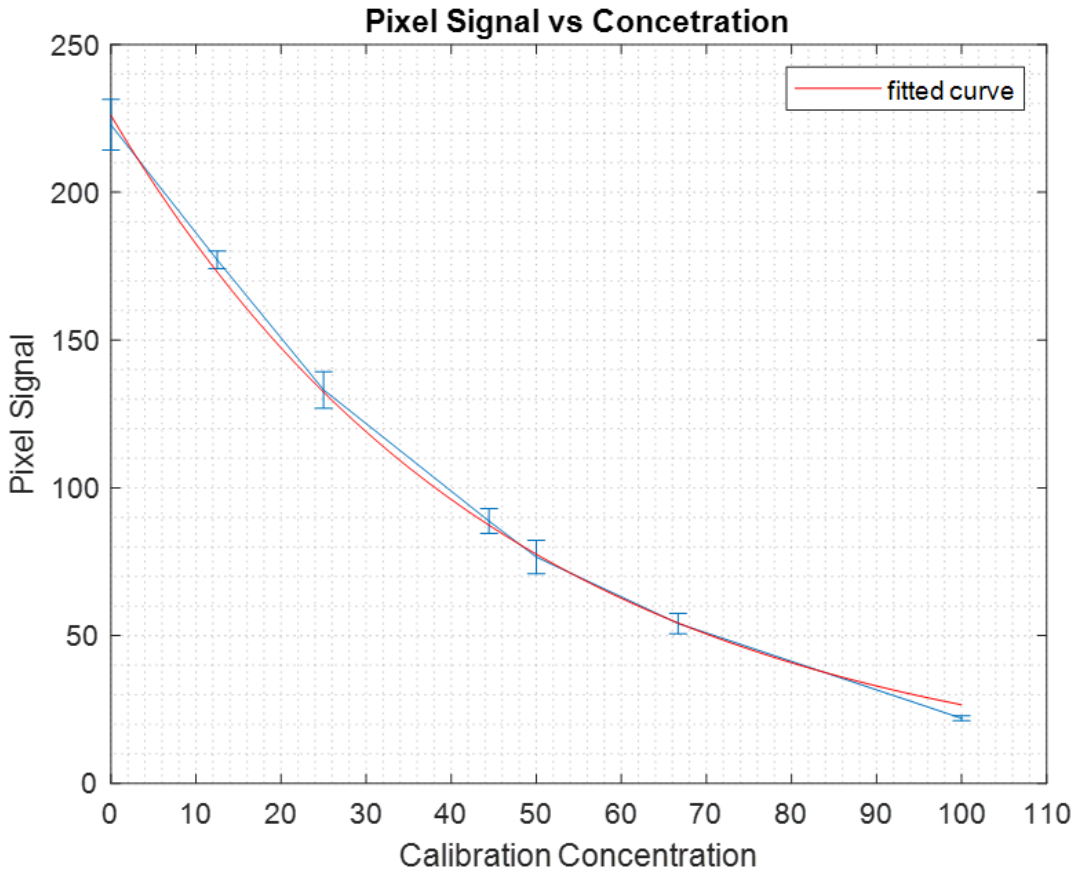

Figure 30 Pixel value plotted against the average concentration of static food coloring inside the chip. Error bars are the standard deviation of the average pixel values of the images. (R^2=.99, F=statistic p-value<<.001)

The static images where the values were taken from are seen in the purple rectangle of Figure 31. There, it is shown how lighter colors (higher pixel values) match the lower concentration of the food dye. The matching pixel values and concentrations are seen in Figure 30. The exponential fit found the following equation linking the food dye concentration to the Pixel Signal. The trend follows an exponential curve as the absorbance of the dye is being measured.

$$Pixel\ Value = 226 \cdot e^{-0.0214 \cdot Concentration} \quad (4.1)$$

4.1.2.2 Flowing Food Coloring

The same process was used to evaluate the concentration in flowing channels. When flowing, the four different concentrations can be seen, as exemplified in the blue rectangle of Figure 31. The figure also shows the width and the length of the lines used to evaluate the average pixel value.

Once flowing, more images were taken to visually evaluate the functionality of the chip. The entrance flows and the early stages of the mixers can be seen in Figure 32. Notice the laminar flows not mixing in the entrance of both the 70% channel (bottom) and the 30% channel (middle). The telsa mixer works by splitting flow and creating turbulent sections after the half-circle. Figure 32 shows (in the yellow and dark purple squares) how early streaks of white are being mixed into the dark food coloring. Figure 33 shows the analysis of the different flows tested. We showed a close relationship between the flowing food dye and the static concertation curve. We tested three different flow rates to quantify the mixing in each channel and obtained an 85% mixing efficiency over all tested conditions in all the channels.

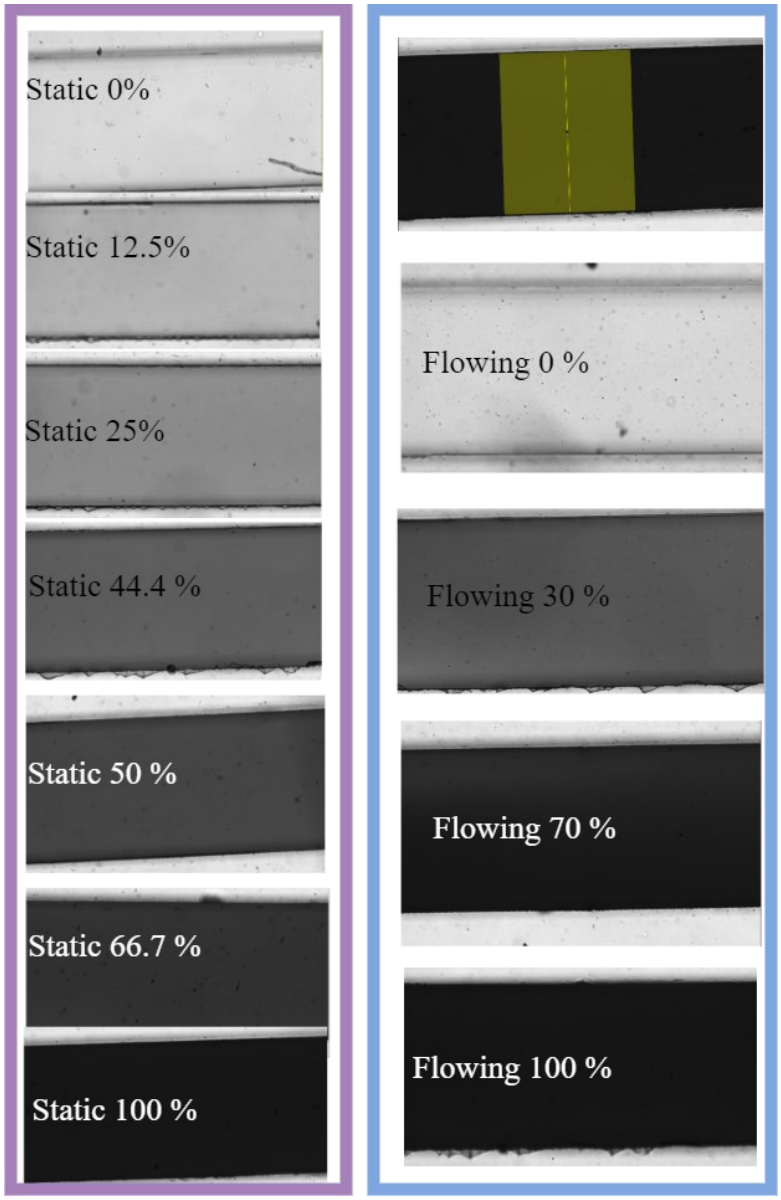

Figure 31 Purple rectangle-from top to bottom static food dye in the channels from 0% to 100% going down. Top of the blue rectangle- Example of the ROI selected to calculate the average pixel signal. Going down the images of the control, 30% 70% and 100% channels are seen under flowing conditions of 200 µL/min.

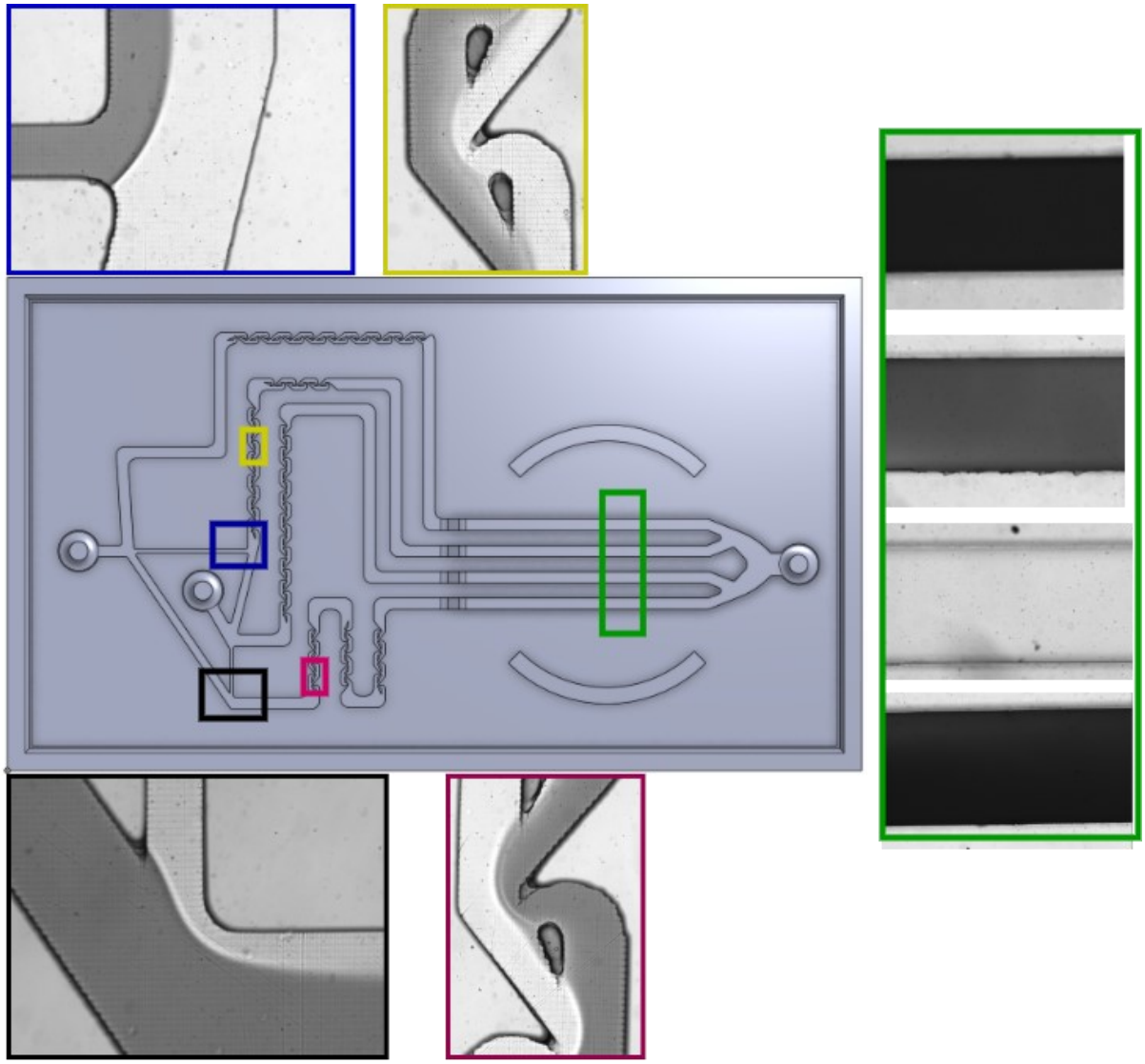

Figure 32 Sample images at important locations in the flow path of the chip. In the black and blue rectangles, the entrances to the 70% and the 30% channel are shown. In the red and yellow rectangles, the tesla mixer is shown mixing the two liquids. In the green rectangle, the flow of the 4 different channels at 200 µL/min can be seen.

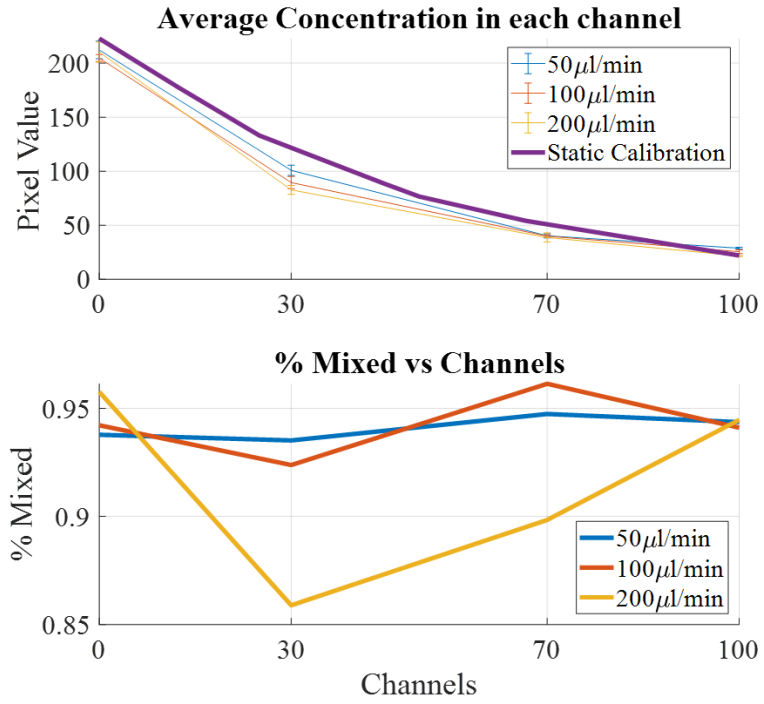

Figure 33 Top- Effect of the input flow on food coloring pixel value. Bottom- Efficacy of mixing, expressed in % mixed for each channel for the three different flows.

4.1.2.3 Flowing Bubbles

When using the original design of the chip, we noticed a couple of problems when studying the distribution of microbubbles under flowing conditions. Two major issues were found. Due to the innate slicing nature of additive manufacturing, angled surfaces, like the one at the entrance of the testing section, print similar to a staircase. These staircases cause bubble accumulation and led to an inconsistent bubble concentration. Similarly, printing defects at the surface of the channels can also cause imperfections where bubbles accumulated and lead to further inconsistent bubble concentrations. The implications and the solution to both of these problems will be discussed further in "Section 5.1.3.1 Surface Modifications for Bubble Flow". The following results were obtained using the new chip manufactured with a smooth surface. Note that, only the results displayed in this section (4.1.2.3) were obtained with the new chip version. The rest of the figures and results in this chapter were obtained with the older version.

We evaluated the ability of our new chip design to titrate MB concentration by recording videos of flowing MB. These videos were analyzed using three readouts. Still frames from these videos can be seen in the first column of Figure 34a-d. First, the bubble count was obtained using a built-in MATLAB function to find circles in an image (imfindcircles). The function gave the total number of bubbles and their size. The resulting circles can be seen highlighted in blue in the second column of Figure 34.

The tables below show the average count, size, and speed for each of the flowing channels (100%, 70%, 30% and 0%). Table 3 shows the bubble count and Table 4 shows the average size of the bubbles. We found that MB concentrations of 65% and 32% using input flows of 200 µL/min, which is within 5% of the 70% and 30% expected values. The bubble size did not differ from each other at an average 3.4 µm ± .6 µm and matching the .98-3.99 µm diameter range from the previous measurements in literature [123]. Next, TrackMate [122](a particle-tracking ImageJ plugin) was used to assess the speed of the bubbles in the videos. We found an average bubble speed in the 100%, 70%, 30% channels to be 41 µm/s ± 4 µm/s with little variation between the channels. The third column of Figure 34, highlights the tracks of the bubbles, and Table 5 shows the resulting average bubble speeds. In Tables 3-5 each chip shows two measurements as each channel was imaged twice at different locations.

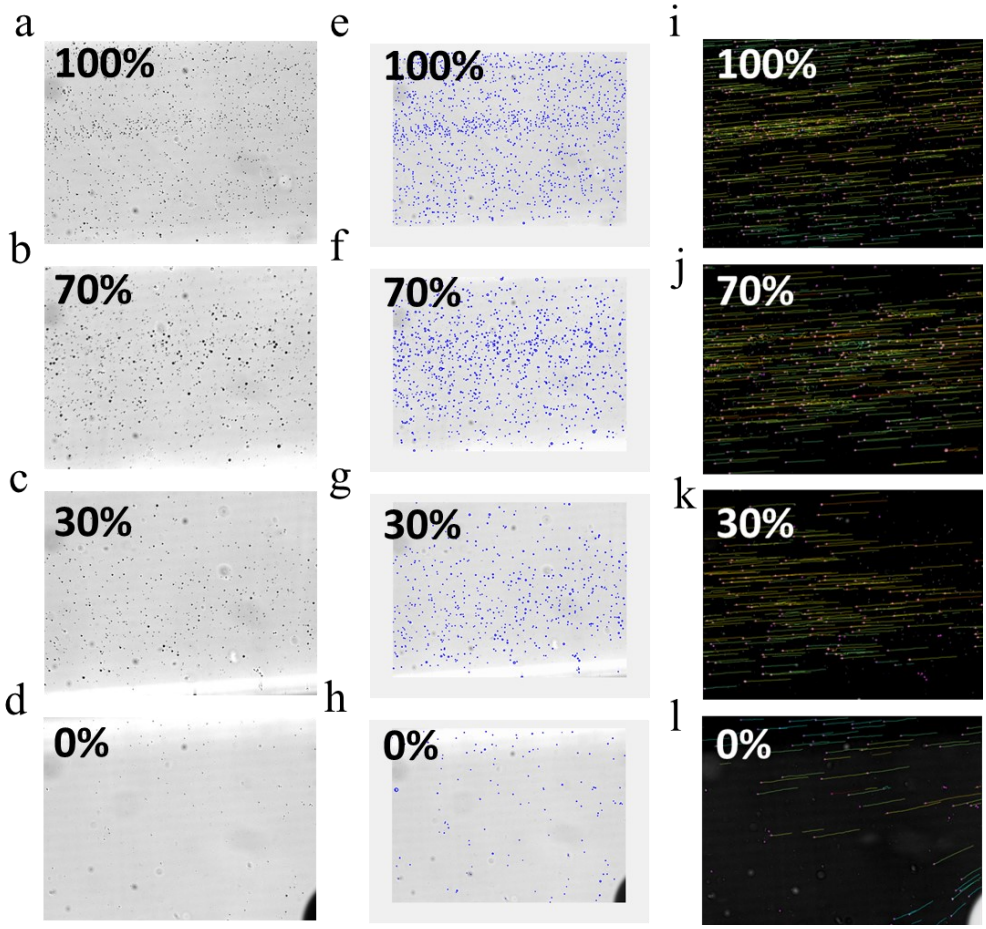

Figure 34 Example of frames taken from videos of microbubbles flowing in the four channels of the microfluidic chip. In the first column (a-d) the raw frame is shown. The dots seen are the MBs flowing at the roof of each of the channels. The second column (e-h) shows the output of the MATLAB circle finder function as blue circles. These were used to assess the count and the size of the MBs. The third column shows the resulting tracks from the TrackMate program. These were used to quantify the speed of the bubbles.

Bubble Count

Channels	100	70	30	0
Chip 1	988	843	457	86
	1837	809	283	59
Chip 2	1372	720	274	150
	933	759	369	228
Chip 3	1945	921	495	30
	2059	904	522	407
Chip 4	741	674	441	153
	999	974	422	211
Chip 5	1805	1588	591	202
	1537	1101	627	172
Average	1422	929	448	170
Percentage	100%	65%	32%	12%

Table 3 Bubble count at the roof for 5 chips with the smooth surface

Bubble Diameter (μm)

Channels	100	70	30	0
Chip 1	3.03	2.48	2.63	2.42
	2.48	2.56	3.21	3.21
Chip 2	2.92	3.18	2.85	3.39
	2.98	3.02	3.15	2.65
Chip 3	3.75	3.53	3.79	5.57
	3.56	3.47	3.44	4.71
Chip 4	3.19	3.96	3.67	5.45
	3.00	2.90	4.25	4.10
Chip 5	2.89	2.82	2.98	4.46
	2.72	2.61	2.93	3.94
Average	3.05	3.05	3.29	3.99

Table 4 Bubble size at the roof for 5 chips with the smooth surface

Bubble Speed (μm/s)

Channels	100	70	30	0
Chip 1	34.60	41.28	37.59	17.80
	38.96	37.37	34.22	35.98
Chip 2	35.83	44.79	51.68	6.91
	46.24	52.62	38.76	22.67
Chip 3	64.80	32.24	25.04	2.33
	34.95	24.48	23.36	2.17
Chip 4	40.38	42.68	21.79	1.19
	54.23	43.12	24.63	9.50
Chip 5	46.16	35.53	26.91	7.69
	25.75	32.77	31.97	1.24
Average	38.91	44.01	40.57	20.84

Table 5 Bubble speed at the roof for 5 chips with a smooth surface

4.1.3 **Static Cell Viability with 4T1**

Cell viability was assessed using fluorescent imaging with Calcein (green) as a live marker and PI (red) as a dead stain. A total of 1017 images were analyzed which were split across six conditions, tested on separate chips and repeated five times. Each chip had 4 channels imaged separately with 5-10 images per channel. In the first column of Figure 35, five sample images artificially colored are shown. In each channel, images were taken using a monochrome camera and Otsu's method was used to automatically segment the image into a binary area. The second and third column in Figure 35 shows the black and white signal with the thresholded area overlayed on top (green for the "alive area" in the second column and red for the "dead area" in the third).

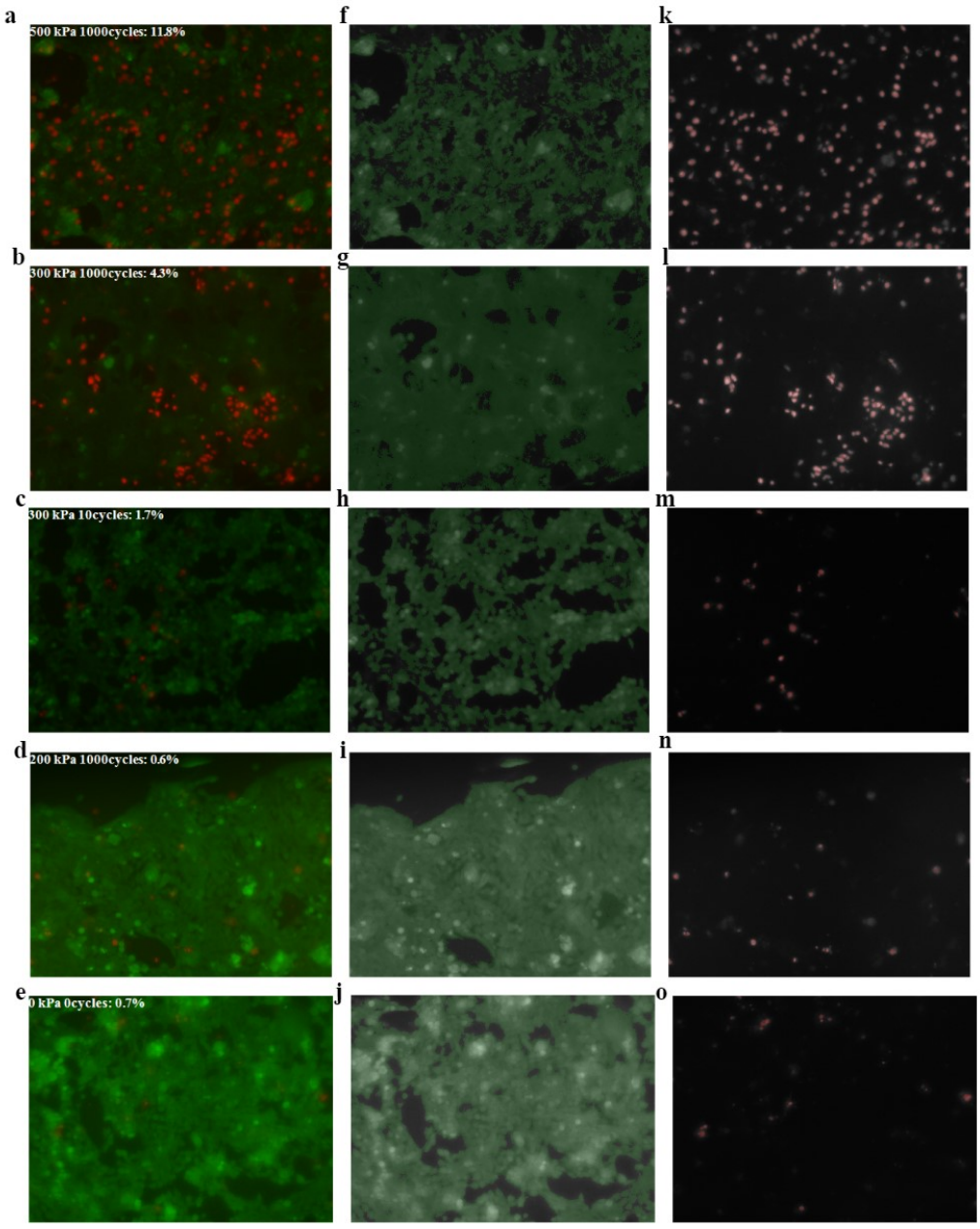

Figure 35 a-e) Examples of pictures of 4T1 cells with the Calcein and the PI images superimposed. f-j) The Calcein channel superimposed with the automatic threshold. k-o) the PI signal superimposed with the automatic thresholded image.

The median percent dead cells varied between 2.42% to 9.43% across all conditions seen in Figure 36. Both, the number cycles and pressure had an effect on percent dead cells, (all $p < 0.001$, one-way ANOVA). At 300 kPa we found a significant difference between the 1000 and 10 cycles ($p < 0.01$, Tukey), and the 1000 and the control ($p < 0.01$, Tukey). At 1000 cycles, we found differences

between 500 kPa and the 200 kPa, the 500 kPa and the control, and the 300 kPa and the control (all $p < 0.01$, Tukey). The difference between the 300 kPa and the 200 kPa was also significantly different ($p < 0.05$).

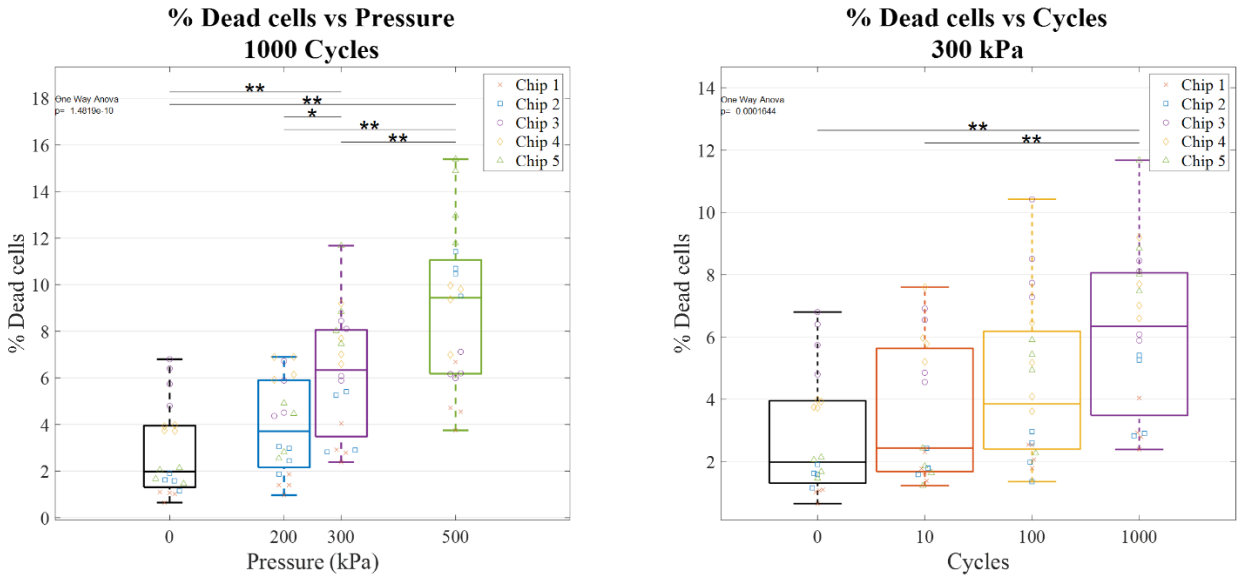

*Figure 36 Boxplot of % dead cells depending on #cycles and US pressure after a single US pulse. Each dot represents the average value for one channel in each chip. N=20 (5 repeats, 4 channels per chip). One-way ANOVA followed by Tukey multiple comparisons. *p < 0.05; **p < 0.01.*

4.1.4 **Static ATP Release**

To understand the spatial distribution of the signal, all ATP experiments included a brightfield image of the channels and the US probe. Figure 37 aims to show the distribution of the ATP signal by overlapping the signal with the brightfield image. Given the wide range of signal intensities (pixel values at peak intensity between 1500 and 600), the dynamic ranges of the signals were adjusted to understand the distribution of the signal more easily. Notice that all of the ATP is contained within the channels. Also, it only appears in the area around the US probe even though luciferin, luciferase, and MB were present all along the channels.

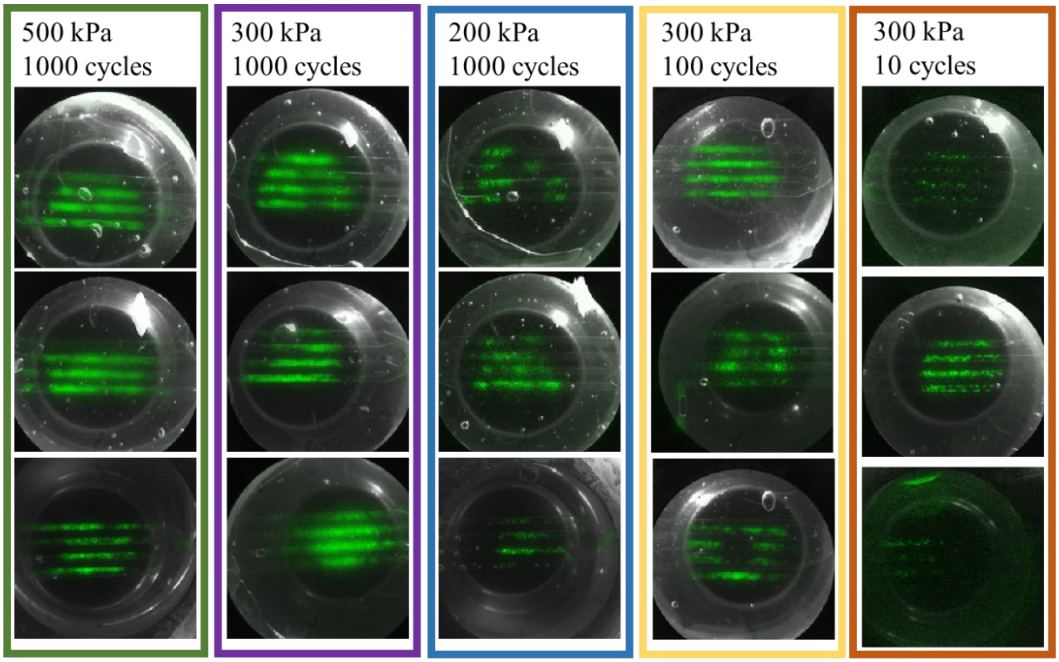

Figure 37 Examples of the ATP signal superimposed with the brightfield image. The ATP signal was scaled for better visualization.

Across all pulses, the median ATP released varied between 0.05 pmol and 2.20 pmol. Comparing these results to Tan el al.[85] where cells were stressed by stretching. Our ATP released is equivalent to the ATP release amount by a strain of 5% to 9% [85]. The median ATP release speed varied between 0.01 pmol/sec and 0.12 pmol/sec. Both pressure and number of cycles had an effect on ATP release (Figure 38) and ATP release speed (Figure 39) (all $p < 0.001$, one-way ANOVA). Upon multiple comparison testing, we found differences between the 300 kPa/1000 cycles and the 300 kPa/10 cycles pulses, and between the 300 kPa/100 cycles and 300 kPa/10 cycles pulses (all $p < 0.01$, Tukey). Similarly, we found a difference between the 500 kPa/100 cycles and 200 kPa/1000 cycles pulses, and between the 300 kPa/1000 cycles and the 200 kPa/1000 cycles pulses (all $p < 0.01$, Tukey). ATP release speed was also different between 300 kPa/1000 cycles and the 500kPa 1000 cycles ($p < 0.05$, Tukey).

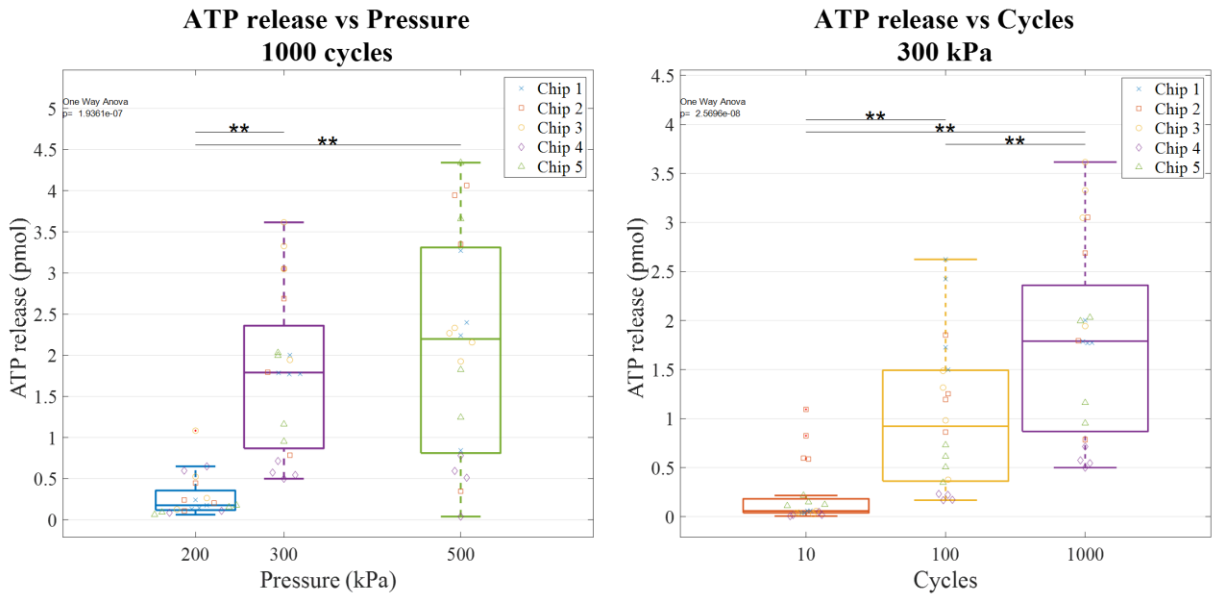

*Figure 38 The ATP released by the 4T1 cells dependent on cycles and US pressure. Each dot represents the average for one channel in each chip. N=20 (5 repeats, 4 channels per chip). One-way ANOVA followed by Tukey multiple comparisons. *p < 0.05; **p < 0.01.*

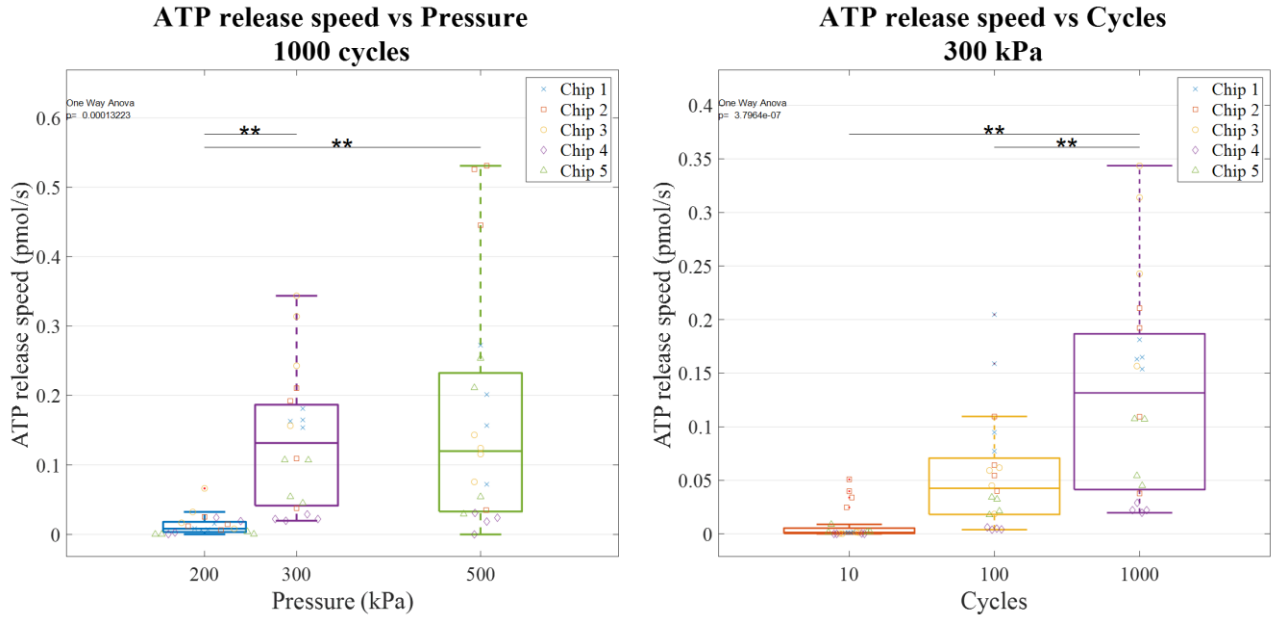

*Figure 39 The ATP released speed by the 4T1 cells dependent on cycles and US pressure. Each dot represents the average for one channel in each chip. N=20 (5 repeats, 4 channels per chip). One-way ANOVA followed by Tukey multiple comparisons. *p < 0.05; **p < 0.01.*

The third readout of interest was the time between US exposure and the peak ATP signal. The median time to peak varied between 12 to 26 seconds (Figure 40). A one-way Anova on the time to peak showed no dependence on pressure (p=0.3) but did find a significant dependence on cycles (p=0.005). The only statistically significant difference between groups occurred between the 300 kPa 100 cycles and the 300 kPa 10 cycles, and between the 300kPa 100 cycles and the 300 kPa 10 cycles.

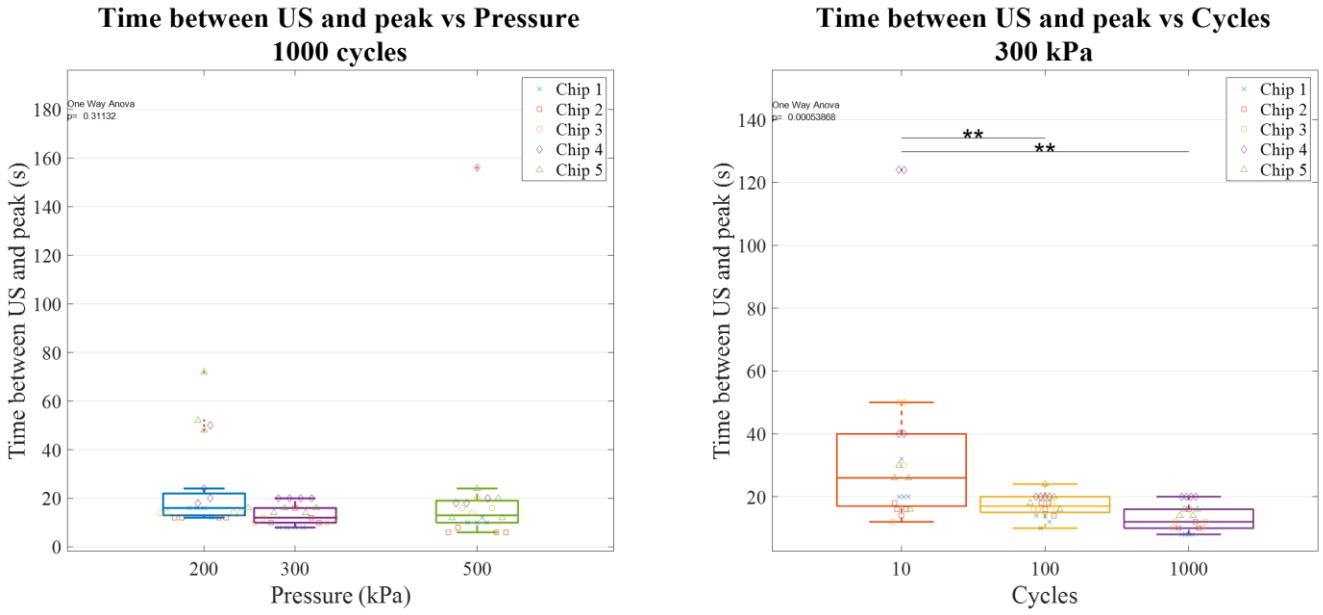

*Figure 40 Time between the US activation and the peak signal plotted against cycles and US pressure. Each dot represents the time constant for one channel in each chip. N=20 (5 repeats, 4 channels per chip). One-way ANOVA followed by Tukey multiple comparisons. *p < 0.05; **p < 0.01.*

Besides plotting the ATP release and the speed, we also examined the consumption rate of the ATP after treatment. Results are shown in Figure 41. The low signal conditions (200kPa 100 cycles and the 300 kPa 10 and 100 cycles) yielded flat curves. This resulted in a fitted curve with a very high time constant. The average time constant rate of consumption hovered around 400 seconds.

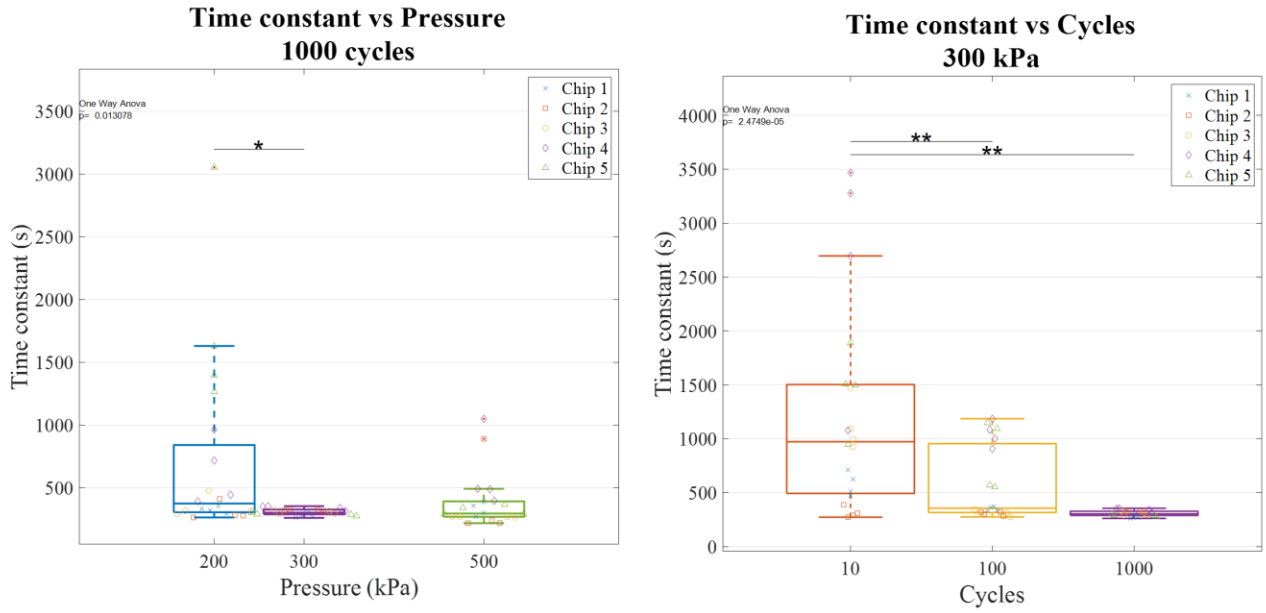

*Figure 41 The ATP consumption rate time constant by the luciferin and luciferase assay plotted against cycles and US pressure. Each dot represents the time constant for one channel in each chip. N=20 (5 repeats, 4 channels per chip). One-way ANOVA followed by Tukey multiple comparisons. *p < 0.05; **p < 0.01.*

4.1.5 **ATP Released vs % Dead Cells in Static Conditions**

ATP released and % dead cells are plotted against each other for all the tested pulses in Figure 42. We can identify two regions in this graph: (1) a region with ATP release (~1pmol) but low cell death (1% increase compared to control), corresponding to lower energy pulses (blue line); (2) a region with a marked increase in ATP release (up to 2.5 pmol) but with higher cell death (6% increase compared to control), corresponding to higher energy pulses (red line). Interestingly, these two regions show different slopes of ATP release as a function of % dead cells which differ by a factor 6, suggesting different release mechanisms (respectively (1) non-lethal and (2) lethal mechanisms)

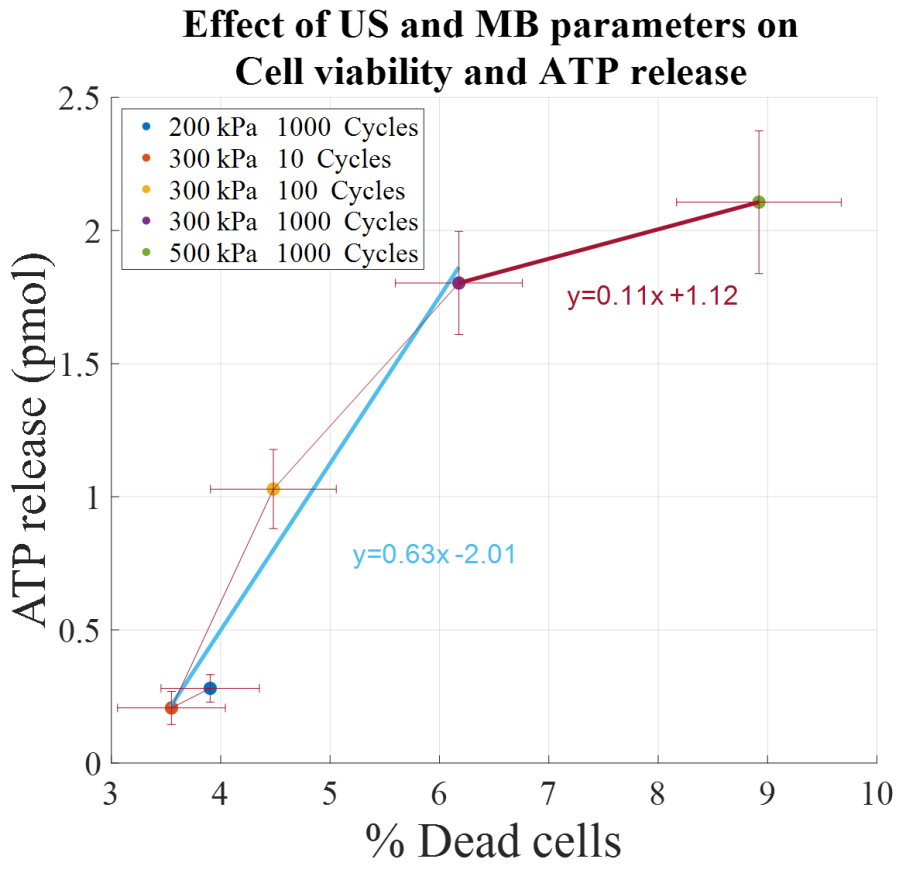

Figure 42 Each condition is shown as a dot plotted where the average % dead cells against the average ATP released. Two sections can be seen: a section in blue representing conditions where ATP is released with low cell death; and a section in red representing conditions where ATP is still released but with an increase in cell death.

The ATP release speed is plotted against cell death in Figure 43. This data seems to suggest that higher US energy causes bigger holes and faster ATP release speed at the cost of increased cell death.

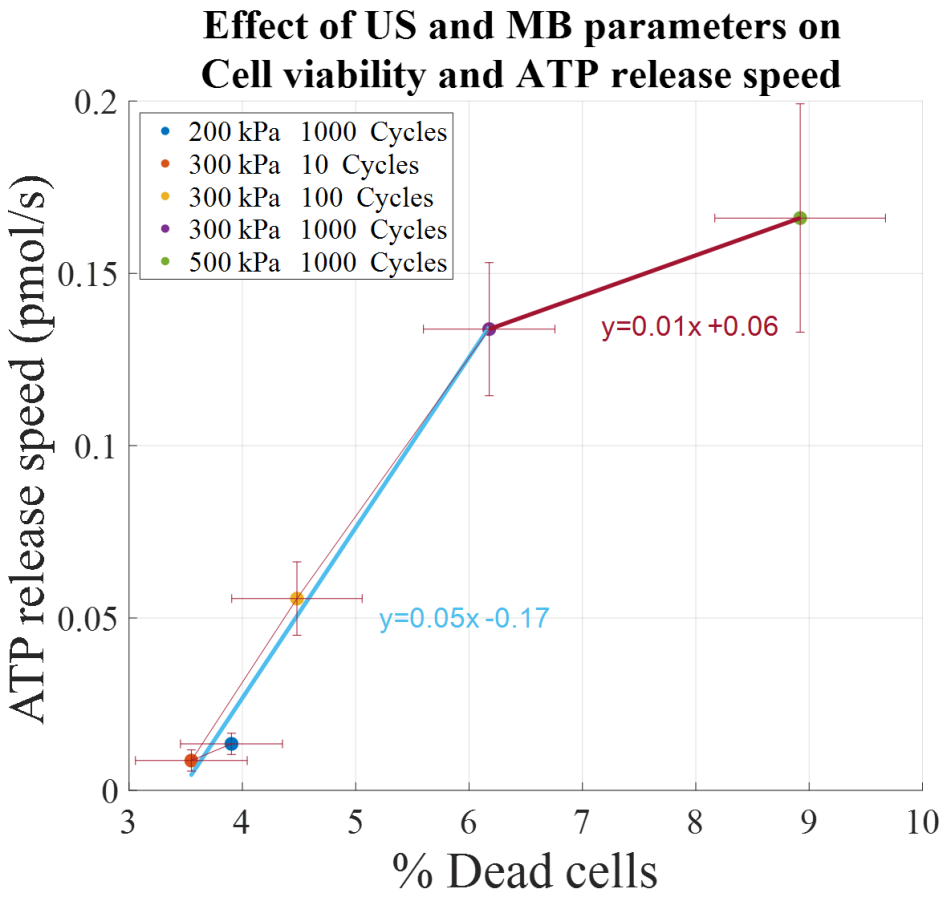

Figure 43 Each condition tested as a dot plotted where the average percentage cell death against the average ATP release speed.

4.1.6 **HUVEC Viability in Flowing Conditions**

We performed one experiment with flowing bubbles on HUVECs cells. Three chips were seeded with cells, one served as the control where flowing bubbles were perfused, but no US pulse was sent. One was subjected to 3 consecutive US pulses with a 2 min time interval (simulating MB replenishment) and the last one was subjected to a single pulse. The Calcein and PI images are displayed in the first column of Figure 44. In the corner of each image, the % dead cells is displayed for that specific picture. The second and third columns show the cell segmentation used to count the alive (second column) and dead cells (third column). For the 100% concentration channel, 3 pulses caused 48.7% dead cells, compared to 29.7% with a single pulse. In the 70% concentration channel, 3 pulses also caused a higher % dead cells compared to the

single pulse conditions (Figure 45). Overall, decreasing MB concentration decreased % dead cells. The control channel and the 30 percent channel had a similar % dead cells when compared to the control chip that was not treated with an US pulse at 9.8% dead cells. These results support that multiple pulsing is possible in flowing conditions, although the robustness of these results will need to be tested more rigorously with additional repetitions.

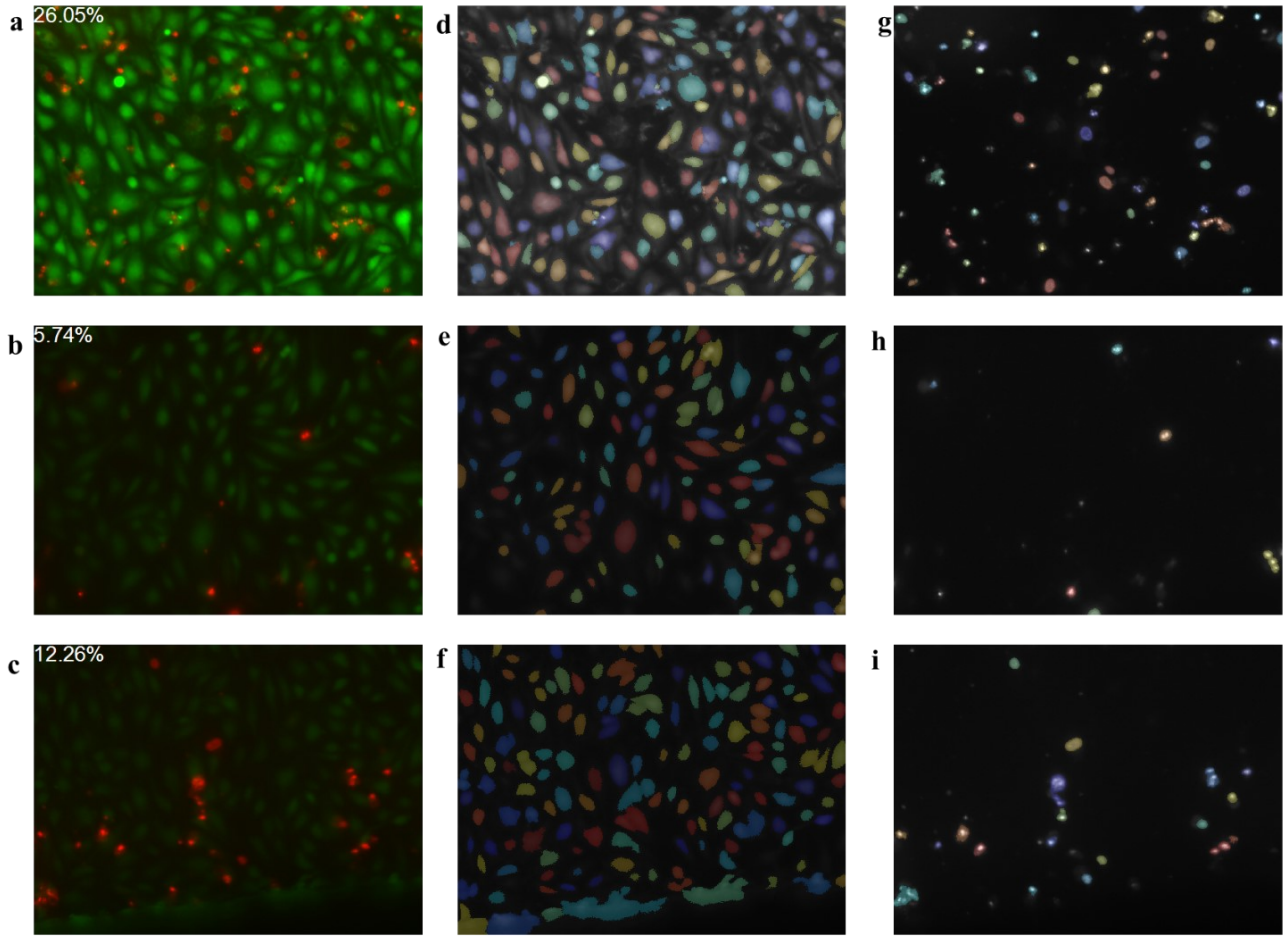

Figure 44 a-c) Examples of pictures of HUVEC cells with the Calcein and the PI images superimposed. d-f) The Calcein channel is superimposed with the automatic watershed transform segmenting out the cells. g-i) the PI signal is superimposed with the automatic watershed transform identifying the dead cells.

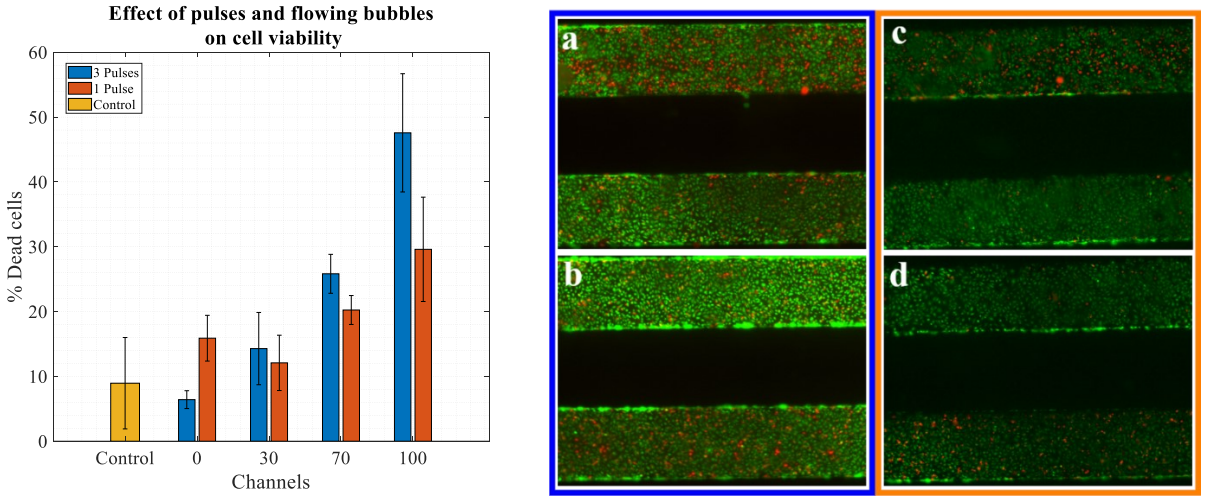

Figure 45 In the blue rectangle the effect on cell death of the 3 pulses on HUVEC cells with flowing bubbles while the orange rectangle displays the effect of a single pulse. a) Shows the fluorescent image of the 100% and the 30% channel. b) Shows the images for the control and the 70% channel. c and d) Show the same channels but for the single pulse experiment.

Chapter 5 Discussion

Overall, in this work, we have developed a microfluidic device that allows culturing cells, mixing of two phases to multiplex MB concentration, transmitting US excitation, and imaging with microscopy. We have been able to create cell monolayers for both the cancer model (4T1) and endothelial cells (HUVECs). We have also developed automated image processing algorithms to quantify cell viability using Calcein and PI staining. Using these techniques, we have demonstrated that cellular viability and ATP release can be imaged via fluorescence and bioluminescence following US excitation. Two modes of operation were tested: (1) for static studies, liquids were easily perfused via pipets using the output port; the 4 channels were then submitted to identical experimental conditions and allowed for replicate experiments; (2) for studies with flow, MB and dilutant phases were injected at the same flow rate to generate 100%, 70%, 30% and 0% MB concentration in the four channels and allow multiplexing of MB concentration. For the first time (to the author's knowledge), ATP release following MB/cell interactions was quantified. We could demonstrate the amount of released ATP and the rate of ATP release increased with % dead cells. Interestingly, with low energy US, there was a region that caused a release of ATP but only a very small increase in cell death. We will now discuss our findings in more detail and provide our perspectives for the next steps and possible improvements for this project.

5.1 Microfluidic Device

5.1.1 Manufacturing and Handling

We have been successful at creating PDMS-based microchips to study MB/cell interactions following ultrasound excitation. We chose to use a 3D printer at this stage, which was a great advantage in the early stages of the design process, where multiple ideas and iterations were easily manufactured and changed. For instance, earlier models included testing sections with a low channel height (150 μm). This did not provide enough media for cells to consume and caused cell death while culturing. Adding extra height (700 μm) in the testing section allowed for more nutrients to be available for the cells. We also found that there was insufficient mixing with the initial 6 units of tesla mixers. While the results were good for the food dye experiments, with MB,

we found that extra mixers needed to be added: indeed because of buoyancy, MB at the top level did not mix as well as food coloring. However, once testing started to ramp up and no major feature changes were made in the design, we did not switch the mold to a more permanent solution. This meant the 3D-printed molds were used to their limits. A better approach would be to manufacture the chips using CNC molds out a more durable material.

In this initial attempt, we obtained satisfying results in static conditions and have been able to relate ATP release and release speed with increasing ultrasound energy. While the system worked well, there are a few design changes that could improve the microfluidic chip.

5.1.1.1 -6dB US area

The chip design used in all these experiments had a major flaw that was overlooked in the early stages of the project. The overall channel separation was designed to be 6mm apart. However, the -6dB beam diameter at the focal point, is only 3.2 mm. This meant that the outermost channels did not receive the same amount of pressure as the innermost channels. Future iterations of the chip will include a channel separation of less than 3.2mm.

5.1.1.2 Problem with Trapped Air

If not careful, bubbles would be accidentally injected into the system and since the chip had multiple branches, these were harder to get rid of. Resulting in the liquid had to be sucked out to start anew. As long as bubbles did not stay inside the testing section, they were not a critical failure for static tests, but needed to be cleared for testing with flowing microbubbles. Extra care and precision had to be implemented when prepping flow experiments. Air bubbles are a common in PDMS devise because of evaporation through the material [124]. The best way to avoid them is to make sure no bubbles get trapped. But as they are inevitable, the best option is to actively flush them out [124].

5.1.1.3 Improvements

Firstly, rare occurrences happened where the output port section was too small for proper bonding between the two halves of PDMS. This meant that sometimes, the liquid escaped via slim

gaps between the two halves instead of running through the channels. Moving the location of the output port a little further from the mold wall would help solve this problem. Furhtermore, once a final design that works reliably is identified, it is recommended that the mold should be manufactured out of a more durable material like aluminum to minimize scratches and wear. The design includes a large space between the mold walls and the channel walls, in this section, a larger chamfer could be added to help demold.

5.1.2 **PDMS Attenuation**

We measured attenuation using a 2.5mm slab (thickness of the roof layer) of PDMS manufactured using the same procedure as that of our microfluidic chips. In three different experiments, we showed that the microfluidic device does not attenuate the US pressure wave (<5%, Figure 29). A 5% reduction of the slab thickness translates to a -1.78 dB/cm attenuation matching literature reposts of 2.35 ± 0.28 [121]. We tested different slabs of PDMS made from three different batches on three different days, and no difference in attenuation was obtained. We also tested the three different pressures, and again no difference in attenuation was seen. Finally, we tested different locations of the same slabs to test if the PDMS was nonhomogeneous and again no difference in attenuation was seen. This gives us confidence that the US pressure that acts on the MBs in one chip is the same as in another chip.

5.1.3 **Microbubble Mixing**

The effectiveness of the concentration divider was tested with two different methods. To understand the efficiency of the chip design, food coloring was used as a marker to quantify concentration and distribution. While it is a simple tool, the food coloring experiments gave us insight into the effectiveness of the concentration divider and the mixing function. We noted that an input current of 200µL/min food dye showed a mixing efficiency of over 85% (Figure 33). The visible cues from these dye tests helped identify problems in older molds. However, food coloring is not used in real experiments so images and videos of flowing bubbles would have a more meaningful impact. Since they are too small to detect at lower magnifications (4X), the distribution of the bubbles across the entire channel is not possible. However, at higher magnifications (10X), bubbles can be seen and can be tracked using TrackMate (ImageJ Plug-in).

Using Matlab code and the tracks, we could quantify the number of bubbles, their size and their speed, in each channel (Table 3, Table 4, Table 5). With this direct measurement, we are confident that the chip can create a multiplexed environment to test the therapeutic pulse.

Differences in the microbubble concentration between the measurements and the designed chip are being investigated. One possible cause could be imperfections of manufacturing and usage of the molds. With successive usage, the accumulated scratches and defects can alter the resistance of each of the branches. Since the MBs of interest float to the top layer, they are very susceptible to surface rugosity. Some examples of how mold usage affects channel geometries are seen in Figure 46. We have recently decided to prepare a smoother surface for the roof section to minimize MB accumulation in surface imperfections during transit. This could be obtained by pouring PDMS in a petri dish and curing it instead of manufacturing the top half in a mold, as previously done.

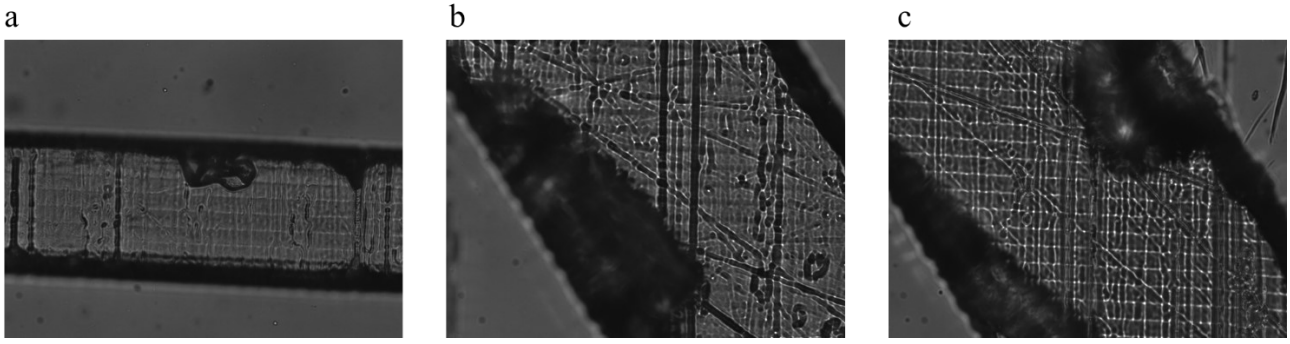

Figure 46 Three examples of scratches and mold usage translating into changes in channel geometry. a) The small channel carrying MB into the 30% channel being significantly affected in cross-sectional area. b-c) Intrusions into the channel of the 70% MB carrying channel.

Secondly, the resistance equation for rectangular cross-sections is an estimation. While a fairly good estimation, it does require that the height be much smaller than the width, and in the worst-case scenario when the cross-section is square, the resistance estimation has a 13% error [89]. To estimate the effect of using Equation 3.12 we calculated the difference between the resistance values used against the true analytical infinite sum solution given in Equation 5.1 [91].

$$R_{hyd} = \frac{12\eta L}{h^3 w} \cdot \frac{1}{1 - \sum_{n\ odd} \left(\frac{192\ h}{\pi^5 n^5 w} \cdot \tanh\left(\frac{n\pi w}{2h}\right)\right.} \tag{5.1}$$

Table 6 shows that we expect a 2% error from the modeling equations in the smaller channels. The 13% error in section 2 of resistances 7-10 is negligible as the modeling equations only require that:

$$R_7 = R_8 = R_9 = R_{10} \tag{3.2}$$

Given that all the $R_{7\text{-}10}$ are all equal, no matter the error, then using the estimations should not change the outcome.

	Segment	Height mm	Width mm	Length mm	Error in Resistance
	1	0.15	0.70	12.00	0%
	2	0.15	0.49	11.20	0%
	3	0.15	0.21	7.63	2%
	4	0.15	0.21	3.82	2%
	5	0.15	0.49	5.60	0%
	6	0.15	0.70	6.00	0%
7,8,9,10	Section 1	0.15	0.70	31.50	0%
	Section 2	0.70	0.70	16.50	12%

Table 6 Error from hydraulic resistance equation approximation.

5.1.3.1 Surface Modifications for Bubble Flow

As mentioned in Section 4.1.2.3-Flowing Bubbles, there were some modifications done to the chip to stop bubble entrapment with flow in the original design. Firstly, in the original design of the chips, the cells were cultured at the roof of the channels. This section curved upward compared to bubble flow as seen in Figure 47. Due to the slicing method of 3D printing, any angled surface will come out as staircases. These staircases are the perfect candidate to trap floating bubbles. (see Figure 48). As time went on, the bubbles would accumulate causing the concentrations downstream to behave in undesired ways. In some cases, the problem went as far as to create environments where the 70% channel had more bubbles than the 100% channel. Similarly,

surface defects caused by either scratches in the mold or by printing lines, created features that could also trap bubbles. Again, causing bubble accumulations and inconsistencies in the overall concentrations in the channel. Figure 47 and Figure 48 both show the effect of surface defects on bubble entrapment. The solution to both of these problems is portrayed at the bottom of Figure 47. Here, we simply manufacture the chip so that the testing area curves away from the roof and we use a smooth surface PDMS as the top half of the chip. This meant manufacturing PDMS in a petri-dish to obtain a smooth surface and poking the inlet and outlet holes in the smooth PDMS instead of in the molded part.

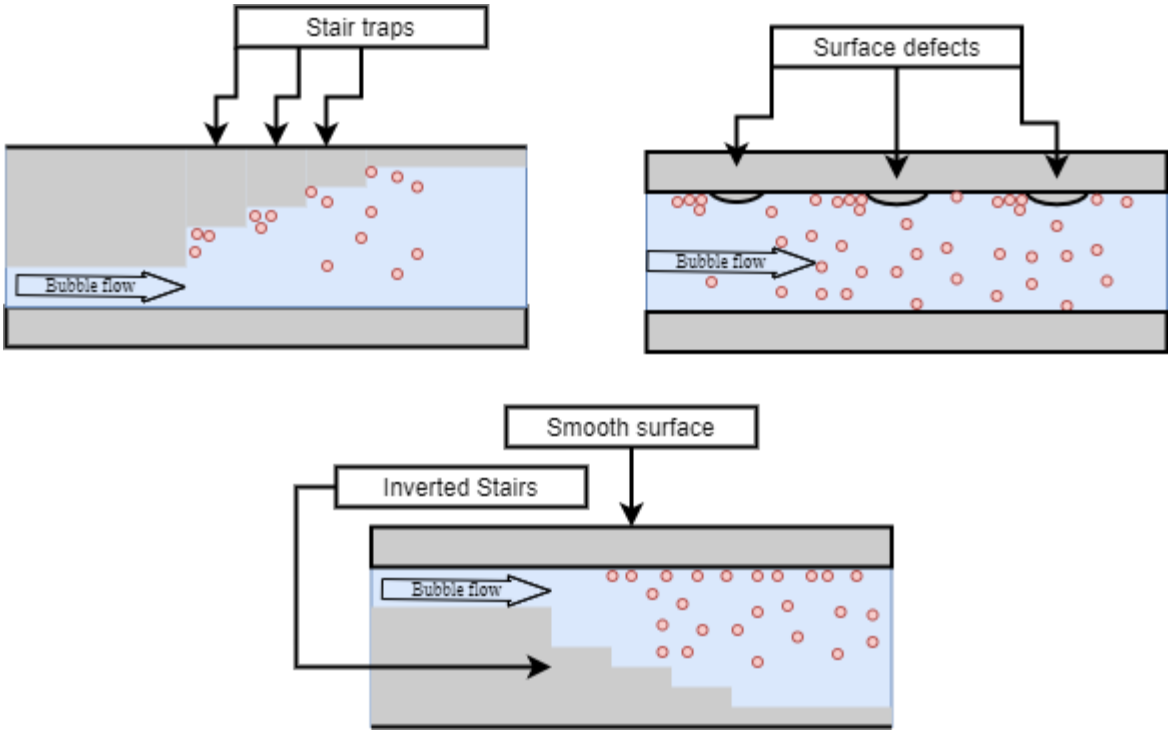

Figure 47 Problems with bubble entrapment due to surface roughness and stair traps in the original design. Bottom- An illustration of how the new chip is made to minimize the bubbles from being trapped.

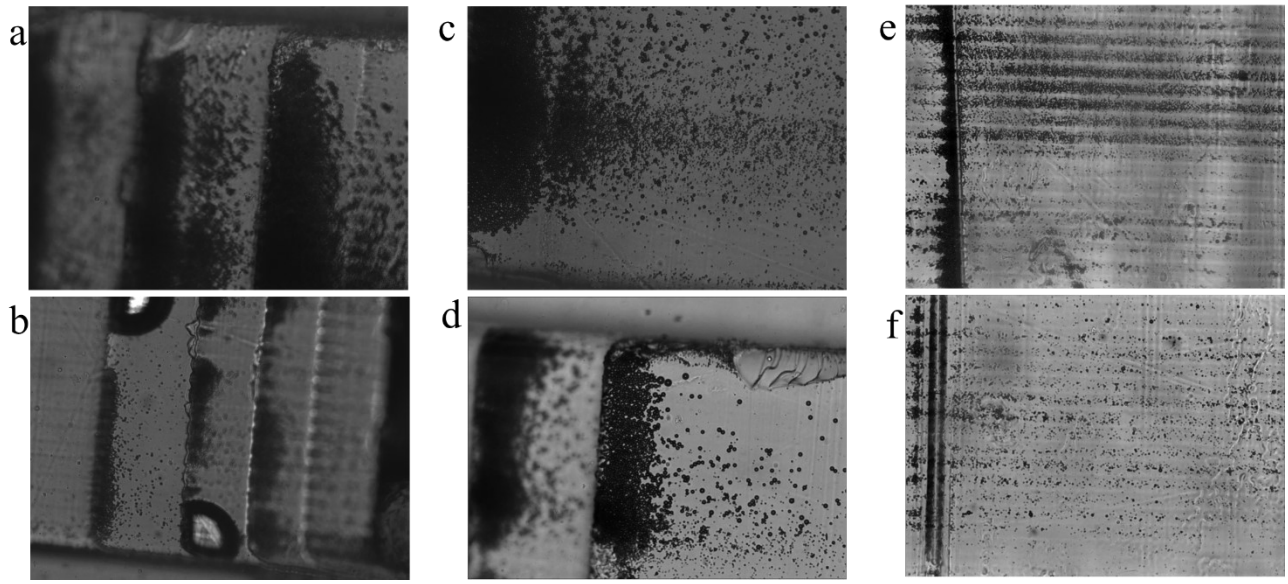

Figure 48 a-d) The staircase traps causing bubble accumulations. e-f) Surface roughness features causing bubble accumulations in the roof of the chip.

5.1.3.2 Artifacts and small amounts of MB in the control channel

Figure 34 does show that in the control channels, MATLAB and Trackmate managed to locate circles. Most of these circles can be attributed to either static circular artifacts, stray bubbles, or other particles in the system. Due to the optical nature of the bubble count some of these noise issues are harder to fix. The static artifacts could be removed by averaging frames over time and removing noise. This type of image processing also decreases the contrast the bubbles have with the frame background, making them harder to detect.

Small amounts of stray bubbles or other particles in the system can be seen travelling inside the control channel. Bubbles can get stuck inside the control flow either when inserting the syringes or when moving the chip to image. Here, the input flow can be altered and some bubbles coming from either the 70% or the 30% merging channels can escape into the control flow path.

Given that the frames were not taken inside the hood, there could be some particles in the air that can get into the fluid and some of these could be seen in the control channel and be counted as a moving bubbles.

To contextualize this noise, we can see that these two errors compound to give an estimated 12% bubble count in the control channels (Table 3) and because the code counts other circular artifacts as bubbles we can see that the size of the circles in the control channel don't exactly match the size in the other two channels, 3.99 vs 3.00 μm (Table 4). Similarity, the algorithm detects static artifacts as bubbles and the average speed of these circles is lower than the other three channels, 20μm/s vs an average of 40 μm/s (Table 5).

5.2 **Cell growth**

5.2.1 **4T1 Cell Line**

We used 4T1 cells as an initial model for this study. However, this is a major limitation for all of the static tests shown in this project. Indeed, in vivo, MBs interact with endothelial cells and not directly with cancer cells. This cell line was chosen to experiment in the early stages of the project because they are easier and cheaper to grow.

5.2.2 **Endothelial Cells**

We have also shown that the microfluidic chip has the capabilities to grow endothelial cells. Not only can we grow endothelial cells, we can take images and count individual cells that are either dead or alive. We have shown that we can cause endothelial cell damage with flowing bubbles. Moving forward the project should focus on studying the effects of microbubble therapy on HUVECs.

5.2.3 **Future Considerations**

Future designs should focus on finding the appropriate seeding methods and the replenishing of media. One of the major hassles with seeding cells in small volumes is the lack of nutrients available for the cells [124]. Inside small microchannels, the key factor in determining the distribution of nutrients is the height of the channel [124]. To avoid poor confluency and poor cell viability, any design should consider the how often the media should be replenished [124]. Other solutions to nutrient dispensation can include gravity driven flow (like the system used in [76]) or syringe pumps to replenish the media inside the small channels [124].

5.3 Image Analysis

To deal with the large amounts of images, the automated script chose the threshold for each image. This was done using Otsu's method. It has been shown to accurately and repeatedly divide the image into two categories based on signal intensity. Using this method, images were easily divided into cells and background, especially when a good contrast was present between the two. When taking images, for the algorithm to work best, a section of the image had to be dark. This way the algorithm could separate cell signal vs background. This mainly applied to locating the image in the Calcein pictures, as the PI images were mostly dark. Even if the image had a dark background section, there were still other features that could degrade the analysis. For example, in the presence of background noise or for a badly focused image, Otsu's method had a hard time finding a threshold value that made physical sense. In order to ensure that the image was acceptably thresholded, as the code went through, the thresholded images were shown to the user. Who would then mark them as acceptable or not. This removed noise and outliers from the analysis. Two sample images that were not used can be seen in Figure 51.

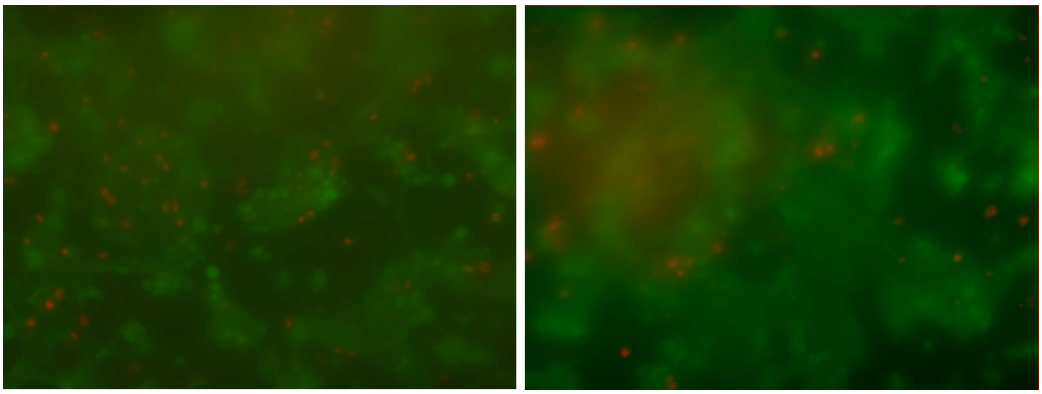

Figure 49 Two sample images with a blurry background or noise.

5.4 Static Tests

We have shown that our current methods are capable of causing ATP release but, depending on the US conditions, this was accompanied by cell damage, which was quantified using live/dead staining assays. Since ATP is a DAMP, this is not surprising: upon cell damage, intracellular ATP is released to the extracellular space. Indeed, MB cavitation is known to cause membrane damage that can lead to cell death [125]. However, there were US conditions that could release ATP

without causing cell death. The mechanism for this remains to be established. For instance, it could implicate the "ATP induced ATP release" mechanism involving the activation of the pannexin channels as described in section 2.2. Another possibility would be smaller holes that could reseal [66]. Depending on the application, cell death could be an issue or not. Indeed, for vasodilation, it may be important not to damage the endothelium. However, there are applications, such as for cancer immunotherapy, in which mild or even important damage could be beneficial. Mild damage that could trigger vascular inflammation and increase ATP accumulation in the tumoral space could enhance immunotherapy.

5.4.1 **Viability Studies**

We designed our experiments to minimize variability between them. To avoid getting effects from cells waiting outside the incubator too long while imaging and testing multiple chips, tests and imaging were performed in random order. To avoid selection bias, multiple pictures of the chips across the different channels were averaged (a total of 1017 pictures) to reduce variability. To help with the number of images taken, code and algorithms were necessary to repeatedly analyze large quantities of data. The protocol to take many pictures in rapid succession made it possible to image six chips in under 45 minutes.

5.4.1.1 Image Analysis

Since the cancer cell line was very confluent, it was hard to determine the borders between cells. This was the main reason for using the area of the cells instead of trying to segment the image. Early on in the project, there was an attempt to characterize cells as sonoporated, dead, or alive. This was achieved by having PI in the medium with the microbubbles. However, since the cells would stack on each other and have hard-to-define borders, it was impossible to distinguish if a cell was dead or sonoporated. In control images where no US was applied, there still seemed to be locations of the chip with both Calcein and PI. Instead, we shifted our focus to study viability. When studying viability, the cells were subjected to PI after sonoporation. By applying PI after sonoporation, we managed to avoid confusion between sonoporated and dead cells by only

studying dead cells. Simply, any red fluorescent cell was dead, thus avoiding the problem of sorting out areas of images with both green and red signals.

This problem was non-existent with HUVEC cells. Being larger in area and having more clearly defined borders helped to create an algorithm that could count the cells.

5.4.1.2 Limitations: Using Offline Methods for Cell Viability

The setup and the measurements were a result of the tools available to the lab at the time. This is limited to measurements of cell viability offline. In other words, the current microscope available to use did not have a way to image the cell's live. Hence the experiment had to take place away from the microscope. While we figured out a way to characterize cell death offline, there have been multiple groups and literature that have shown to image cells live when exposed to the US pulse. The lab is working on a solution to image the pulse live. Once that happens sonoporation experiments can happen and more data can be collected on the microfluidic chip.

5.4.2 **ATP Release Studies**

We have shown a direct effect of the US pulse on the release of ATP. We have quantified the amount of ATP that is released by the US and MB therapy. We have also quantified the kinetics of ATP release and have a quantitative analysis on the reaction times of ATP release after a therapeutic pulse. The process and equipment used for these studies have been well developed by Ju Jing et al. The knowledge they brought was of major importance for the scientific impact of this work. While others have seen the presence of ATP after sonoporation [31] they were not able to quantify the amount of ATP released and the release kinematics.

One of the interesting results from these tests was obtained with low energy pulses, where the ATP released could be seen as individual spots of the channel rather than covering the entire channel. Figure 50 exemplifies these different types of signals. These could be examples of single cell poration.

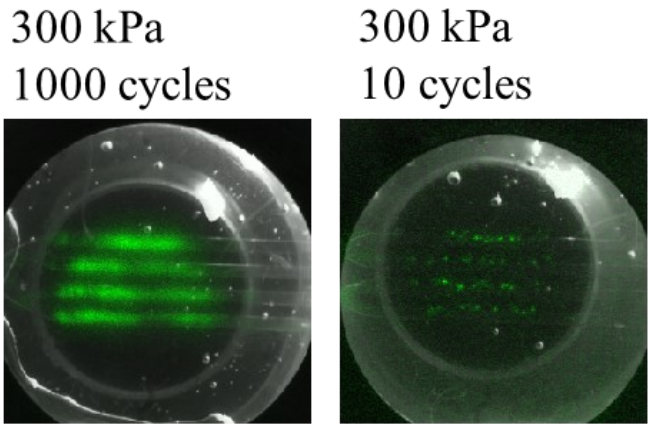

Figure 50 Differences between signal covering the entire channel vs single spot.

5.4.2.1 Time Constant

The time constant variable translates to the physical consumption of ATP due to the luciferin and luciferase reaction. The main contribution of this variable is to ensure that the signal measured is actually ATP. Our measures of the time constant go well with past literature on ATP release and the ATP consumption rate [85]. Our time constant values were 400s while literature showed to have a time constant between 362s and 587s depending on the ATP concertation. We found that ATP gets consumed very quickly, in a matter of minutes and cells stop releasing ATP after a single pulse. There is no sustained release of ATP after the ultrasound pulse. This is interesting to note as studies have shown sustained ATP release in mouse muscle for up to 20 minutes and even a low signal 24 hours after treatment [31].

5.4.2.2 Possible Release Mechanisms

There are two proposed mechanisms to describe the two regions of ATP released describe above. The first would be the prevalence of resealable pores in the lower energy regions. Resealable pores can still release ATP without causing cell death, explaining the relative increase in ATP without the increase in cell death in the lower energy regions.

The next proposed release mechanism would be ATP-induced ATP release through pannexin channels, again, as described above (Section 2.2) . There seems to be a negative feedback control loop of the ATP release through these channels. Here, the lower regions would release enough ATP into the extracellular space to activate the channel opening. On the other hand, the higher

energy pulses could release too much ATP and trigger the inhibitory effects of ATP in the activation of the P2Y receptors.

More data is needed to study the differences between the higher and lower energy pulses and their effect on ATP release.

5.4.2.3 Limitations

Limitation 1: Focussing One of the major limitations of the ultrasound setup was that focusing on the layer of cells that are being imaged became tedious. While focusing, the camera moved up and down the channel walls, while maintaining straight and crisp wall lines. However, once the machine was running the focus could not be adjusted as the camera was inside the dark shroud. This meant that in some of the images the signal was not in perfect focus as exemplified in Figure 51. To minimize the effect of unfocused signals the system deals with them on two different fronts. Firstly, the camera collects all of the light in the infinite column above the pixels. This means that even if the signal is diffuse, the pixels will still collect the data. Secondly, the algorithm integrates and sums the entire ROI. This means that even if the camera was not focused on the layer, the data was still collected and added up to count towards the amount of ATP released.

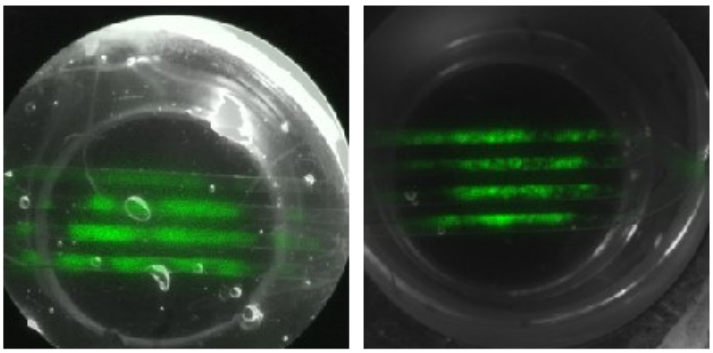

Figure 51 Two pictures showing the difference between a well-focused image (right) vs an unfocused signal (left)

Limitation 2: Alignment and US Beam Size Miscalculation Another limitation of the setup was the lack of consistent alignment. This led to a large spatial variation in signal. The tests were performed under a chip design where the visual marker was not yet put in place. The alignment

and the location of the US probe in comparison with the chip varied across all tests. Figure 37 shows exactly this problem. Notice that the US probe is sometimes smaller or larger depending on the picture. It can also shift its location relative to the channels, in some images the center of the US probe is not centered with respect to the channels while in others it is. Furthermore, the old design of the chip still had a large distance between the outermost channels (6mm in total). These earlier designs did not take into account the proper diameter of the -6dB ultrasound beam (3.2mm). Consequently, this study is subjected to some spatial variability caused by smaller pressures on the outer channels. Future design will include channels that are closer together and within the -6dB beam profile.

Limitation 3: Time constant estimation of low signal Another limitation of the study came from low energy pulses that released little ATP. With low amounts of ATP released the exponential fitting curves were susceptible to flat time course signals. This made the estimation for time constant very large when little ATP was released. Figure 52 exemplifies this with an example of a low signal ROI.

Limitation 4: Noise in estimation time to peak

Figure 52 also exemplifies the next limitation with low signal ROIs, the larger time for the signals to peak. Notice that the peak signal is close to the innate noise of the system. This pushes the peak of the signal further in time. This means that the large time to peak of the lower signal treatments is largely due to noise.

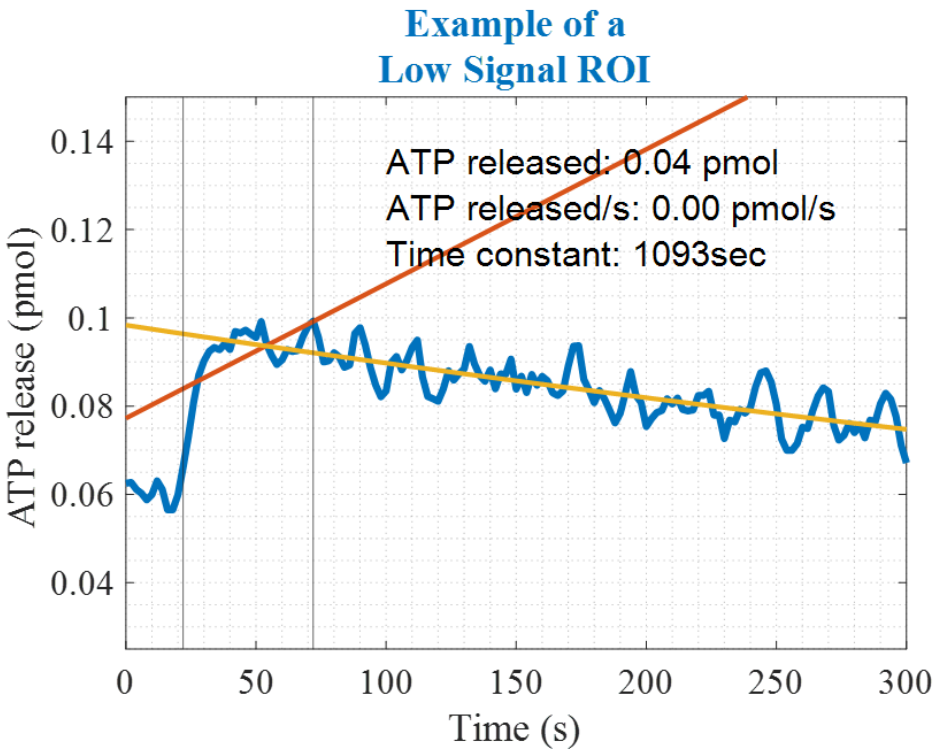

Figure 52 An example of a noisy signal inside an ROI. The two vertical black lines indicate the activation of the US pulse and the peak of the signal. Both of these time coordinates and ATP values were used in the analysis. The red line is the line of best fit of the signal between the two black lines. The slope of this line dictates the ATP release speed. The yellow fitted curve is an exponential fit of the signal between the second black line and the last time point. The time constant of that fit is the time constant used in the analysis.

5.4.3 Relation of ATP Released, Time to Peak, Release Speed and Cell Death

5.4.3.1 ATP Released and Cell Death

The offline analysis, performed on separate chips, allows us to link ATP release and cell death indirectly. According to the work presented in this project, ultrasound pulses affect the relationship between the amount of ATP released and cell death. Indeed, two trends appear in Figure 42. For the lower energy pulses (300kPa 100 cycles and the 300kPa 1000 cycles) there was an increase in the amount of ATP released but a relatively small change in cell death. For higher energy pulses (500 kPa 1000 cycles), we observed a marked increase in released ATP, however, this was accompanied by an increase in cell death. We theorize that this difference is attributed to reversible and irreversible sonoporation of the cells.

To support this interpretation, we first look at the work presented by Qiu et al [126]. They show that the intertidal cavitation dose (ICD), i.e. how much the bubbles activated, increases with both acoustic pressure and with the time of treatment [126]. They also studied cell viability (using PI and flow cytometry) and pore size (using SEM) after exposure to US and MBs, finding that pore size and cell viability increase with ICD. Furthermore, we know that large enough pores do not reseal [66] and that these non-resealable pores cause cell death [75].

With this in mind, the interpretation of our results is as follows. At lower energies, only a few cells get treated by the resonating MBs as seen in Figure 50. The pores created could temporarily let ATP flow into the extracellular space. Given the low amount of ATP released and the low cell death, the pores can be interpreted to be small and resealable. As the treatment intensifies, more cells get treated and slightly larger pores are formed. Hence, total ATP release increases, but cell death does not increase as the pores reseal. Further increasing the energy of the pulse still increases the ATP released as more cells are activated. However, we know that higher energies cause larger pores that do not reseal. Consequently, the pulses with greater pressures and cycles cause irreversible sonoporation and increase cell death.

5.4.3.2 Time to Peak

To further investigate the mechanism involved, we examined the time the signal took to peak between treatments (See Figure 40). Interestingly, there was no change in the "time to peak" readout between all treatments (except the 300kPa 10 cycles pulse, in which the signal analysis was affected by noise, see 5.4.2.3). Even more, the average time to peak of all tests is 22 seconds, closely matching the time constant (20 seconds [66]) of the closing membrane pores. This suggests a common release mechanism between all pulses.

5.4.3.3 ATP Release Speed

We showed that ATP released changes with cell death. Also, the time to peak remained constant throughout. If ATP released speed is linked to both the time to peak and to ATP released, it is logical to conclude that the ATP release speed would share the ATP released pattern. In fact, Figure 43 shows exactly that. With lower energy pulses, ATP release speed increases sharply with cell death, while at higher energy ones, the increase is reduced.

5.4.3.4 Conclusion

We have successfully quantified the ATP released after US and MB therapy and have linked this release to cell death. The time to peak analysis points towards a common mechanism of release between pulses and matches quite closely the literature reports of pore resealing kinetics. These holes in the membrane can either reseal or not depending on their size. Total ATP release results suggest that higher energy pulses create larger pores that don't reseal and cause cell death, while lower energy pulses create small pores that close up after treatment. However further research is needed to observe a link between ATP release to pore sizes.

5.5 **Flowing Viability Tests**

The current setup uses wide square cross-sectional channels of 700 µm in width. The larger width was very useful for cell culture, it was wide enough for cells to attach and create a monolayer with enough nutrients. However, achieving in vivo flows or shear stresses, are not feasible with the current setup. The dimensions of our channel, at 700 µm, represent large arterioles. These have average blood flow speeds of around 1 cm/ s and to achieve these speeds in our set-up we would have to pump liquid at 4000 µL/s, consuming very high amounts of reagents. In comparison, we used flow rates of 200 µL/min which is 1200 times lower. Because of the large dimension, bubbles at the wall also travel very slowly. This means that bubble replenishment after an US pulse takes a long time. With an input flow rate of 200 µL/min, it takes 1 minute for the bubbles to travel 3.2mm and replenish the treated area. We did have a successful sonoporation of HUVEC cells with flowing microbubbles. But have failed to replicate the effect on the cancer cell line. The chip shows potential for flowing MB sonoporation events, however, adjustments have to be taken before any scientific study can be made. As previously discussed, a more reliable bubble concentration across all channels would be ideal. For example, smaller channels that can still support cell growth exist and could be used in this project [106]. Focusing on growing and culturing endothelial cells inside the system would also be ideal.

As mentioned before, the initial input conditions of the flowing microbubbles can affect the distribution of bubbles. Under the current setup, all of the chips are checked for air bubbles or any disturbances that can affect the bubble distribution before moving on with the experiment.

However, there is no live view of the microbubbles when insonated. Moving to a setup where we can send an US pulse and see the bubbles at the same time would ideally make experiments more repeatable and can directly link the sonoporation event to any of the cellular activity we would like to image.

Currently, we only achieved a multiple pulse test once, on HUVEC cells. The repeatability of this test has been called into question as the test was done using an old design of the chip that didn't ensure reproducible results. As mentioned before there are newer designs that will have higher and quantifiable reproducibility.

Chapter 6 Conclusion

The goal for this master's project stemmed from the desire to improve provascular US and MB therapeutic pulses before radiotherapy. To that end, we designed a system that allows testing of multiple parameters to better understand the cells physiological response. In this microfluidic platform, resonating MB in an US pressure pulse can interact with cells and their response can be quantified. This leads to the two main goals of the project. First, to assess a key signaling molecule in the provascular response, ATP, and how its released after US and MB therapeutic pulses. Second to create a multiplexed environment were multiple parameters can be tested and quantified.

We have succeeded at the first goal by creating cell monolayers inside a PDMS microfluidic channels and having them interact with US and MB. We have quantified the release of ATP after treatment and have found that the mechanism of release depends on the cavitation energy of the treatment conditions. We succeeded at the second goal of the project by creating a platform where flowing MBs can be mixed and diluted into four parallel channels each with its own MB concentration. We could quantify the size, concentration, and speed of the bubbles to ensure repeatable results.

Finally, the results from this master's thesis will help develop better therapeutic pulses to treat tumours before radiotherapy.

6.1 Future work

In this work, we developed tools to study bubble to cell interactions. In particular, we quantified the kinetics of ATP release using bioluminescence imaging inside the microfluidic chip. There is still much work to be done to fully characterize ATP release with flowing microbubbles and multiple US pulses. This will allow us to test the effects of replenishing bubbles and to better mimic in vivo conditions. We have been able to culture endothelial cells in our current setup, but with a smaller sized channel to achieve a faster bubble replenishment and mimic smaller arterioles, we can achieve more meaningful in vitro results. It has been shown that achieving this

is possible[76], [106]. It would take some design changes and perfection experiments to obtain a fully endothelialized microfluidic system with different flowing microbubble concentrations.

Fluorescent images have been taken inside the chip and many other physiological reactions happen when cells are sonoporated. For example, calcium and NO can be imaged using fluorescent markers. The lab has had some preliminary experiments in the production of NO in HUVEC cells with promising results (See Annexe B). A link between the NO production in cells and ATP could lead to major advancements in the study of vasodilation after US and MB therapy.

Bibliography

[1] Canadian Cancer Society, "Cancer statistics at a glance." [Online]. Available: https://www.cancer.ca/en/cancer-information/cancer-101/cancer-statistics-at-a-glance/?region=on#:~:text=Cancer is the leading cause,women will die from cancer. [Accessed: 16-Nov-2020].

[2] A. M. Seaman, "U.S. cancer survival rates improving," *Reuters Health*, 2015. [Online]. Available: https://ca.reuters.com/article/idUSKBN0NE2KD20150423.

[3] "Understanding Radiation Therapy," 2020. [Online]. Available: https://www.cancer.net/navigating-cancer-care/how-cancer-treated/radiation-therapy/understanding-radiation-therapy. [Accessed: 13-Nov-2020].

[4] L. Harrison and K. Blackwell, "Hypoxia and anemia: factors in decreased sensitivity to radiation therapy and chemotherapy?," *Oncologist*, vol. 9, no. suppl_ 5, pp. 31–40, 2004.

[5] K. Graham and E. Unger, "Overcoming tumor hypoxia as a barrier to radiotherapy, chemotherapy and immunotherapy in cancer treatment," *Int. J. Nanomedicine*, vol. 13, pp. 6049–6058, Oct. 2018.

[6] J. T. Belcik *et al.*, "Augmentation of limb perfusion and reversal of tissue ischemia produced by ultrasound-mediated microbubble cavitation," *Circ. Cardiovasc. Imaging*, vol. 8, no. 4, p. e002979, 2015.

[7] V. Chan and A. Perlas, "Basics of ultrasound imaging," in *Atlas of ultrasound-guided procedures in interventional pain management*, Springer, 2011, pp. 13–19.

[8] O. I. Resources, "Ultrasonic Transducer Technical Notes." [Online]. Available: https://www.olympus-ims.com/en/resources/white-papers/ultrasonic-transducer-technical-notes/.

[9] J. E. Aldrich, "Basic physics of ultrasound imaging," *Crit. Care Med.*, vol. 35, no. 5, pp. S131–S137, 2007.

[10] "The Law of Refraction." [Online]. Available: https://www.math.ubc.ca/~cass/courses/m309-01a/chu/Fundamentals/snell.htm.

[11] M. L. Oelze, J. F. Zachary, and W. D. O'Brien Jr, "Characterization of tissue microstructure using ultrasonic backscatter: Theory and technique for optimization using a Gaussian form factor," *J. Acoust. Soc. Am.*, vol. 112, no. 3, pp. 1202–1211, 2002.

[12] E. Franceschini, F. T. H. Yu, F. Destrempes, and G. Cloutier, "Ultrasound characterization of red blood cell aggregation with intervening attenuating tissue-mimicking phantoms," *J. Acoust. Soc. Am.*, vol. 127, no. 2, pp. 1104–1115, Feb. 2010.

[13] R. J. Lavarello, W. R. Ridgway, S. S. Sarwate, and M. L. Oelze, “Characterization of thyroid cancer in mouse models using high-frequency quantitative ultrasound techniques,” *Ultrasound Med. Biol.*, vol. 39, no. 12, pp. 2333–2341, Dec. 2013.

[14] S. Hughes, “Medical ultrasound imaging,” *Phys. Educ.*, vol. 36, no. 6, p. 468, 2001.

[15] H. Hasegawa, “Very high frame rate ultrasound for medical diagnostic imaging,” in *AIP Conference Proceedings*, 2019, vol. 2173, no. 1, p. 20015.

[16] J. Foiret, H. Zhang, T. Ilovitsh, L. Mahakian, S. Tam, and K. W. Ferrara, “Ultrasound localization microscopy to image and assess microvasculature in a rat kidney,” *Sci. Rep.*, vol. 7, no. 1, pp. 1–12, 2017.

[17] S. R. Wilson and P. N. Burns, “Microbubble-enhanced US in body imaging: what role?,” *Radiology*, vol. 257, no. 1, pp. 24–39, 2010.

[18] P. A. Dijkmans *et al.*, “Quantification of myocardial perfusion using intravenous myocardial contrast echocardiography in healthy volunteers: comparison with positron emission tomography,” *J. Am. Soc. Echocardiogr.*, vol. 19, no. 3, pp. 285–293, 2006.

[19] E. Quaia, “Physical basis and principles of action of microbubble-based contrast agents,” in *Contrast media in ultrasonography*, Springer, 2005, pp. 15–30.

[20] K. Ferrara, R. Pollard, and M. Borden, “Ultrasound microbubble contrast agents: fundamentals and application to gene and drug delivery,” *Annu. Rev. Biomed. Eng.*, vol. 9, pp. 415–447, 2007.

[21] I. Lentacker, I. De Cock, R. Deckers, S. C. De Smedt, and C. T. W. Moonen, “Understanding ultrasound induced sonoporation: definitions and underlying mechanisms,” *Adv. Drug Deliv. Rev.*, vol. 72, pp. 49–64, 2014.

[22] E. VanBavel, “Effects of shear stress on endothelial cells: Possible relevance for ultrasound applications,” *Prog. Biophys. Mol. Biol.*, vol. 93, no. 1, pp. 374–383, 2007.

[23] P. F. Davies, “Flow-mediated endothelial mechanotransduction,” *Physiol. Rev.*, vol. 75, no. 3, pp. 519–560, Jul. 1995.

[24] A. Alonso *et al.*, “Reorganization of gap junctions after focused ultrasound blood–brain barrier opening in the rat brain,” *J. Cereb. Blood Flow Metab.*, vol. 30, no. 7, pp. 1394–1402, 2010.

[25] I. Beekers *et al.*, “Opening of endothelial cell–cell contacts due to sonoporation,” *J. Control. Release*, 2020.

[26] B. D. M. Meijering *et al.*, “Ultrasound and microbubble-targeted delivery of macromolecules is regulated by induction of endocytosis and pore formation,” *Circ. Res.*, vol. 104, no. 5, pp. 679–687, 2009.

[27] E. Beguin, S. Shrivastava, N. V Dezhkunov, A. P. McHale, J. F. Callan, and E. Stride, “Direct evidence of

multibubble sonoluminescence using therapeutic ultrasound and microbubbles," *ACS Appl. Mater. Interfaces*, vol. 11, no. 22, pp. 19913–19919, 2019.

[28] D. E. Goertz, "An overview of the influence of therapeutic ultrasound exposures on the vasculature: high intensity ultrasound and microbubble-mediated bioeffects," *Int. J. Hyperth.*, vol. 31, no. 2, pp. 134–144, 2015.

[29] C. Jia, L. Xu, T. Han, P. Cai, C. H. Alfred, and P. Qin, "Generation of reactive oxygen species in heterogeneously sonoporated cells by microbubbles with single-pulse ultrasound," *Ultrasound Med. Biol.*, vol. 44, no. 5, pp. 1074–1085, 2018.

[30] I. Beekers *et al.*, "High-Resolution Imaging of Intracellular Calcium Fluctuations Caused by Oscillating Microbubbles," *Ultrasound Med. Biol.*, 2020.

[31] J. T. Belcik *et al.*, "Augmentation of muscle blood flow by ultrasound cavitation is mediated by ATP and purinergic signaling," *Circulation*, vol. 135, no. 13, pp. 1240–1252, 2017.

[32] F. Moccetti *et al.*, "Flow Augmentation in the Myocardium by Ultrasound Cavitation of Microbubbles: Role of Shear-Mediated Purinergic Signaling," *J. Am. Soc. Echocardiogr.*, vol. 33, no. 8, pp. 1023-1031.e2, 2020.

[33] N. McDannold, C. D. Arvanitis, N. Vykhodtseva, and M. S. Livingstone, "Temporary disruption of the blood–brain barrier by use of ultrasound and microbubbles: safety and efficacy evaluation in rhesus macaques," *Cancer Res.*, vol. 72, no. 14, pp. 3652–3663, 2012.

[34] J. P. Christiansen, B. A. French, A. L. Klibanov, S. Kaul, and J. R. Lindner, "Targeted tissue transfection with ultrasound destruction of plasmid-bearing cationic microbubbles.," *Ultrasound Med. Biol.*, vol. 29, no. 12, pp. 1759–1767, Dec. 2003.

[35] S. Chen *et al.*, "Efficient gene delivery to pancreatic islets with ultrasonic microbubble destruction technology," *Proc. Natl. Acad. Sci.*, vol. 103, no. 22, pp. 8469–8474, 2006.

[36] N. G. Lee *et al.*, "Sonoporation enhances chemotherapeutic efficacy in retinoblastoma cells in vitro," *Invest. Ophthalmol. Vis. Sci.*, vol. 52, no. 6, pp. 3868–3873, 2011.

[37] A. Van Wamel *et al.*, "Vibrating microbubbles poking individual cells: drug transfer into cells via sonoporation," *J. Control. release*, vol. 112, no. 2, pp. 149–155, 2006.

[38] G. Dimcevski *et al.*, "A human clinical trial using ultrasound and microbubbles to enhance gemcitabine treatment of inoperable pancreatic cancer," *J. Control. Release*, vol. 243, pp. 172–181, 2016.

[39] P. Prentice, A. Cuschieri, K. Dholakia, M. Prausnitz, and P. Campbell, "Membrane disruption by optically controlled microbubble cavitation," *Nat. Phys.*, vol. 1, no. 2, pp. 107–110, 2005.

[40] R. B. McDonald, "Thermoregulation: Autonomic, Age-Related Changes," L. R. B. T.-E. of N. Squire, Ed. Oxford:

Academic Press, 2009, pp. 977–986.

[41] N. Charkoudian, “Skin blood flow in adult human thermoregulation: how it works, when it does not, and why.,” *Mayo Clin. Proc.*, vol. 78, no. 5, pp. 603–612, May 2003.

[42] N. Charkoudian, “Mechanisms and modifiers of reflex induced cutaneous vasodilation and vasoconstriction in humans,” *J. Appl. Physiol.*, vol. 109, no. 4, pp. 1221–1228, Oct. 2010.

[43] Y. Hellsten, M. Nyberg, L. G. Jensen, and S. P. Mortensen, “Vasodilator interactions in skeletal muscle blood flow regulation,” *J. Physiol.*, vol. 590, no. 24, pp. 6297–6305, Dec. 2012.

[44] P. Bagher and S. S. Segal, “Regulation of blood flow in the microcirculation: role of conducted vasodilation,” *Acta Physiol. (Oxf).*, vol. 202, no. 3, pp. 271–284, Jul. 2011.

[45] B. J. Krause, M. A. Hanson, and P. Casanello, “Role of nitric oxide in placental vascular development and function,” *Placenta*, vol. 32, no. 11, pp. 797–805, 2011.

[46] D. L. Kellogg, Y. Liu, I. F. Kosiba, and D. O’Donnell, “Role of nitric oxide in the vascular effects of local warming of the skin in humans,” *J. Appl. Physiol.*, vol. 86, no. 4, pp. 1185–1190, Apr. 1999.

[47] R. Boushel, “Metabolic control of muscle blood flow during exercise in humans,” *Can. J. Appl. Physiol.*, vol. 28, no. 5, pp. 754–773, 2003.

[48] C. A. Gruetter, B. K. Barry, D. B. McNamara, D. Y. Gruetter, P. J. Kadowitz, and L. Ignarro, “Relaxation of bovine coronary artery and activation of coronary arterial guanylate cyclase by nitric oxide, nitroprusside and a carcinogenic nitrosoamine.,” *J. Cyclic Nucleotide Res.*, vol. 5, no. 3, p. 211, 1979.

[49] A. Andrews, D. Buerk, and K. Barbee, “Shear Stress-Induced NO Production is Dependent on ATP Autocrine Signaling and Capacitative Calcium Entry,” *Cell. Mol. Bioeng.*, vol. 7, pp. 510–520, Dec. 2014.

[50] H. WESSELLS *et al.*, “Fluid shear stress-induced nitric oxide production in human cavernosal endothelial cells: inhibition by hyperglycaemia,” *BJU Int.*, vol. 97, no. 5, pp. 1047–1052, May 2006.

[51] A. M. Andrews, D. Jaron, D. G. Buerk, P. L. Kirby, and K. A. Barbee, “Direct, real-time measurement of shear stress-induced nitric oxide produced from endothelial cells in vitro,” *Nitric oxide Biol. Chem.*, vol. 23, no. 4, pp. 335–342, Dec. 2010.

[52] M. Noris *et al.*, “Nitric oxide synthesis by cultured endothelial cells is modulated by flow conditions,” *Circ. Res.*, vol. 76, no. 4, pp. 536–543, 1995.

[53] P. Bodin and G. Burnstock, “Evidence That Release of Adenosine Triphosphate From Endothelial Cells During Increased Shear Stress Is Vesicular,” *J. Cardiovasc. Pharmacol.*, vol. 38, no. 6, 2001.

[54] A. M. Forsyth, J. Wan, P. D. Owrutsky, M. Abkarian, and H. A. Stone, “Multiscale approach to link red blood cell dynamics, shear viscosity, and ATP release,” *Proc. Natl. Acad. Sci.*, vol. 108, no. 27, pp. 10986–10991, 2011.

[55] S. P. Mortensen, J. González-Alonso, L. T. Bune, B. Saltin, H. Pilegaard, and Y. Hellsten, “ATP-induced vasodilation and purinergic receptors in the human leg: roles of nitric oxide, prostaglandins, and adenosine,” *Am. J. Physiol. Integr. Comp. Physiol.*, vol. 296, no. 4, pp. R1140–R1148, Apr. 2009.

[56] A. R. Crecelius *et al.*, “Mechanisms of ATP-mediated vasodilation in humans: modest role for nitric oxide and vasodilating prostaglandins,” *Am. J. Physiol. Circ. Physiol.*, vol. 301, no. 4, pp. H1302–H1310, Jul. 2011.

[57] F. T. H. Yu, X. Chen, A. C. Straub, and J. J. Pacella, “The Role of Nitric Oxide during Sonoreperfusion of Microvascular Obstruction,” *Theranostics*, vol. 7, no. 14, p. 3527, 2017.

[58] C. M. Anderson, J. P. Bergher, and R. A. Swanson, “ATP-induced ATP release from astrocytes,” *J. Neurochem.*, vol. 88, no. 1, pp. 246–256, 2004.

[59] S. Locovei, J. Wang, and G. Dahl, “Activation of pannexin 1 channels by ATP through P2Y receptors and by cytoplasmic calcium,” *FEBS Lett.*, vol. 580, no. 1, pp. 239–244, 2006.

[60] M. Zhang, N. A. Piskuric, C. Vollmer, and C. A. Nurse, “P2Y2 receptor activation opens pannexin-1 channels in rat carotid body type II cells: potential role in amplifying the neurotransmitter ATP,” *J. Physiol.*, vol. 590, no. 17, pp. 4335–4350, 2012.

[61] F. Qiu and G. Dahl, “A permeant regulating its permeation pore: inhibition of pannexin 1 channels by ATP,” *Am. J. Physiol. Physiol.*, 2009.

[62] G. Dahl, F. Qiu, and J. Wang, “The bizarre pharmacology of the ATP release channel pannexin1,” *Neuropharmacology*, vol. 75, pp. 583–593, 2013.

[63] C. D’hondt *et al.*, “Pannexin channels in ATP release and beyond: an unexpected rendezvous at the endoplasmic reticulum,” *Cell. Signal.*, vol. 23, no. 2, pp. 305–316, 2011.

[64] J. Wu, J. P. Ross, and J.-F. Chiu, “Reparable sonoporation generated by microstreaming,” *J. Acoust. Soc. Am.*, vol. 111, no. 3, pp. 1460–1464, 2002.

[65] J. Wu and W. L. Nyborg, “Ultrasound, cavitation bubbles and their interaction with cells,” *Adv. Drug Deliv. Rev.*, vol. 60, no. 10, pp. 1103–1116, 2008.

[66] Y. Hu, J. M. F. Wan, and A. C. H. Yu, “Membrane Perforation and Recovery Dynamics in Microbubble-Mediated Sonoporation,” *Ultrasound Med. Biol.*, vol. 39, no. 12, pp. 2393–2405, 2013.

[67] A. Zeghimi, J.-M. Escoffre, and A. Bouakaz, “Role of endocytosis in sonoporation-mediated membrane

permeabilization and uptake of small molecules: a electron microscopy study," *Phys. Biol.*, vol. 12, no. 6, p. 66007, 2015.

[68] F. Yang *et al.*, "Experimental study on cell self-sealing during sonoporation," *J. Control. Release*, vol. 131, no. 3, pp. 205–210, 2008.

[69] N. Kudo, K. Okada, and K. Yamamoto, "Sonoporation by single-shot pulsed ultrasound with microbubbles adjacent to cells," *Biophys. J.*, vol. 96, no. 12, pp. 4866–4876, 2009.

[70] Z. Fan, H. Liu, M. Mayer, and C. X. Deng, "Spatiotemporally controlled single cell sonoporation," *Proc. Natl. Acad. Sci.*, vol. 109, no. 41, pp. 16486–16491, 2012.

[71] B. Helfield, X. Chen, S. C. Watkins, and F. S. Villanueva, "Biophysical insight into mechanisms of sonoporation," *Proc. Natl. Acad. Sci.*, vol. 113, no. 36, pp. 9983–9988, 2016.

[72] K. Kooiman, M. Foppen-Harteveld, A. F. W. van der Steen, and N. de Jong, "Sonoporation of endothelial cells by vibrating targeted microbubbles," *J. Control. Release*, vol. 154, no. 1, pp. 35–41, 2011.

[73] I. Skachkov, Y. Luan, A. F. W. van der Steen, N. de Jong, and K. Kooiman, "Targeted microbubble mediated sonoporation of endothelial cells in vivo," *IEEE Trans. Ultrason. Ferroelectr. Freq. Control*, vol. 61, no. 10, pp. 1661–1667, 2014.

[74] I. De Cock *et al.*, "Ultrasound and microbubble mediated drug delivery: acoustic pressure as determinant for uptake via membrane pores or endocytosis," *J. Control. release*, vol. 197, pp. 20–28, 2015.

[75] T. van Rooij *et al.*, "Viability of endothelial cells after ultrasound-mediated sonoporation: Influence of targeting, oscillation, and displacement of microbubbles," *J. Control. Release*, vol. 238, pp. 197–211, 2016.

[76] R. G. Li, "Engineering a vascular model based on microfluidics for studying microbubbles in an acoustic field." NTNU, 2018.

[77] M. J. Berridge, M. D. Bootman, and H. L. Roderick, "Calcium signalling: dynamics, homeostasis and remodelling," *Nat. Rev. Mol. cell Biol.*, vol. 4, no. 7, pp. 517–529, 2003.

[78] I. Fleming, J. Bauersachs, and R. Busse, "Calcium-dependent and calcium-independent activation of the endothelial NO synthase.," *J. Vasc. Res.*, vol. 34, no. 3, pp. 165–174, 1997.

[79] S. L. Sandow, S. Senadheera, T. H. Grayson, D. G. Welsh, and T. V Murphy, "Calcium and endothelium-mediated vasodilator signaling," in *Calcium Signaling*, Springer, 2012, pp. 811–831.

[80] J. Park, Z. Fan, and C. X. Deng, "Effects of shear stress cultivation on cell membrane disruption and intracellular calcium concentration in sonoporation of endothelial cells," *J. Biomech.*, vol. 44, no. 1, pp. 164–169, 2011.

[81] S. M. Nejad, S. H. R. Hosseini, H. Akiyama, and K. Tachibana, “Optical observation of cell sonoporation with low intensity ultrasound,” *Biochem. Biophys. Res. Commun.*, vol. 413, no. 2, pp. 218–223, 2011.

[82] D. M. B. de Paula, V. B. Valero-Lapchik, E. J. Paredes-Gamero, and S. W. Han, “Therapeutic ultrasound promotes plasmid DNA uptake by clathrin-mediated endocytosis,” *J. Gene Med.*, vol. 13, no. 7–8, pp. 392–401, 2011.

[83] J. K. Tung, K. Berglund, C.-A. Gutekunst, U. Hochgeschwender, and R. E. Gross, “Bioluminescence imaging in live cells and animals,” *Neurophotonics*, vol. 3, no. 2, p. 25001, Apr. 2016.

[84] “ATP MEASUREMENT.” [Online]. Available: https://www.berthold.com/en/bioanalytic/knowledge/glossary/atp-measurement/. [Accessed: 17-Nov-2020].

[85] J. J. Tan, O. Ponomarchuk, R. Grygorczyk, and F. Boudreault, “Wide field of view quantitative imaging of cellular ATP release,” *Am. J. Physiol. Physiol.*, vol. 317, no. 3, pp. C566–C575, 2019.

[86] E. K. Sackmann, A. L. Fulton, and D. J. Beebe, “The present and future role of microfluidics in biomedical research,” *Nature*, vol. 507, no. 7491, pp. 181–189, 2014.

[87] M. Astolfi *et al.*, “Micro-dissected tumor tissues on chip: an ex vivo method for drug testing and personalized therapy,” *Lab Chip*, vol. 16, no. 2, pp. 312–325, 2016.

[88] T. Das *et al.*, “Empirical chemosensitivity testing in a spheroid model of ovarian cancer using a microfluidics-based multiplex platform,” *Biomicrofluidics*, vol. 7, no. 1, p. 11805, Jan. 2013.

[89] H. Bruus, “Governing equations in microfluidics,” 2014.

[90] R. F. Ismagilov *et al.*, “Pressure-driven laminar flow in tangential microchannels: an elastomeric microfluidic switch,” *Anal. Chem.*, vol. 73, no. 19, pp. 4682–4687, 2001.

[91] H. Bruus, *Theoretical microfluidics*, vol. 18. Oxford university press Oxford, 2008.

[92] T. M. Squires and S. R. Quake, “Microfluidics: Fluid physics at the nanoliter scale,” *Rev. Mod. Phys.*, vol. 77, no. 3, p. 977, 2005.

[93] D. Ahmed, X. Mao, B. K. Juluri, and T. J. Huang, “A fast microfluidic mixer based on acoustically driven sidewall-trapped microbubbles,” *Microfluid. Nanofluidics*, vol. 7, no. 5, p. 727, 2009.

[94] B. Xu, T. N. Wong, N.-T. Nguyen, Z. Che, and J. C. K. Chai, “Thermal mixing of two miscible fluids in a T-shaped microchannel,” *Biomicrofluidics*, vol. 4, no. 4, p. 44102, 2010.

[95] Y. Wang, J. Zhe, B. T. F. Chung, and P. Dutta, “A rapid magnetic particle driven micromixer,” *Microfluid.*

Nanofluidics, vol. 4, no. 5, pp. 375–389, 2008.

[96] C.-Y. Lee, C.-L. Chang, Y.-N. Wang, and L.-M. Fu, "Microfluidic mixing: a review," *Int. J. Mol. Sci.*, vol. 12, no. 5, pp. 3263–3287, 2011.

[97] Z. Chen *et al.*, "Performance analysis of a folding flow micromixer," *Microfluid. Nanofluidics*, vol. 6, no. 6, pp. 763–774, 2009.

[98] P. E. Neerincx, R. P. J. Denteneer, S. Peelen, and H. E. H. Meijer, "Compact mixing using multiple splitting, stretching, and recombining flows," *Macromol. Mater. Eng.*, vol. 296, no. 3-4, pp. 349–361, 2011.

[99] C.-C. Hong, J.-W. Choi, and C. H. Ahn, "A novel in-plane passive microfluidic mixer with modified Tesla structures," *Lab Chip*, vol. 4, no. 2, pp. 109–113, 2004.

[100] A. Bertsch, S. Heimgartner, P. Cousseau, and P. Renaud, "Static micromixers based on large-scale industrial mixer geometry," *Lab Chip*, vol. 1, no. 1, pp. 56–60, 2001.

[101] A. D. Stroock, S. K. W. Dertinger, A. Ajdari, I. Mezić, H. A. Stone, and G. M. Whitesides, "Chaotic mixer for microchannels," *Science (80-.).*, vol. 295, no. 5555, pp. 647–651, 2002.

[102] C.-Y. Lee, W.-T. Wang, C.-C. Liu, and L.-M. Fu, "Passive mixers in microfluidic systems: A review," *Chem. Eng. J.*, vol. 288, pp. 146–160, 2016.

[103] A. Enders, I. G. Siller, K. Urmann, M. R. Hoffmann, and J. Bahnemann, "3D printed microfluidic mixers—a comparative study on mixing unit performances," *Small*, vol. 15, no. 2, p. 1804326, 2019.

[104] M. Zimmermann, H. Schmid, P. Hunziker, and E. Delamarche, "Capillary pumps for autonomous capillary systems," *Lab Chip*, vol. 7, no. 1, pp. 119–125, 2007.

[105] T. Wang *et al.*, "The design and characterization of a gravitational microfluidic platform for drug sensitivity assay in colorectal perfused tumoroid cultures," *Nanomedicine Nanotechnology, Biol. Med.*, p. 102294, 2020.

[106] E. K. Juang *et al.*, "Engineered 3D microvascular networks for the study of ultrasound-microbubble-mediated drug delivery," *Langmuir*, vol. 35, no. 31, pp. 10128–10138, 2018.

[107] G. Lajoinie *et al.*, "In vitro methods to study bubble-cell interactions: Fundamentals and therapeutic applications," *Biomicrofluidics*, vol. 10, no. 1, p. 11501, 2016.

[108] Z. G. Li, A. Q. Liu, E. Klaseboer, J. B. Zhang, and C. D. Ohl, "Single cell membrane poration by bubble-induced microjets in a microfluidic chip," *Lab Chip*, vol. 13, no. 6, pp. 1144–1150, 2013.

[109] C. L. Ling Yong *et al.*, "Microbubble-mediated sonoporation for highly efficient transfection of recalcitrant human B-cell lines," Wiley Online Library, 2014.

[110] C.-D. Ohl *et al.*, "Sonoporation from jetting cavitation bubbles," *Biophys. J.*, vol. 91, no. 11, pp. 4285–4295, 2006.

[111] V. Garbin *et al.*, "Changes in microbubble dynamics near a boundary revealed by combined optical micromanipulation and high-speed imaging," *Appl. Phys. Lett.*, vol. 90, no. 11, p. 114103, Mar. 2007.

[112] M. Overvelde, V. Garbin, B. Dollet, N. de Jong, D. Lohse, and M. Versluis, "Dynamics of Coated Microbubbles Adherent to a Wall," *Ultrasound Med. Biol.*, vol. 37, no. 9, pp. 1500–1508, Sep. 2011.

[113] Y. Zheng *et al.*, "In vitro microvessels for the study of angiogenesis and thrombosis," *Proc. Natl. Acad. Sci.*, vol. 109, no. 24, pp. 9342 LP – 9347, Jun. 2012.

[114] K. J. Regehr *et al.*, "Biological implications of polydimethylsiloxane-based microfluidic cell culture," *Lab Chip*, vol. 9, no. 15, pp. 2132–2139, 2009.

[115] J. Y. Park *et al.*, "Surface chemistry modification of PDMS elastomers with boiling water improves cellular adhesion," *Sensors Actuators B Chem.*, vol. 173, pp. 765–771, 2012.

[116] G. K. Toworfe, R. J. Composto, C. S. Adams, I. M. Shapiro, and P. Ducheyne, "Fibronectin adsorption on surface-activated poly (dimethylsiloxane) and its effect on cellular function," *J. Biomed. Mater. Res. Part A An Off. J. Soc. Biomater. Japanese Soc. Biomater. Aust. Soc. Biomater. Korean Soc. Biomater.*, vol. 71, no. 3, pp. 449–461, 2004.

[117] M. Klarhöfer, B. Csapo, C. Balassy, J. C. Szeles, and E. Moser, "High-resolution blood flow velocity measurements in the human finger," *Magn. Reson. Med. An Off. J. Int. Soc. Magn. Reson. Med.*, vol. 45, no. 4, pp. 716–719, 2001.

[118] C. E. Riva, J. E. Grunwald, S. H. Sinclair, and B. L. Petrig, "Blood velocity and volumetric flow rate in human retinal vessels.," *Invest. Ophthalmol. Vis. Sci.*, vol. 26, no. 8, pp. 1124–1132, 1985.

[119] M. P. Kok, T. Segers, and M. Versluis, "Bubble sorting in pinched microchannels for ultrasound contrast agent enrichment," *Lab Chip*, vol. 15, no. 18, pp. 3716–3722, 2015.

[120] S. R. Bazaz, A. A. Mehrizi, S. Ghorbani, S. Vasilescu, M. Asadnia, and M. E. Warkiani, "A hybrid micromixer with planar mixing units," *RSC Adv.*, vol. 8, no. 58, pp. 33103–33120, 2018.

[121] A. Cafarelli, A. Verbeni, A. Poliziani, P. Dario, A. Menciassi, and L. Ricotti, "Tuning acoustic and mechanical properties of materials for ultrasound phantoms and smart substrates for cell cultures," *Acta Biomater.*, vol. 49, pp. 368–378, 2017.

[122] J.-Y. Tinevez *et al.*, "TrackMate: An open and extensible platform for single-particle tracking," *Methods*, vol. 115, pp. 80–90, 2017.

[123] D. E. Goertz, N. de Jong, and A. F. W. van der Steen, “Attenuation and size distribution measurements of Definity™ and manipulated Definity™ populations,” *Ultrasound Med. Biol.*, vol. 33, no. 9, pp. 1376–1388, 2007.

[124] E. W. K. Young and D. J. Beebe, “Fundamentals of microfluidic cell culture in controlled microenvironments,” *Chem. Soc. Rev.*, vol. 39, no. 3, pp. 1036–1048, 2010.

[125] R. Karshafian, P. D. Bevan, R. Williams, S. Samac, and P. N. Burns, “Sonoporation by ultrasound-activated microbubble contrast agents: effect of acoustic exposure parameters on cell membrane permeability and cell viability,” *Ultrasound Med. Biol.*, vol. 35, no. 5, pp. 847–860, 2009.

[126] Y. Qiu *et al.*, “The correlation between acoustic cavitation and sonoporation involved in ultrasound-mediated DNA transfection with polyethylenimine (PEI) in vitro,” *J. Control. Release*, vol. 145, no. 1, pp. 40–48, 2010.

Annexes

Annexe A- IEEE IUS conference proceedings

A multiplexed microfluidic and microscopy study of vasodilation signaling pathways using microbubble and ultrasound therapy

Joseph Goldgewicht
Centre de recherche du CHUM
Université de Montréal
Montréal, Canada

Ju Jing Tan, PhD
Centre de recherche du CHUM
Université de Montréal
Montréal, Canada

Ryszard Grygorczyk, PhD
Centre de recherche du CHUM
Université de Montréal
Montréal, Canada
University of Montreal
Montreal, Canada

Thomas Gervais, PhD
École Polytechnique de Montréal
Montreal, Canada

François T. H. Yu, PhD
Centre de recherche du CHUM
Université de Montréal
Montréal, Canada

Abstract— Introduction: Oscillating microbubbles (MBs) in an ultrasound (US) pressure field can induce purinergic signaling (ATP) and vasodilation in muscle. We therefore envision that US+MB may be used to alter hypoxic tumor micro-environments to improve radiotherapy. Herein, we propose a multiplexed microfluidic platform that allows mixing of two separate flowing phases to examine the effects of MB and US on purinergic signaling in cultured cells. Methods: 4T1 cells were cultured in PDMS microfluidic chips. We investigated a range of different US pressures (200, 300 and 500 kPa) and cycles (10, 100, 1000) using single therapeutic US pulses at 1 MHz, in the presence of MB (1e7 MBs/mL). A bioluminescent imaging system (Evolve 512, Photometrics) and a luciferin/luciferase assay were used to quantify ATP release kinetics after treatment. Fluorescent microscopy was used to assess cell viability after US exposure via a propidium iodide and calcein AM assays. Results and conclusions: Our results show that we can quantify released ATP kinetics following US treatments. Released ATP ranged between 0.3 pmol to 2.74 pmol and the signal lasted for over 250 seconds. Results show that larger numbers of cycles and pressures both increased the amount of ATP released. Live/dead staining showed that cell death varied between (1.52% to 33.77%) depending on the US conditions.

Keywords—Theranostics, Microbubbles, Ultrasound, Microfluidics, ATP release

I. INTRODUCTION

It was previously shown that microbubble (MB) oscillations in an ultrasound (US) field can cause vasodilation in muscle [12] which we propose to leverage as a targeted provascular therapy approach to reduce hypoxia in solid tumors before radiotherapy. One key signaling pathway is ATP, which, when released in the extracellular space, can phosphorylate eNOS through the P2Y receptor. However, very little is known about ATP release kinetics following MB cell interactions. In this study, we used microfluidic chips to create cell coated flow channels mimicking in vivo bubble replenishment to study how different US and MB parameters (pressure, bubble concentration, and flow rate) affect ATP signaling following MB+US therapy. Our overall objective is to elucidate the time course, reservoir, and signaling pathways leading to ATP release.

II. METHODS

A. Abbreviations and Acronyms

US: Ultrasound
MB: Microbubble
ATP: Adenosine triphosphate
ROI: Region of interest
PDMS: Polydimethylsiloxane
PI: Propidium iodide

B. Microfluidic manufacturing

Moulds were 3D printed using an Asiga SLA printer, cleaned with isopropanol 5%, cured under a UV light for 5 min and sonicated in 70% ethanol for 5 min. Microfluidic chips were manufactured using Polydimethylsiloxane (PDMS) (Sylgard 184, Dow). PDMS was mixed at a 10:1 ratio of PMDS to curing agent, poured onto the moulds and degassed in a vacuum. The degassed PMDS in the moulds was then cured at 70°C for 90 min. The two halves of the chips were bonded together by exposing the faces to atmospheric plasma for 30s [3].

C. Cell culture

Before cell seeding, the microfluidic chips were sterilized and coated with fibronectin (Sigma Aldrich) at a concentration of 100 µg/mL for an hour. 4T1 cells were then seeded into the chips at a concentration 2,200 of cells/mm2. Chips were flipped upside down into a petri dish and

submerged in 2 mL of media (RPMI, 10% fetal bovine serum, 1% penicillin/streptomycin). Cells were incubated at 37°C and 5% CO2 until the cells were nearly confluent (typically 24h).

D. Experimental conditions

On the experimental day, the chip was flipped again and filled with microbubbles, allowing MB to float to be in contact with cells. Three different US pressures (200, 300 and 500 kPa) and three number of cycles (10, 100 and 1000 cycles) were tested using single US pulses, delivered using a single element US probe (1MHz, A303S, 0.5 Inch, Olympus) (Fig.1). Two experiments were performed: (1) with constant number of cycles (1000 cycles) and varying pressure; (2) with constant pressure (300 kPa) and varying the number of cycles. All experiments were performed with a fixed MB concentration of 1×10^7 MBs/mL. A bioluminescent imaging system (Evolve 512, Photometrics) and a Luciferin/Luciferase assay (FLAAM Sigma Aldrich, prepared as discussed in Tan el al [4]) were used to quantify ATP release after US treatment (Fig 1a) [4]. Every chip was first positioned using brightfield imaging, allowing to locate the US probe and the chip (Fig. 1b). ATP video sequences were taken at 2 seconds frame interval for 5 min. A fluorescent microscope (Widefield Olympus IX71) was used to perform a live/dead assay (Fig. 1c): Propidium iodide (PI, 25 µg/mL Thermo Fisher) and Calcein AM (4 µg/mL Thermo Fisher) were added 5 minutes after the experiment to assess cell viability after US exposure. Viability tests were performed on separate microfluidic chips.

E. Statistical analysis

The effect of pressure and cycles on both cell viability and ATP release were tested using one-way ANOVAs. Multiple comparisons testing (Tukey) were performed to identify differences in cell death and ATP release between treatment groups. All statistical tests were performed in MATLAB (v2019).

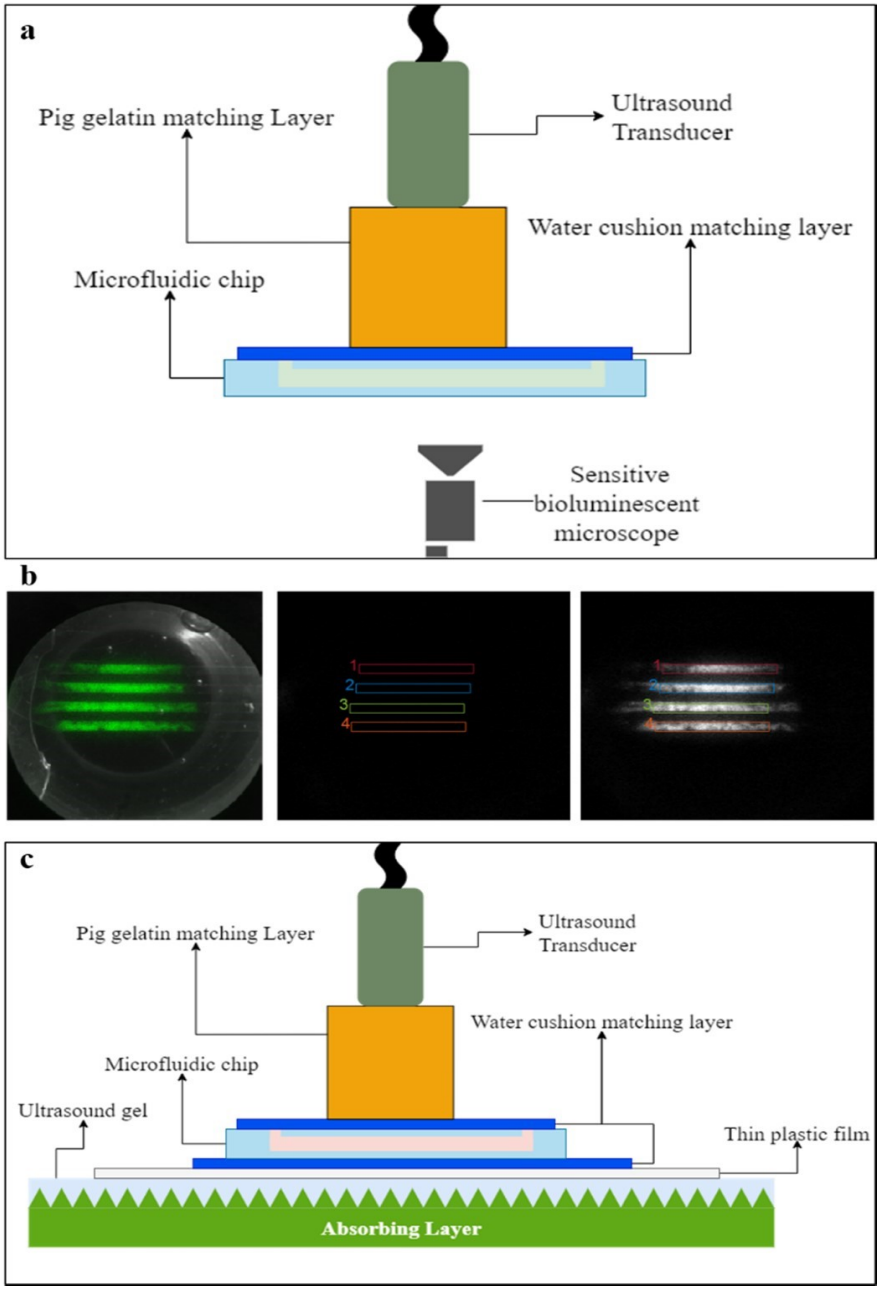

Fig 1. a) ATP bioluminescence imaging schematic: the ultrasound probe was positioned above the microfluidic chip and imaged by a sensitive bioluminescent microscope; b) Typical images, showing the microfluidic chip positioned in front of the ultrasound probe and the four parallel channels and regions of interest before and after treatment; c) Schematic of the cell viability test setup: the ultrasound probe was positioned above the microfluidic chip positioned on an absorbing layer.

III. IMAGE PROCESSING

A. ATP release

ATP image sequences were analysed using a custom MATLAB script. Four rectangular ROIs of equal area were drawn in flow channels subjected to US, seen in Fig. 1b. To obtain the amount of ATP in each frame, noise was first subtracted from the image. Then the signal was integrated over the ROI and multiplied by a calibration factor determined in Tan et al. [4]. Total ATP release was calculated as the peak ATP signal minus the average pre-US value. The ATP release speed was calculated by fitting a linear regression to the ATP signal in the first 10 seconds after the US pulse. The slope of the linear regression was considered the ATP release speed.

B. Cell Viability

Cell viability images had two channels: a green channel marking live cells (Calcein AM) and a red marking dead cells (PI). All images were separated and thresholded using Otsu's method. Briefly, Otsu's method divides a grayscale image into two classes that minimizes interclass variance. The area fraction of both channels was used as an estimation the number of live and dead cells. Percent dead cells was calculated as the area fraction of the dead cells divided by the area of all cells (sum of dead and live cells). For one chip, each channel was imaged 5 times. The average of these 5 images was taken as the % dead cells for the channel.

IV. RESULTS

A. ATP release

Across all pulses, the ATP released varied between 0.03 pmol and 2.7 pmol. This is an equivalent ATP resealed amount by a strain of 5% to 9% [4]. ATP release speed varied between 0.00 pmol/sec and 0.24 pmol/sec. Both pressure and #cycles had an effect on ATP release (Fig. 2a) and ATP release speed (Fig. 2b) (all $p < 0.001$, one-way ANOVA). Upon multiple comparison testing, we found differences between the 300 kPa/1000 cycles and the 300 kPa/10 cycles pulses, and between the 300 kPa/100 cycles and 300 kPa/10 cycles pulses (all $p < 0.01$, Tukey). Similarly, we found a difference between the 500 kPa/100 cycles and 200 kPa/1000 cycles pulses, and between

the 300 kPa/1000 cycles and the 200 kPa/1000 cycles pulses (all $p < 0.01$, Tukey). ATP release speed was also different between 300 kPa/1000 cycles and the 500kPa 1000 cycles ($p < 0.05$, Tukey).

B. Cell Viability

Percent dead cells varied between 1.52% to 33.77% across all conditions seen in Fig. 2c. The #cycles and pressure both had an effect on % dead cells, (all $p < 0.001$, one-way ANOVA). At 300 kPa we found significant difference between the 1000 and the 100 cycles ($p < 0.05$, Tukey), the 1000 and 10 cycles ($p < 0.01$, Tukey), and the 1000 and the control ($p < 0.01$, Tukey). At 1000 cycles, we found differences between 500 kPa and the 200 kPa, the 500 kPa and the control, the 300 kPa and the 200 kPa, and the 300 kPa and the control (all $p < 0.01$, Tukey).

C. ATP and Cell death combined

ATP release and % dead cells are plotted against each other for all the tested pulses in Fig.3. We can identify to two regions in this graph: (1) a region with ATP release but low cell death, corresponding to lower energy pulses; (2) a region with a marked increase in ATP release but with a higher cell death, corresponding to higher energy pulses.

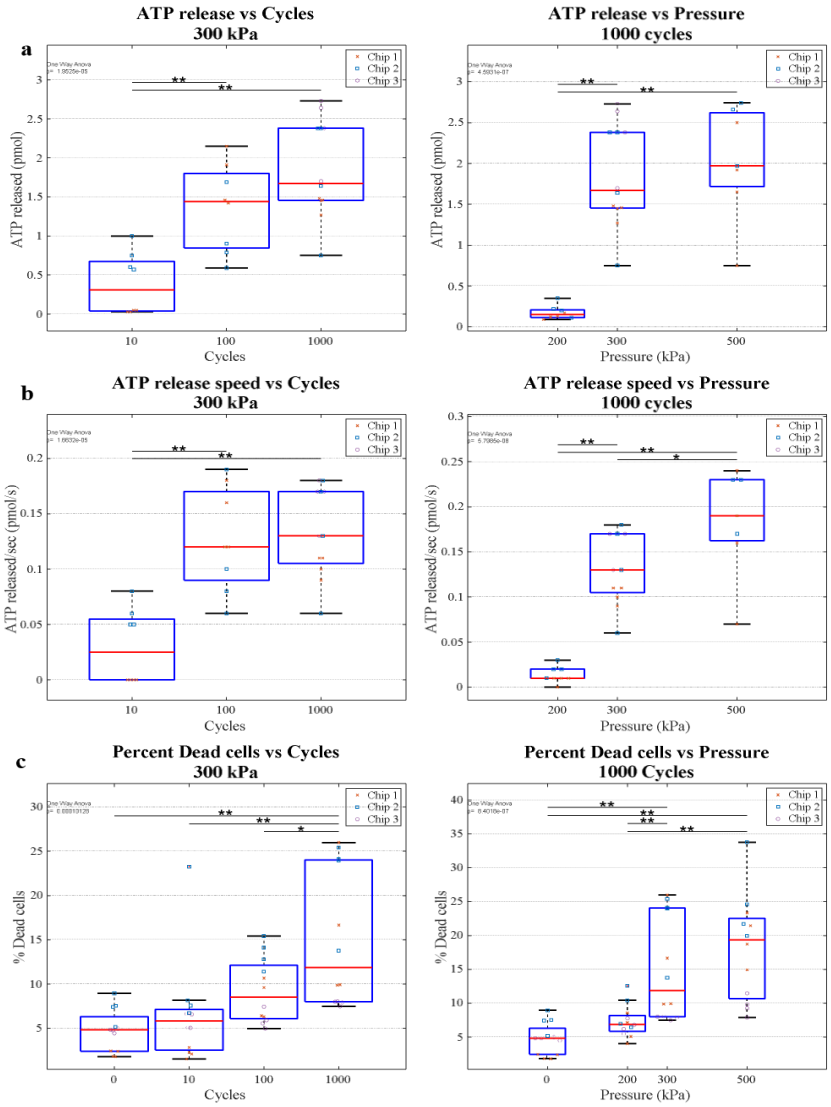

Fig 2. Box plots (median 25th and 75th percentile) of in vitro ATP release, release speed and % dead cells after MB+US therapy: a) ATP released, and b) ATP release speed plotted as a function of cycles and pressure (n = 8-12 channels). Each dot represents one channel. c) % dead cells plotted as a function of #cycles and pressure. (n = 12 channels). * $p < 0.05$, ** $p < 0.01$, *** $p < 0.001$ (Tukey Multiple comparisons test).

V. DISCUSSION AND CONCLUSION

Using an in vitro PDMS cell culture chip (compatible with flow and mixing of two phases to allow MB and drug titrations), we demonstrated that we can quantify the kinetics of ATP release

following MB+US therapy using single US bursts at 1 MHz. We found that there are conditions that allow ATP release without and with a concomitant increase in cell death.

One limitation of the study is that the MB in all tests were static. To mimic in vivo replenishment conditions flowing MBs are needed. Furthermore, the cell viability imaging was done after US therapy. This limits our understating of how sonoporation is related to observed ATP kinetics and cell viability. An experiment that follows both ATP release and PI uptake for example, would be necessary to understand what percentage of ATP release comes from sonoporation rather than cell death. Next steps include flowing MB experiments and multiple therapeutic pulses in the microfluidic chip, which can provide four different MB concentrations in one experiment. This in vitro approach will help further our understanding of MB cell interactions, including the effects on purinergic signaling, and guide the design of a therapeutic pulse to increase vascular perfusion in hypoxic tumors to sensitize them to radiotherapy.

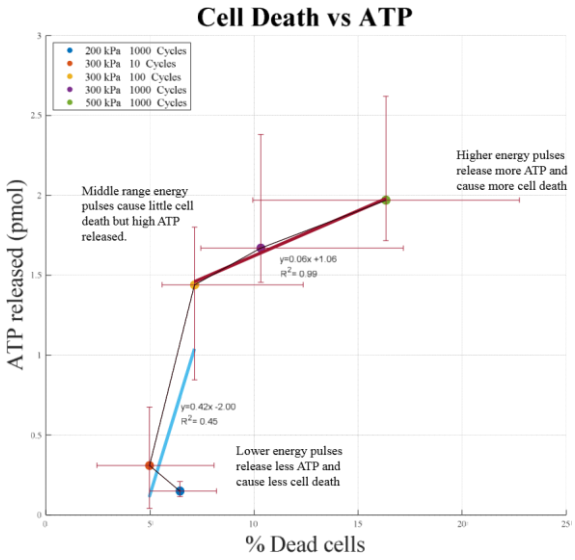

Fig 3. Relationship between ATP released and % dead cells. The median and the interquartile range are shown in dots and bars respectively. The blue and purple lines show the linear regression for the first three (low energy pulses) and last three pulses (high energy pulses), respectively

This work was funded by the Natural Sciences and Engineering Research Council of Canada (Discovery Grant # RGPIN-2018-04233) and the Fonds de recherche du Québec – Santé (# 265499)

REFERENCES

[1] F. T. H. Yu, X. Chen, A. C. Straub, and J. J. Pacella, “The Role of Nitric Oxide during Sonoreperfusion of Microvascular Obstruction,” Theranostics, vol. 7, no. 14, p. 3527, 2017.

[2] J. T. Belcik et al., “Augmentation of muscle blood flow by ultrasound cavitation is mediated by ATP and purinergic signaling,” Circulation, vol. 135, no. 13, pp. 1240–1252, 2017.

[3] A. St-Georges-Robillard et al., “Fluorescence hyperspectral imaging for live monitoring of multiple spheroids in microfluidic chips,” Analyst, vol. 143, no. 16, pp. 3829–3840, 2018.

[4] J. J. Tan, O. Ponomarchuk, R. Grygorczyk, and F. Boudreault, “Wide field of view quantitative imaging of cellular ATP release,” Am. J. Physiol. Physiol., vol. 317, no. 3, pp. C566–C575, 2019.

Annexe B- Rodin Chermat report.

Rodin Chermat was part of the MYL Yu lab for the summer and fall of 2019. His work was closely related to the topic of this thesis. The project focused on measuring increases in NO production in endothelial cells following US and MB treatment. The dye used, DAF-FM, increases in fluorescence once in contact with NO. After treatment with US and MB, the HUVEC cells were imaged in a fluorescent microscope. My contribution to this project was writing the custom ImageJ plugin to analyze the images in the following report. The following report was included in this thesis with his consent.

Fluorescence imaging of shear stress-induced nitric oxide release mediated by ultrasound-triggered microbubble cavitation in live tumor and endothelial cells

Rodin Chermat

Project supervisor: Prof. François Yu

Examiner: Prof. Thomas Gervais

Abstract

Nitric oxide (NO), a highly reactive free radical gas, is associated in mammalians to a variety of physiological and pathophysiological in both stromal and tumor cells. NO is synthesized from the conversion of L-arginine into L-citrulline, catalyzed by one of three NO synthases (NOS) depending on stimuli. Although tumor cells response to NO varies drastically depending on NO concentration, cell type and NOS implicated, recent studies showed shear-stress induced increase in NO acting as a radiosensitizer in tumor, as well as altering local hemodynamics thereby offering new strategies for better drug, gene or effector cell delivery. Interaction between gas microbubbles (MBs) and ultrasound (US) pulses has been showed to increase local shear-stress through MB cavitation, leading to increase in intracellular NO levels. Generally, NO production is quantified indirectly through nitrate colorimetry, NOS mRNA Western-Blot or NO-sensitive electrode, without providing real-time information on spatial distribution of NO synthesis. Thus, the goal of this project was to design a fluorescence-based imaging method of US-triggered MB-mediated shear-stress induced NO production in live endothelial and tumor cells. DAF-FM Da, a fluorescein-based green fluorescent intracellular NO probe was selected as our NO fluorescent probe and was first used to detect intracellular lipopolysaccharides (LPS)-induced and bradykinin-induced NO synthesis in 4T1 murine mammary tumor model and in human endothelial vein umbilical cells (HUVECs). Upon confirmation of proper functioning of L-arginine pathway in HUVECs, MB/US-mediated shear stress-induced NO production was imaged with DAFFM Da in order to shed light on the influence of ultrasound parameters and microbubble density on the shear-stress mediated increase of intracellular NO levels.

Introduction

Nitric oxide (NO) is a highly reactive free radical versatile gas, synthesized from the conversion of Larginine into L-citrulline by a family of enzymes called NO synthases (NOS), reaction requiring both NADPH and O2 as co-substrates (Figure 1). [1]-[6]

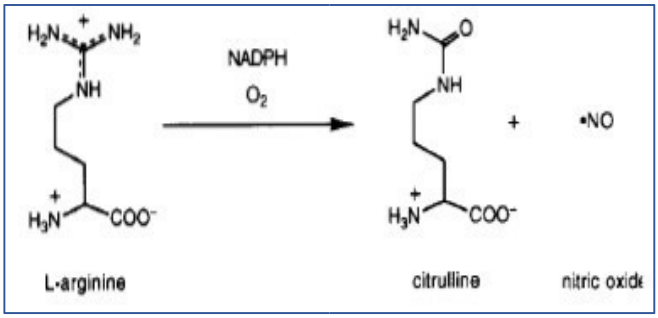

Figure 1: Mechanism of nitric oxide synthesis. NO is a byproduct of L-arginine conversion into L-citrulline in the presence of both NADPH and O2.

There are three isoforms of NOS: neuronal NOS (nNOS or NOS1), inducible NOS (iNOS or NOS2) and endothelial NOS (eNOS or NOS3). [7][2]

Both nNOS and eNOS are also referred to as constitutive NOS (cNOS), since they are respectively constitutively expressed predominantly in neuronal cells and vascular endothelial cells. On the other hand, iNOS is transcriptionally regulated, its transcription being induced by inflammatory cytokines, endotoxin, hypoxia and oxidative stress. [8] For example, stimuli for iNOS induction include products of Gram-negative and Gram-positive bacteria, interferon-y, interleukin-l, and tumor necrosis factors. [2] Activation of iNOS by lipopolysaccharides (LPS), a protein extracted from the membrane of Gram-negative bacteria, or by the vasodilator bradykinin has been widely documented as a stable positive control for NO production in a large panel of animal and human cell types. [9]-[21]

Although the term “inducible” has been restricted to iNOS, eNOS expression is also regulated by a variety of stimuli. For instance, fluid flow across the endothelium, commonly known as shear stress, upregulates eNOS expression. Shear stress-triggered NO release has been demonstrated

in vitro in both animal and human cells, using either classic culture setups or microfluidics devices. [22]–[26] Besides shear stress-responsive elements, it has been shown that the eNOS promotor also contains putative elements rendering it responsive to various transcription factors and proteins such as Sp1, GATA proteins, sterols, estrogens, nuclear factor 1, cAMP, and activator protein-1 (AP-1) and -2 (AP-2). [4]

Generally, iNOS activation results in the production of more NO than other NOS, and does so independently of intracellular Ca2+ levels, while cNOS activity crucially depends on cytosolic calcium (Ca2+) levels. Indeed, although all NOSs require bound calmodulin for activity, only iNOS has sufficiently high avidity for calmodulin to remain bound at low basal levels of calcium, thereby conferring iNOS full catalytic activity. [7] Thus, cNOS mainly produce small amounts of NO in response to transient elevations in intracellular calcium, while iNOS produces large fluxes of NO until substrates become limiting. iNOS is thus considered to be the isoform from which cytotoxic amounts of NO are produced, even though a sufficiently sustained increase in intracellular Ca2+ (for example in ischemial reperfusion) may cause cNOS to produce cytotoxic quantities of NO. [7]

NO is implicated in the regulation of a variety of physiological and/or pathophysiological processes, such as neurological functions (neurogenesis and neurotransmission), vascular functions (angiogenesis, vasodilation, vascular permeability, leukocyte–endothelial interaction, platelet aggregation and even microlymphatic flow), and even cytotoxic functions (cytostasis and cytolysis) at high concentrations. [2], [24], [27], [28]

Many of the cellular effects of NO are mediated by the NO–cGMP signaling pathway, although the contribution of post-translational protein modification, mainly through S-nitrosylation of cysteine thiol residues, is starting to gain attention. Cytotoxic and/or genotoxic effects, such as inhibition of mitochondrial respiration, protein and DNA damage resulting in gene mutation, loss of protein function, necrosis and apoptosis, are mediated either directly by NO or by NO metabolites such as nitrite, nitrate, S-nitrosothiols, nitrosamines and peroxynitrite. [7], [27]

The various physiological effects of NO, and notably its effects on tumor growth and progression, are not self-evident. NO effects highly vary depending on the type and activity of NOSs activated, but also on the type of cell receiving and/or producing NO, either stromal or tumor-like. [29]

Increased expression and higher NOS activity have been identified across multiple human cancer cell lines. Generally, tumor cells mainly express iNOS and only in some cases nNOS or eNOS, depending on tumor type and eventually on the stage of the tumor: for example, cancerous vascular endothelial cells predominantly express eNOS. [7]

In tumors, studies indicate the ubiquity of the effects of NO, showing that NO can both promote and/or inhibit tumor onset, progression and metastasis, depending on local concentration of NO, duration of exposure to NO, cell sensitivity and also depending on the activity and localization of NOS. [7] Indeed, Fukumura et al. showed that modulation of NO levels altered hemodynamics and microcirculatory behavior of murine mammary carcinoma but not of human colon adenocarcinoma, once again indicating the versatile aspect of NO in tumors. [29]

Interestingly, Jordan et al showed that NO can work as an additive complementary factor to oxygen in radiotherapy, since NO increases tumor oxygenation and has an intrinsic radiosensitizing potential.[30]

In responsive solid tumors, altering hemodynamics through the local modulation of NO levels could thus become a potential strategy to improve drug, gene vector or even effector cell delivery, as well as increasing local oxygen levels and radiation sensitivity.

If high intensity focalized ultrasound (HIFU) is already being used as a tissue ablation method in cancer treatment, treatment strategies based on the combined effects of microbubbles (MBs) and ultrasound (US) have been gaining interest in recent years and show promising results. [31] It is now established that US waves can induce controlled cavitation of MBs in vivo, resulting in a variety of physiological effects depending on the type and size of the bubbles as well as the parameters of the US pulse. Indeed, when placed in a driving pressure field, the surface of MBs exhibit non-spherical oscillations and volumetric oscillations, in conjunction with a radiation force phenomenon, conferring various properties allowing drug delivery, gene delivery, improved imaging contrast, and other clinical applications. [32]-[36]

Mainly, when US-mediated MB cavitation increases shear-stress beyond a threshold of a few kilopascals, a phenomenon of transient cell sonoporation synchronized with the US pulse is observed and drastically increases cellular membrane permeability. The value of this threshold

depends on US parameters, with a linear dependency on US frequency between 0.5 and 2MHz and an inverse square root dependency to the number of oscillation cycles. Furthermore, single sonoporation events have also been shown to generate intercellular gaps between endothelial cells, persisting over longer timescales than membrane pores. [37], [38] Interestingly, damage-free resealing of cell membrane pores has been shown to depend not only on pore diameter but also on extracellular Ca2+ levels. [37]

Provascular effects of combined use of US and MBs have also been demonstrated. Indeed, convective shear caused by therapeutic results in increased tissue blood flow US, an effect amplified by the presence of cavitating MBs and depending on ATP and purinergic signaling. [33], [39]

Interestingly, while studying the sonoreperfusion effect of US-mediated MB cavitation, which is to say the relief of microvascular obstruction and the restoration of perfusion, Yu et al. showed that oscillating MBs are able to achieve activation of the eNOS pathway, which leads to increased blood perfusion and higher success of sonoreperfusion. [40]

Thus, the goal of this study is to understand how US parameters and MB density influence NO production in stromal and tumor cells, as a way to identify which experimental setup allows the production of an optimal amount of intracellular nitric oxide.

While most studies choose to evaluate NO roduction through indirect measures such as nitrate quantitation, NOS immunoblotting, or NO sensitive electrode, we propose a method using fluorophores, allowing real-time imaging of NO in live cells and spatial quantitation [41], [42]. DAF-FM diacetate, a fluoresceinbased green fluorescent intracellular NO probe, was selected for the higher cell retainability, lower photobleaching, pH-stability, higher specificity and lower detection level conferred by its reaction mechanism (Figure 2). [43]-[45] DAF-FM Da would first be used to image LPSinduced/bradykinin-induced NO release in 4T1 murine mammary tumor cells and in HUVECs as a positive control.

Upon success of this positive control, we would image shear-stress induced NO release triggered by US mediated cavitation of perfluoropropane MBs and study the contribution of US parameters and MB density on intracellular NO levels.

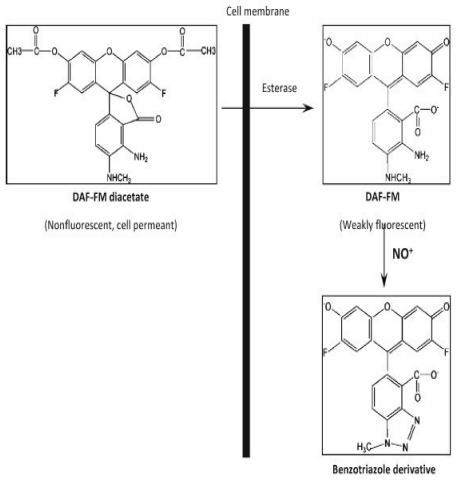

Figure 2: Reaction mechanism of DAF-FM Diacetate intracellular NO probe. Upon entering the cell, DAF-FM Da is converted into DAF-FM by intracellular esterase and is then able to react with NO to form a fluorescent benzotriazole derivative.

Materials and methods

Tumor Cell Culture

4T1 mammary carcinoma cell line was cultured in RPMI + 10% Fetal Bovine Serum + 1% Penicillin/ Streptomycin. The cell culture was maintained in logarithmic growth in T-25 flasks (BioLite 25cm² vented flask, ThermoFisher) by subculturing the flasks at subconfluency. Briefly, media was aspirated, and cells are washed twice with 2 mL of PBS. Cells are then trypsinized with 1.5 mL of 0.25% trypsin for 3-5 minutes at 37°C. Once cells are detached, the enzymatic reaction was blocked with 1.5 mL of culture media, and the cell suspension is then passaged 1:8 or 1:12 in a new 25cm² flask. Media is then changed every 2 to 3 days. For experiments, 4T1 cells were harvested, counted with trypan on a BioRad TC-20 Cell-Counter, and seeded into a 96-well plate (Costar TC-treated 96 wells microplate, Corning Incorporated) at 8000 cells per well into 200 µL of culture media before being grown for 24h at 37°C.

Endothelial Cell Culture

HUVECs endothelial cell line was cultured in EBM-2 (EBMTM-2 Endothelial Cell Growth Basal Medium-2, Lonza Bioscience) supplemented as follows : in 500mL of EBM-2 were added 10mL of Fetal Bovine Serum, 2mL of hFGF, 0.5mL of hydrocortison, 0.5mL of VEGF, 0.5mL of R3-IGF, 0.5mL of ascorbic acid, 0.5mL of hEGF, 0.5mL of GA-1000 and 0.5mL of heparin. The cell culture was maintained in logarithmic growth in T-25 flasks (BioLite 25cm² vented flask, ThermoFisher) by subculturing the flasks at subconfluency. Briefly, media was aspirated and cells are washed twice with 2 mL of D-PBS. Cells are then trypsinized with 1.5 mL of 0.25% trypsin for 3-5 minutes at 37°C. Once cells are detached, the enzymatic reaction was blocked with 1.5 mL of culture media, and the cell suspension is centrifuged at room temperature for 6 min at 300 rpm. The cell pellet is then resuspended in 1 mL of media and passaged 1:8 or 1:12 in a new 25cm² flask. Media is then changed every 2 to 3 days. For experiments, HUVECs were harvested and seeded into a 96-well plate (Costar TC-treated 96 wells microplate, Corning Incorporated) at 16000 cells per well into 200 µL of culture media before being grown for 24h at 37°C. All experiments were conducted between passages 3 and 6.

Fluorescent imaging of NO

DAF-FM Da was selected as our intracellular fluorescent nitric oxide probe. Upon reception, DAF-FM Da (DAF-FM Da solution,5 mM in DMSO, ≥97% (HPLC), Sigma-Aldrich) 5mM stock solution was divided into aliquots, in turn wrapped in aluminum foil and stored at -20°C in the dark. Before use, stock solution was thawed at room temperature and diluted to 50 µM into corresponding culture media. Adequate volumes of the 50µM working solution were added onto cells grown into a 96-well plate along with to 200µL of culture media, in order to reach the desired final concentration ranging between 10µM and 100nM. Cells were then left to incubate for 45 minutes at room temperature, in complete darkness under the laminar hood. After incubation, the DAF-FM Da solution is sucked out and 200µL of fresh media are added into the wells. All working solutions of DAF-FM Da were discarded, as they should not be reused. Green fluorescence and brightfield images were obtained on EVOS FL Cell Imaging System (Life Technologies) at first for 4T1 cells, and on Widefield Olympus IX71 microscope with Evolution VF Cooled Monochrome

(Media Cybernetics) camera for all of the following experiments. Fluorescence signal quantitation was done on ImageJ using a custom macro function. All images were taken under the same imaging conditions. Mean intracellular pixel value is extracted for each image, and DAF-FM intensity is calculated as the mean of these values across all images taken for said well. All statistical analysis was performed using the two-way ANOVA option of the Excel Data Analysis Toolkit.

Chemical trigger of NO synthesis

Chemically-induced NO synthesis was achieved in cells either via exposition to lipopolysaccharides (Lipopolysaccharides from Escherichia coli O55:B5, purified by phenol extraction, Sigma-Aldrich) or bradykinin (Bradykinin acetate salt, powder, ≥98% (HPLC), Sigma-Aldrich). Upon reception, LPS powder was dissolved in PBS to a stock concentration of 1mg/mL and bradykinin powder was dissolved into distilled water to a stock concentration of 1mg/mL. Before use, LPS and bradykinin solutions were thawed on ice and diluted into 200µL of fresh corresponding culture media to their working concentration. Cells were incubated with LPS solutions at final concentrations of 1; 3,3; 10; 33 and 100µg/mL between 5 min and 4h before imaging. Cells were incubated with bradykinin solutions at final concentrations of 0.1, 0.33, 1, 3,3 and 10µg/mL for 30min before imaging.

Mechanical trigger of NO synthesis

Mechanically-induced NO synthesis was achieved by increasing local shear stress levels via US-mediated MB cavitation. Encapsulated perfluoropropane MBs (Definity, Perflutren suspension, Lantheus medical imaging) were used for cavitation. Before use, MBs were counted, and the suspension was diluted into corresponding culture media to a working concentration of 1.10^6 MB/mL. Working solution was then further diluted to final concentrations of 5 to 25 MB/cell into the wells of a 96-well plate. Upon experimentation, cellcontaining wells were emptied and filled with 400µL of culture media containing the appropriate number of MBs. After sealing the lid with tape, the plate was flipped and left upside down for 5min to allow MBs to be in contact with the

cells (Supp. Figure 1) A 1MHz transducer coupled with a Keysight 33500B Trueform waveform generator was used to generate the US pulses. Peak pressure values and number of cycles were respectively 150 kPa, 500kPa or 1500kPa and 10, 100 or 1000 cycles during experiments. A plastic stand was coated with EcoGel 200 (EcoGel 200, Eco-Med Pharmaceutical), a MicroAmp adhesive film (MicroAmp Optical Adhesive Film, ThermoFisher) was then placed upon the gel and coated with a fine layer of distilled water, before the upside-down 96-well plate is laid upon it. The plate itself is then coated with a fine layer of distilled water, and the transducer is finally held above a custom 3% porcine gelatin (G2500, SigmaAldrich) gel phantom also filled with distilled water, calibrated and placed so that the beam is focused on one well. The experimental ultrasound setup is represented in Supp. Figure 1.

Results

Imaging of LPS-induced/bradykinin-induced NO release in tumor cells

4T1 murine mammary cancer cell line was selected to construct our in vitro tumor model, principally for its fast growth rate, and incubated with DAF-FM Da solution followed by either LPS or bradykinin incubation, as described previously.

In LPS-incubated 4T1 cells, a faint green fluorescent signal was observed after 5 minutes but was not correlated to LPS concentration (p= 0,76035787). Instead, data analysis showed that DAF-FM fluorescent signal was almost indistinguishable from background signal, and that signal variation could only be attributed to variations of initial concentration of DAF-FM Da (p= 5,2377691464579E-21). Similarly, data analysis showed that time of exposure to LPS did not contribute to signal variation (p=0,179243476994709). Together, these results suggested lack of LPS-induced NO release in 4T1 cells. Similar observations were made in bradykinin-incubated 4T1 cells (results not showed), suggesting lack of bradykinin-induced response as well in 4T1 cells.

Imaging of LPS-induced/bradykinin-induced NO release in endothelial cells

Human umbilical vein endothelial cells (HUVECs), a cell type widely used to study angiogenesis and endothelial responses, was selected and used as our in vitro endothelial cell model. HUVECs

were incubated with DAF-FM Da solution followed by either LPS or bradykinin incubation, as described previously. After 2h of LPS-incubation, fluorescent signal observed in HUVECs was significantly higher than values obtained in 4T1 for the same imaging parameters. Furthermore, the signal was clearly intracellular, which confirmed proper functioning of the DAF-FM Da dye and thus proper functioning of the NO-release pathway in HUVECs in response to LPS (Figure 3C).

Data analysis showed that in the absence of LPS, low signal intensity varied with DAF-FM concentration, an observation already proposed in 4T1 (Figure 3B). Results also show that intensity increases with LPS concentration (p= 0,00597627888358408), although a clear visual dependency of DAF-FM signal on LPS could only be observed for high enough DAF-FM Da concentration, namely for 3.3 and 10 µM (Figure 3A, 3C). For a concentration of 3.3 µM, signal peaks for 1µg/mL of LPS before decreasing and stagnating for higher agonist concentrations. Given the standard deviation values, and the fact that 3.3 µM is slightly under the lowest DAF-FM Da concentration documented of 5 µM, these discrepancies were attributed to noise. For a concentration of 10 µM, widely used in the literature, the signal increases with LPS concentration in a non-linear manner and reaches its highest observed value, thereby confirming LPS-dependent production of NO in HUVECs.

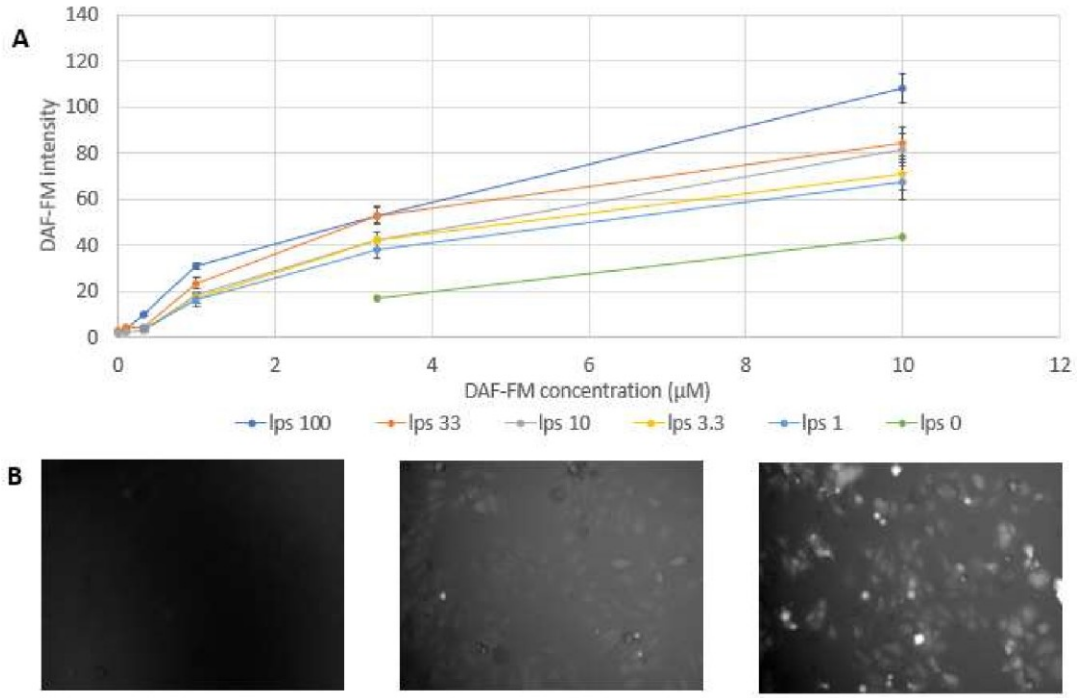

Figure 3: DAF-FM signal intensity in LPS-incubated HUVECs. **A.** DAF-FM intensity as a function of DAF-FM concentration (µM) and LPS concentration (µg/mL). Results indicate that DAF-FM signal increases in the presence of bradykinin in a dose-dependent manner and increases with DAF-FM concentration. **B.** Fluorescence images of LPS-induced NO release in LPS-incubated HUVECS, DAF-FM Da 10µM. Left: 1µg/mL. Center: 10µg/mL. Right: 100µg/mL.

Despite confirming the success of our positive control experiment, increased cell roundedness and detachment also indicated high cell apoptosis after 2h of exposition to LPS, especially at high concentrations, LPS-induced apoptosis being a known phenomenon in HUVECs. [46] DAF-FM signal is highly specific to NO but has also been shown to react with other ROS and RNS, which prompted us to repeat the experiment with bradykinin. Bradykinin is indeed reported to require a shorter exposure time to take effect, and does not trigger any apoptosis pathway in HUVECs. [19], [43] Only DAF-FM Da concentrations of 3.3 and 10 µM were kept to test bradykinin-induced NO release, as they previously showed the best results and are in the range described by the literature. Visually, images obtained after 30 minutes of exposure showed lower cell roundedness and detachment, indicating overall lower cell apoptosis. Data analysis showed that DAF-FM intensity depends on bradykinin concentration (p= 0,0363584122180844), as the signal is multiplied tenfold between the negative control and the lowest bradykinin concentration of 0.1 µM (Figure 4A).

DAF-FM measured intensity also appeared to be strongly dependent on DAF-FM Da concentration (p= 0,00539160021578912), leading us to hypothesize that the relatively low values observed at DAF-FM 3.3 µM might be caused by lack of available DAF-FM for NO molecules to react with. These results confirm proper functioning of bradykinin-induced NO release in HUVECs and led us to select a DAF-FM Da concentration of 10 µM for following experiments.

Altogether, these results confirmed success of chemically-induced NO release positive control experiment and success of fluorescent imaging of intracellular NO in HUVECS; and suggested the use of high DAF-FM Da concentration in following experiments.

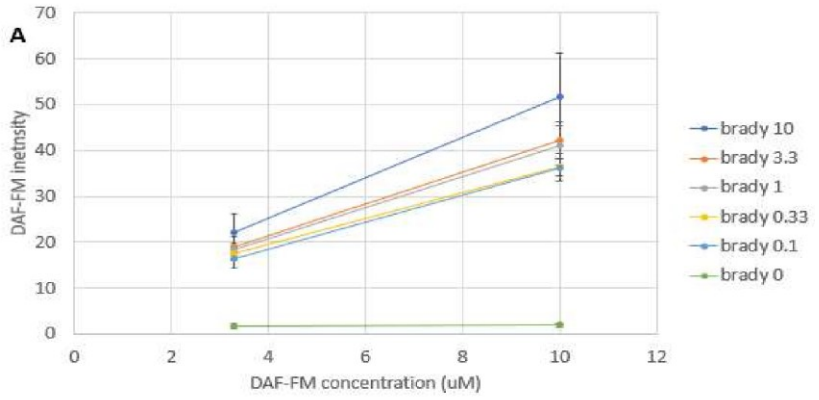

Figure 4: DAF-FM signal intensity in bradykinin-incubated HUVECs. A. DAF-FM signal intensity as a function of DAF-FM concentration (µM) and bradykinin concentration (µM). Results indicate that DAF-FM signal increases with DAF-FM concentration in the presence of bradykinin in a dose-dependent manner. **B.** Fluorescence images of intracellular NO in HUVECs after 30 minutes of 10µg/mL bradykinin incubation. Top: DAF-FM Da 10µM. Bottom: DAF-FM Da 3.3µM. Olympus IX71, 20X

Mechanical trigger of NO synthesis

Mechanical trigger of NO synthesis was only tested in HUVECs, due to previous failure to confirm proper functioning of NO synthesis in 4T1 and to the low probability of significant eNOS expression in 4T1. A combination of suspended perfluoropropane MBs (MB) and US treatment (US) was used to generate localized increases in shear stress, as previously described.

Generally, intensity values obtained through mechanical trigger of NO synthesis were lower than values measured for chemically-induced NO release, which is coherent with the respective mechanistic behaviors and activity of both eNOS and iNOS. [7]

Effects of MB density were compared for three different US conditions: 150kPa/10cycles (“low”), 500kPa/100cycles (“medium”) and 1500kPa/1000cycles (“high”). Data analysis showed that both US conditions (p= 0,000002711806317637) and MB density (p= 0,0000191686609197024) significatively influence DAF-FM signal.

In order to study the contribution of each individual US parameter to the increase in DAF-FM signal, we compared the effects of pressure and number of cycles on DAF-FM signal in HUVECs under two MB density conditions, namely 5 MB/cell and 15 MB/cell. Intensity values measured during these experiments were coherent with the ones previously obtained. Generally, DAF-FM signal appeared to increase with pressure (p= 0,00113295466938398, p= 0,00102719811234963) and number of cycles (p= 0,00893000415969417, p= 0,0108125346316494), as expected. For a density of 5MB/cell, results indicate that a high number of cycles is required to observe significant increase in NO-production, except at high pressure (Figure 6A). Indeed, for a peak pressure of 1500kPa, the relative difference between DAF-FM signals measure for 10 and 100 cycles is maximal. This observation is further corroborated by analyzing the contribution of pressure, data showing that as pressure increases a lower number of cycles is required to obtain a significant effect (Figure 6B) due to the “radiation force” phenomenon.

Similar observations can be made with a density of 15 MB/cell. Once again, highest relative difference between cycle conditions 10 and 100 is observed for a pressure of 1500kPa, indicating that fewer cycles are required to obtain a significant response at high pressure (Figure 7A, 7B). Finally, the influence of MB density itself is coherent with previous observation. Three-fold increase in MB density increases mean DAF-FM intensity for all duty cycle/pressure conditions but does not affect overall profile of response to US parameters. Altogether, these results suggest that US parameters are the main drivers of NO-production by having a direct effect on single-cell response, while MB density likely increases mean DAF-FM intensity by increasing the total number of cells contributing to NO-production.

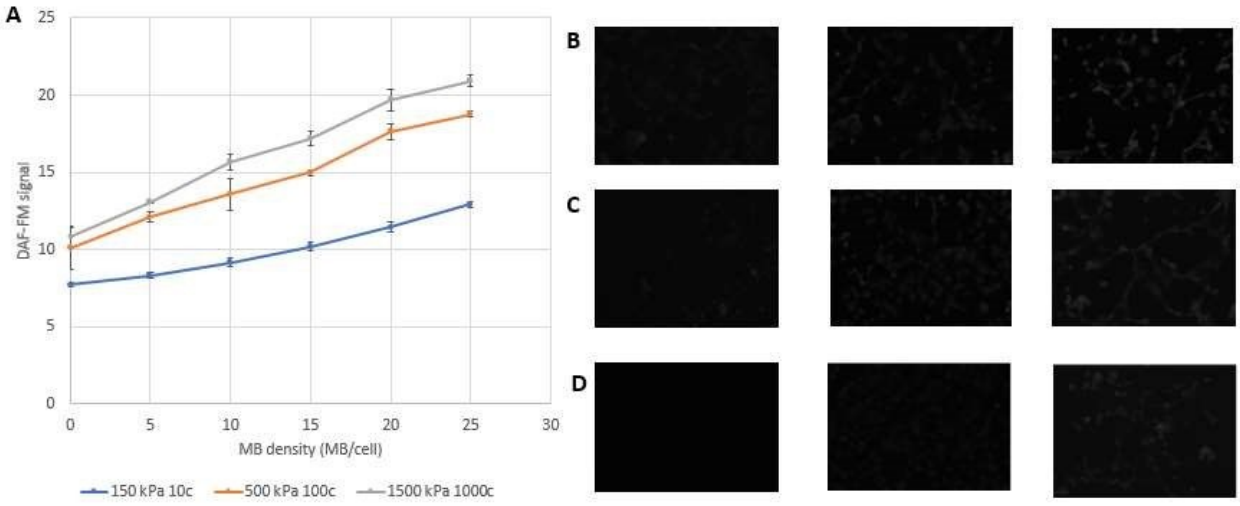

Figure 5: DAF-FM signal intensity in MB/US treated HUVECs. A. DAF-FM signal intensity as a function of MB density under three US conditions. Results indicate that DAF-FM signal increases with US parameters and MB density. **B.** Effect of MB density under "high" ultrasound conditions. Left: 0 MB/cell. Center: 5 MB/cell. Right: 25 MB/cell. Olympus IX71, 20X **C.** Effect of MB density under "medium" ultrasound conditions. Left: 0 MB/cell. Center: 5 MB/cell. Right: 25 MB/cell. Olympus IX71, 20X **D.** Effect of MB density under "low" ultrasound conditions. Left: 0 MB/cell. Center: 5 MB/cell. Right: 25 MB/cell. Olympus IX71, 20X.

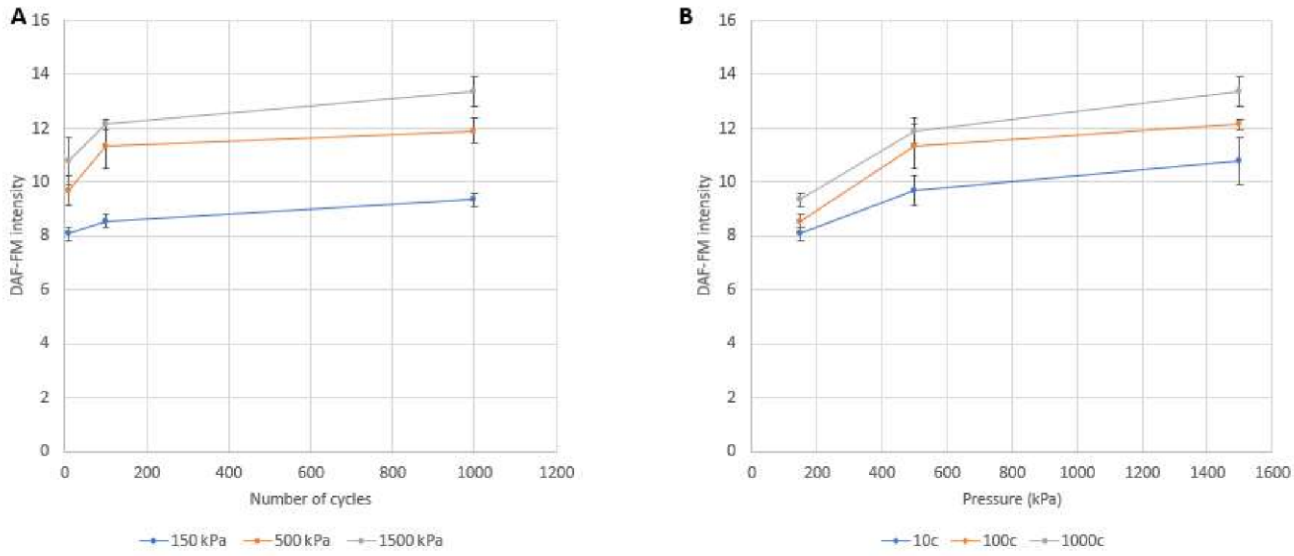

Figure 6: DAF-FM signal intensity in MB/US treated HUVECs, 5 MB/cell density. A. DAF-FM intensity as a function of number of cycles. **B.** DAF-FM intensity as a function of peak pressure (kPa). Results show that signal increases with number of cycles and parameters and indicate that fewer cycles are required to obtain a significant response at high pressure.

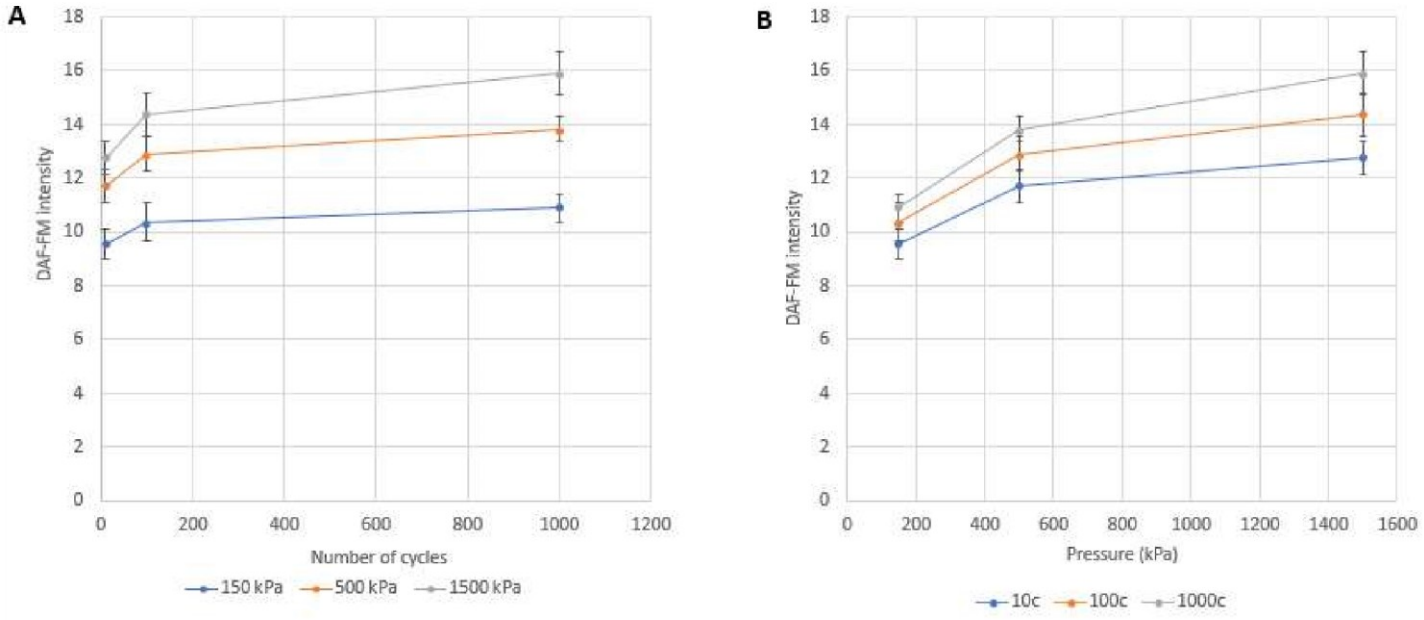

Figure 7: DAF-FM signal intensity in MB/US treated HUVECs, 15 MB/cell density. **A.** DAF-FM intensity as a function of number of cycles. **B.** DAF-FM intensity as a function of peak pressure (kPa). Results show that signal increases with number of cycles and parameters and indicate that fewer cycles are required to obtain a significant response at high pressure.

Discussion

In this study, we investigated live fluorescence imaging of shear stress-induced nitric oxide release in 4T1 murine tumor cells and in human umbilical vein endothelial cells (HUVECs).

After confirming the proper functioning of the L-arginine pathway and thus of NO production in 4T1 cells by exposing them to two known agonists, namely lipopolysaccharides (LPS) and bradykinin, 4T1 response to ultrasound-triggered microbubble (MB) cavitation would have been investigated in order to determine under which ultrasound (US) conditions can we optimize NO production and how intracellular NO concentrations are affecting tumor cell metabolism, either positively or negatively. In a similar way, HUVECs were subjected to LPS and/or bradykinin to visually assess correct functioning of NO-release pathway through fluorescent signal, before shear-stress induced nitric oxide production triggered by MBs and US was studied. Once again, this would help us understand the mechanisms and effects of shear-stress induced NO release on endothelial cells, and the influence of US parameters on levels of intracellular nitric oxide. DAFFM

Da was selected as our nitric oxide probe given its high cell retainability, independency to pH if above 5.5, low photobleaching, higher sensitivity and overall higher NO specificity. [44]

Unfortunately, using DAF-FM Da fluorescent intracellular probe as our only indicator of production of nitric oxide in live cells, we could not confirm proper functioning of the L-arginine pathway in 4T1 murine tumor cells in response to either LPS or bradykinin. Indeed, variations in DAF-FM fluorescent signal can be attributed to variations in initial DAF-FM Da concentration at the time of incubation, since DAF-FM is known to exhibit a low fluorescence upon entering the cell (due to reaction with basal nitric oxide or analogs such as ROS or RNS). [43] Neither LPS nor bradykinin, two known agonists supposed to respectively trigger iNOS and eNOS activity and thus result in increased levels of nitric oxide, seemed to have any effect on DAF-FM signal even after long periods of incubation. Generally speaking, to eliminate the possibility that the cause of the absence of signal is simply due to abnormal reactivity between the dye and nitric oxide, doubling fluorescence intensity measures with either NOS immunoblotting, colorimetric nitrate quantitation or electrochemical NO sensor could be recommended. [47] Loss of function mutation of NOS2 gene and overall variations in iNOS expression or regulation hasn't been documented in 4T1, but iNOS expression and activity varies drastically across tumor types: for example, malignant central nervous system tumors show abnormally high levels of iNOS while extremely low iNOS levels can be observed in various highly metastatic cancer. [7], [48] [49], [50]

Interestingly, 4T1 cells are commonly used as a murine model for triple negative breast cancer (TNBC), the more aggressive type of breast cancer and the most prone to metastasis. [51] Thus, to further investigate the apparent absence of response from 4T1 cells, sequencing of NOS2 gene in our 4T1 cell line to identify possible loss of function polymorphism could be considered, as well as evaluating intracellular iNOS expression levels with Western-Blot.

We successfully imaged intracellular nitric oxide in human umbilical vascular endothelial cells (HUVECs) after exposing them to either LPS or bradykinin for respectively 2h and 30min.

If 2h LPS exposition resulted in an increase in DAF-FM signal and thus in nitric oxide release, drastic variations in cell shape and reduced viability (although not tested) could be observed, which led us to consider the possibility that other molecules released upon apoptosis might

contribute to the observed fluorescence signal. Indeed, it has been shown that DAF-FM, despite having one of the highest specificities to NO, can still react with oxygen-based analogs such as superoxide and hydroxyl radical or with nitrogen-based species such as peroxynitrite. [43] All of those species fall under either the ROS or RNS category and are released upon cell death. Furthermore, previous studies indicated that exposure to LPS triggered apoptosis in HUVECs, by increasing caspase-3 and caspase-1 activities as well as increasing expression of pro-apoptotic protein Bax and tumor suppressor p53. [46]

Bradykinin-triggered NO release was observable after only 30 minutes of incubation, and was not accompanied with high cell roundedness, detachment and/or apparent death. Interestingly, fluorescence signal was lower than for LPS for the same dye concentration and observation parameters. As previously stated, effects of nitric oxide depend on cell type but also on the NOS isoform catalyzing the L-arginine conversion. In addition to promoting apoptosis in HUVECs, LPS triggers iNOS activation which leads to the continuous production of high levels of possibly cytotoxic NO. On the other hand, bradykinin does not activate any apoptosis-related pathway in HUVECs, and triggers eNOS through cytosolic elevation of Ca2+ levels, thus resulting in mostly non-cytotoxic levels of NO. [7] Adding this information to the fact that LPS incubation lasted at least four times longer than bradykinin incubation in our experimental setup, the higher cell viability and overall better quality of the bradykinin-based positive control is evident.

We did not test the effects of the combination of US treatment and MBs on 4T1 cells, mainly because we were unable to obtain the expected results from our intended positive control experiment. As previously stated, tumor behavior regarding variations of nitric oxide levels is complex and hardly predictable and require further exploration. However, since various highly metastatic tumor cells seem to have eliminated iNOS through selective pressure, finding a way to expose these cells to high levels of nitric oxide from exogenous sources such as shear-stress triggered endothelial cells might prove useful in improving current or novel treatment strategies.

Mainly, we managed to image intracellular shear-stress induced NO release in HUVECS after exposing them to US-triggered cavitating perfluoropropane MBs. As expected, DAF-FM fluorescence signal obtained one to five minutes after US treatment was dependent on MBs to

cell ratio, on peak US pressure and on number of cycles per pulse, increasing with these three parameters. These observations confirmed previous findings showing that US-mediated cavitation of MBs generated enough elevation of local shear-stress to trigger activation of eNOS in either animal or human endothelial cells. [24], [40] Although this phenomenon had already been documented, NO production was being quantified globally either with an electrochemical sensor, a colorimetric nitrate assay or immunoblotting hours after the experiment, methods which did not allow real-time imaging and spatial quantitation of NO either in vitro or in vivo. By spatially tracking shearstress induced NO release and being able to study single-cell response, fluorescent indicators offer ways towards a better understanding of MB-cell interactions.

Here, our results show that influence of US parameters (pressure and number of cycles) and MB density can be tracked by DAF-FM fluorescence, thus confirming their role as drivers of NO production in endothelial cells. Our results also clearly indicate the existence of a parameters-dependent threshold for NO production, as the significative difference between cycle conditions diminishes under high pressure, although this observation might be a direct consequence of our reversed experimental setup which allows bubbles to move away from the cells, a phenomenon more prevalent at high pressure and/or high duty cycles. Unfortunately, we were not able to statistically confirm that MB density actually increases mean signal by increasing the total number of triggered cells. Furthermore, overall low DAF-FM intensity values do not allow us to come to a definitive conclusion, as imaging parameters still need to be optimized. It also has to be noted that images often showed high cell roundedness and detachment for high pressure and/or high number of cycles, indication of possible apoptosis, making it difficult to have a definitive explanation of the mechanisms behind MB/US and endothelial cell interaction. For this reason, a propidium iodine (PI) counterstaining could prove useful in following experiments. Furthermore, extracting actual intracellular NO concentrations, either directly from DAF-FM signal intensity using a calibration curve or through a colorimetric nitrate quantitation, would also provide useful information on the cellular effects of UStriggered MB-mediated shear stress-induced NO release.

Recent studies showed that shear stress-induced NO production depends on ATP autocrine signaling as well as calcium ions, ATP being required to induce eNOS phosphorylation. [33] Previous research from our lab showed that combination of US treatment and MBs was able to

increase local extracellular ATP levels, a phenomenon achieved through sonoporation but also through promotion of pannexin 1 channel activity. Just like nitric oxide, tumor behavior regarding ATP levels is rather ubiquitous, some tumor lines showing increased proliferation under high-ATP conditions while others experience cytotoxic effects under such high concentrations of ATP. [52], [53] Thus, being able to combine imaging of NO and ATP-release with fluorescent indicators would help shed light on the interaction between these two molecules, but also on the spatial dynamics of tumor cells response to MB cavitation.

Finally, a microfluidics device for luciferin/luciferase tracking of ATP-release using cancer cells, MBs and US pulses is being developed in our lab and could in time be coupled with fluorescent-based NO imaging. Microfluidic devices are actively being developed in order to provide vascular models for the study of angiogenesis, endothelial behavior and tumor behavior, and would offer the possibility of novel co-culture setups closer to in vivo. [54], [55]

References

[1] M. A. Marletta, « Nitric oxide synthase structure and mechanism », J. Biol. Chem., vol. 268, nº 17, p. 12231-12234, juin 1993.

[2] S. S. Gross et M. S. Wolin, « Nitric oxide: pathophysiological mechanisms », Annu. Rev. Physiol., vol. 57, nº 1, p. 737–769, 1995.

[3] O. W. Griffith et D. J. Stuehr, « Nitric oxide synthases: properties and catalytic mechanism », Annu. Rev. Physiol., vol. 57, nº 1, p. 707–734, 1995.

[4] R. Govers et T. J. Rabelink, « Cellular regulation of endothelial nitric oxide synthase », Am. J. Physiol.-Ren. Physiol., vol. 280, nº 2, p. F193–F206, 2001.

[5] C. Nathan, « Nitric oxide as a secretory product of mammalian cells », FASEB J. Off. Publ. Fed. Am. Soc. Exp. Biol., vol. 6, nº 12, p. 3051-3064, sept. 1992.

[6] S. Moncada et A. Higgs, « The L-arginine-nitric oxide pathway », N. Engl. J. Med., vol. 329, nº 27, p. 2002-2012, déc. 1993.

[7] D. Fukumura, S. Kashiwagi, et R. K. Jain, « The role of nitric oxide in tumour progression », Nat. Rev. Cancer, vol. 6, nº 7, p. 521-534, juill. 2006.

[8] K. MacNaul et N. Hutchinson, « Differential expression of iNOS and cNOS mRNA in human vascular smooth muscle cells and endothelial cells under normal and inflammatory conditions », Biochemical and Biophysical Research Communications, p. 1330-1334, 1993.

[9] S. J. Ajizian, B. K. English, et E. A. Meals, « Specific inhibitors of p38 and extracellular signal-regulated kinase mitogen-activated protein kinase pathways block inducible nitric oxide synthase and tumor necrosis factor accumulation in murine macrophages stimulated with lipopolysaccharide and interferon-gamma », J. Infect. Dis., vol. 179, nº 4, p. 939-944, avr. 1999.

[10] C. Bernardini, F. Greco, A. Zannoni, M. L. Bacci, E. Seren, et M. Forni, « Differential expression of nitric oxide synthases in porcine aortic endothelial cells during LPS-induced apoptosis », J. Inflamm., vol. 9, n° 1, p. 47, 2012.
[11] J. Gao et al., « Protective effects of propofol on lipopolysaccharide-activated endothelial cell barrier dysfunction », Inflamm. Res., vol. 55, n° 9, p. 385-392, sept. 2006.
[12] N. Koide et al., « Lipopolysaccharide enhances interferon-γ-induced nitric oxide (NO) production in murine vascular endothelial cells via augmentation of interferon regulatory factor-1 activation », J. Endotoxin Res., vol. 13, n° 3, p. 167-175, juin 2007.
[13] D. Salvemini, R. Korbut, E. Anggård, et J. Vane, « Immediate release of a nitric oxide-like factor from bovine aortic endothelial cells by Escherichia coli lipopolysaccharide », Proc. Natl. Acad. Sci. U. S. A., vol. 87, n° 7, p. 2593-2597, avr. 1990.
[14] D. Schwartz et al., « Inhibition of constitutive nitric oxide synthase (NOS) by nitric oxide generated by inducible NOS after lipopolysaccharide administration provokes renal dysfunction in rats. », J. Clin. Invest., vol. 100, n° 2, p. 439-448, juill. 1997.
[15] Z. Spolarics, J. J. Spitzer, J. F. Wang, J. Xie, J. Kolls, et S. Greenberg, « Alcohol administration attenuates LPSinduced expression of inducible nitric oxide synthase in Kupffer and hepatic endothelial cells », Biochem. Biophys. Res. Commun., vol. 197, n° 2, p. 606-611, déc. 1993.
[16] E. K. Tamura, E. Cecon, A. W. A. Monteiro, C. L. M. Silva, et R. P. Markus, « Melatonin inhibits LPS-induced NO production in rat endothelial cells », J. Pineal Res., vol. 46, n° 3, p. 268-274, avr. 2009.
[17] P. A. Vo, B. Lad, J. A. P. Tomlinson, S. Francis, et A. Ahluwalia, « Autoregulatory Role of Endothelium-derived Nitric Oxide (NO) on Lipopolysaccharide-induced Vascular Inducible NO Synthase Expression and Function », J. Biol. Chem., vol. 280, n° 8, p. 7236-7243, févr. 2005.
[18] T. Hayashi, E. Abe, T. Yamate, Y. Taguchi, et H. E. Jasin, « Nitric oxide production by superficial and deep articular chondrocytes », Arthritis Rheum. Off. J. Am. Coll. Rheumatol., vol. 40, n° 2, p. 261–269, 1997.
[19] Y. Kono et al., « Bradykinin inhibits serum-depletion-induced apoptosis of human vascular endothelial cells by inducing nitric oxide via calcium ion kinetics », J. Cardiovasc. Pharmacol., vol. 39, n° 2, p. 251-261, févr. 2002.
[20] C. L. M. Silva et al., « Melatonin inhibits nitric oxide production by microvascular endothelial cells in vivo and in vitro », Br. J. Pharmacol., vol. 151, n° 2, p. 195-205, mai 2007.
[21] E. K. Tamura, C. L. M. Silva, et R. P. Markus, « Melatonin inhibits endothelial nitric oxide production in vitro », J. Pineal Res., vol. 41, n° 3, p. 267-274, oct. 2006.
[22] A. M. Andrews, D. Jaron, D. G. Buerk, et K. A. Barbee, « Shear Stress-Induced NO Production is Dependent on ATP Autocrine Signaling and Capacitative Calcium Entry », Cell. Mol. Bioeng., vol. 7, n° 4, p. 510-520, déc. 2014.
[23] A. M. Andrews, D. Jaron, D. G. Buerk, P. L. Kirby, et K. A. Barbee, « Direct, real-time measurement of shear stressinduced nitric oxide produced from endothelial cells in vitro », Nitric Oxide, vol. 23, n° 4, p. 335-342, déc. 2010.
[24] P. Ulker, G. Filiz, M. H. J, et B. O. K, « Nitric oxide generated by red blood cells following exposure to shear stress dilates isolated small mesenteric arteries under hypoxic conditions », Clin. Hemorheol. Microcirc., n° 4, p. 357– 369, 2013.
[25] H. Wessells et al., « Fluid shear stress-induced nitric oxide production in human cavernosal endothelial cells: inhibition by hyperglycaemia », BJU Int., vol. 97, n° 5, p. 1047-1052, mai 2006.
[26] M. Noris et al., « Nitric oxide synthesis by cultured endothelial cells is modulated by flow conditions », Circ. Res., vol. 76, n° 4, p. 536-543, avr. 1995.

[27] D. A. Wink et J. B. Mitchell, « Chemical biology of nitric oxide: Insights into regulatory, cytotoxic, and cytoprotective mechanisms of nitric oxide », Free Radic. Biol. Med., vol. 25, nº 4-5, p. 434-456, sept. 1998.
[28] M. M. Cortese-Krott et M. Kelm, « Endothelial nitric oxide synthase in red blood cells: Key to a new erythrocrine function? », Redox Biol., vol. 2, p. 251-258, 2014.
[29] D. Fukumura, F. Yuan, M. Endo, et R. K. Jain, « Role of nitric oxide in tumor microcirculation. Blood flow, vascular permeability, and leukocyte-endothelial interactions. », Am. J. Pathol., vol. 150, nº 2, p. 713, 1997.
[30] B. F. Jordan et al., « Nitric oxide as a radiosensitizer: Evidence for an intrinsic role in addition to its effect on oxygen delivery and consumption: Nitric Oxide as a Radiosensitizer », Int. J. Cancer, vol. 109, nº 5, p. 768-773, mai 2004.
[31] J.-M. Escoffre et A. Bouakaz, Éd., Therapeutic Ultrasound, vol. 880. Cham: Springer International Publishing, 2016.
[32] K. Kooiman, H. J. Vos, M. Versluis, et N. de Jong, « Acoustic behavior of microbubbles and implications for drug delivery », Adv. Drug Deliv. Rev., vol. 72, p. 28-48, juin 2014.
[33] J. T. Belcik et al., « Augmentation of Muscle Blood Flow by Ultrasound Cavitation Is Mediated by ATP and Purinergic Signaling », Circulation, vol. 135, nº 13, p. 1240-1252, mars 2017.
[34] G. Shapiro et al., « Multiparameter evaluation of in vivo gene delivery using ultrasound-guided, microbubbleenhanced sonoporation », J. Controlled Release, vol. 223, p. 157-164, févr. 2016.
[35] A. Jain, A. Tiwari, A. Verma, et S. K. Jain, « Ultrasound-based triggered drug delivery to tumors », Drug Deliv. Transl. Res., vol. 8, nº 1, p. 150-164, févr. 2018.
[36] S. Keller, M. Bruce, et M. A. Averkiou, « Ultrasound Imaging of Microbubble Activity during Sonoporation Pulse Sequences », Ultrasound Med. Biol., vol. 45, nº 3, p. 833-845, mars 2019.
[37] Y. Hu, J. M. F. Wan, et A. C. H. Yu, « Membrane Perforation and Recovery Dynamics in Microbubble-Mediated Sonoporation », Ultrasound Med. Biol., vol. 39, nº 12, p. 2393-2405, déc. 2013.
[38] B. Helfield, X. Chen, S. C. Watkins, et F. S. Villanueva, « Biophysical insight into mechanisms of sonoporation », Proc. Natl. Acad. Sci. U. S. A., vol. 113, nº 36, p. 9983-9988, 06 2016.
[39] J. T. Belcik et al., « Augmentation of limb perfusion and reversal of tissue ischemia produced by ultrasoundmediated microbubble cavitation », Circ. Cardiovasc. Imaging, vol. 8, nº 4, avr. 2015.
[40] F. T. H. Yu, X. Chen, A. C. Straub, et J. J. Pacella, « The Role of Nitric Oxide during Sonoreperfusion of Microvascular Obstruction », Theranostics, vol. 7, nº 14, p. 3527-3538, 2017.
[41] Y. C. Boo, S. L. Tressel, et H. Jo, « An improved method to measure nitrate/nitrite with an NO-selective electrochemical sensor », Nitric Oxide Biol. Chem., vol. 16, nº 2, p. 306-312, mars 2007.
[42] H. Tsukahara, D. V. Gordienko, et M. S. Goligorsky, « Continuous monitoring of nitric oxide release from human umbilical vein endothelial cells », Biochem. Biophys. Res. Commun., vol. 193, nº 2, p. 722-729, juin 1993.
[43] Y.-J. Xie et W.-B. Shen, « In vivo Imaging of Nitric Oxide and Reactive Oxygen Species Using Laser Scanning Confocal Microscopy », in Plant Salt Tolerance, S. Shabala et T. A. Cuin, Éd. Totowa, NJ: Humana Press, 2012, p. 191-200.
[44] H. Li et A. Wan, « Fluorescent probes for real-time measurement of nitric oxide in living cells », The Analyst, vol. 140, nº 21, p. 7129-7141, 2015.
[45] X. Wang, « Nitric oxide signalling in astrocytes », Université de Montréal, 2017.

[46] N. Munshi, A. Z. Fernandis, R. P. Cherla, I.-W. Park, et R. K. Ganju, « Lipopolysaccharide-Induced Apoptosis of Endothelial Cells and Its Inhibition by Vascular Endothelial Growth Factor », J. Immunol., vol. 168, nº 11, p. 5860-5866, juin 2002.
[47] C. W. C. Bi et al., « Fo Shou San, an Ancient Chinese Herbal Decoction, Protects Endothelial Function through Increasing Endothelial Nitric Oxide Synthase Activity », PLoS ONE, vol. 7, nº 12, p. e51670, déc. 2012.
[48] F. Vannini, K. Kashfi, et N. Nath, « The dual role of iNOS in cancer », Redox Biol., vol. 6, p. 334-343, déc. 2015.
[49] S. K. Choudhari, M. Chaudhary, S. Bagde, A. R. Gadbail, et V. Joshi, « Nitric oxide and cancer: a review », World J. Surg. Oncol., vol. 11, nº 1, p. 118, 2013.
[50] H. Cheng, L. Wang, M. Mollica, A. T. Re, S. Wu, et L. Zuo, « Nitric oxide in cancer metastasis », Cancer Lett., vol. 353, nº 1, p. 1-7, oct. 2014.
[51] S. Badve et al., « Basal-like and triple-negative breast cancers: a critical review with an emphasis on the implications for pathologists and oncologists », Mod. Pathol., vol. 24, nº 2, p. 157-167, févr. 2011.
[52] Y. Qian, X. Wang, Y. Li, Y. Cao, et X. Chen, « Extracellular ATP a New Player in Cancer Metabolism: NSCLC Cells Internalize ATP In Vitro and In Vivo Using Multiple Endocytic Mechanisms », Mol. Cancer Res., vol. 14, nº 11, p. 1087-1096, nov. 2016.
[53] J. X. Jiang, M. A. Riquelme, et J. Z. Zhou, « ATP, a double-edged sword in cancer », Oncoscience, vol. 2, nº 8, p. 673, 2015.
[54] C. Franco et H. Gerhardt, « Blood vessels on a chip », Nature, vol. 488, nº 7412, p. 465-466, août 2012.
[55] R. G. Li, « Engineering a vascular model based on microfluidics for studying microbubbles in an acoustic field », NTNU, 2018.

A

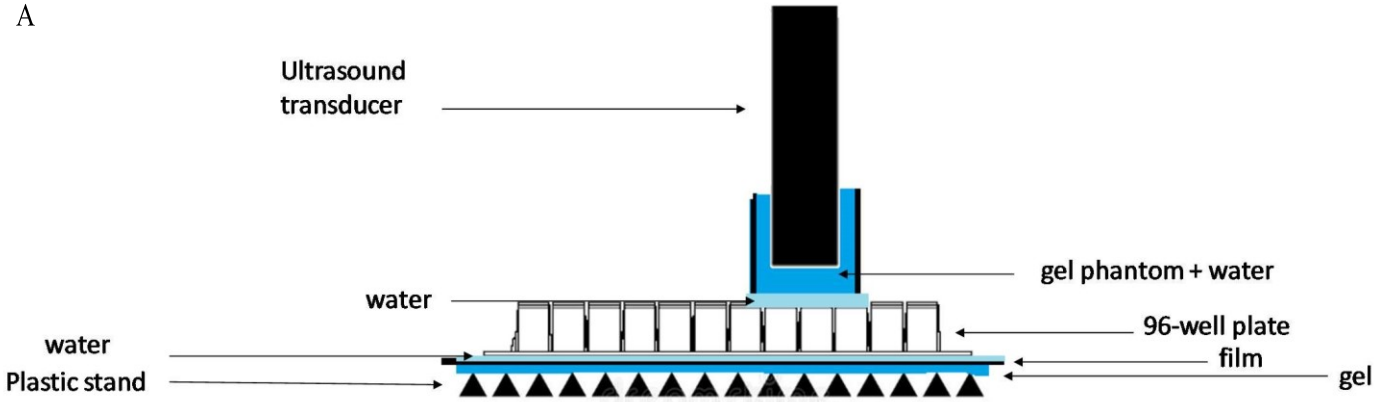

B

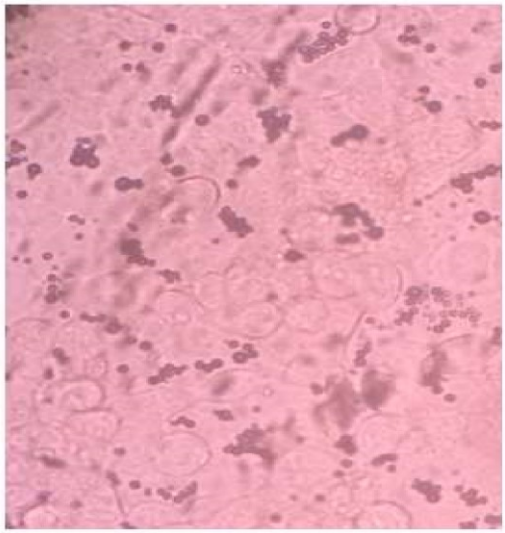

Supplementary Figure 1: A. Custom ultrasound apparatus for US-triggered MB-mediated NO release in live cells. A plastic stand was coated with EcoGel 200 (EcoGel 200, Eco-Med Pharmaceutical), a MicroAmp adhesive film (MicroAmp Optical Adhesive Film, ThermoFisher) was then placed upon the gel and coated with a fine layer of distilled water, before the upside-down 96-well plate is laid upon it. The plate itself is then coated with a fine layer of distilled water, and the transducer is finally held above a custom 3% porcine gelatin (G2500, Sigma-Aldrich) gel phantom also filled with distilled water, calibrated and placed so that the beam is focused on one well. B. Brightfield image confirmation of contact between perfluoropropane microbubbles and cells in our experimental setup. 20X.